Predictive Forward Dynamic Simulation of Manual Wheelchair Propulsion

by

Colin Brown

A thesis
presented to the University of Waterloo
in fulfillment of the
thesis requirement for the degree of
Master of Applied Science
in
System Design Engineering

Waterloo, Ontario, Canada, 2018

I hereby declare that I am the sole author of this thesis. This is a true copy of the thesis, including any required final revisions, as accepted by my examiners.

I understand that my thesis may be made electronically available to the public.

Abstract

Approximately 200,000 Canadians require the use of a manual wheelchair to complete activities ranging from tasks of daily living to competing on elite sports teams. Research to understand the biomechanics of manual wheelchair propulsion has grown steadily in the last 30 years. Many of these studies have incorporated experimental data and mathematical models to advance this field of research. A range of models have been developed for use in inverse dynamic simulations, yet few have been used in predictive forward dynamic simulations, which have the benefit of requiring little to no experimental data.

The purpose of this project was to test the feasibility of implementing a two-dimensional model to generate forward dynamic fully predictive computer simulations of a wheelchair basketball athlete on a stationary ergometer. The body segment inertial parameters used in the two-dimensional model were obtained from a projection parameter identification method using a validated three-dimensional inverse dynamic model developed by the Canadian Sports Institute Ontario (CSIO). Furthermore, subject-specific torque generator functions were developed through joint torque testing of an elite wheelchair basketball athlete on a Biodex System 4 Pro human dynamometer system. A direct collocation optimization technique using GPOPS-II was utilized to determine input torque functions that minimized the change in torque activations and hand forces to best replicate the human muscle recruitment strategy. Dynamic equations were generated using the multibody software MapleSim, and bounds for states and controls were determined from experimental data.

Forward dynamic simulations were generated with varying initial conditions. Similar profiles and magnitudes of kinematic and kinetic data were observed between fixed final time simulations and CSIO experimental data of a sub-maximal first push. Additional simulations were generated that varied the seat position and used an additional objective function term that minimized push time to simulate a maximal effort from rest. These simulations resulted in push times that compared closely to experiment for the first push. Furthermore, seat heights inferior to the neutral experimental position were found to produce similar joint torque effects to those reported in previous modeling studies. An anterior seat placement to the neutral experimental position produced the quickest push time with the least amount of shoulder torque required. Variations in this model compared to those in literature, as well as the model parameter identification of only one subject, provided limited validation of these seat adjustment findings. However, the work completed in this project demonstrates that fully predictive simulations of wheelchair propulsion can produce realistic results, and shows the potential of varying simulation parameters to make meaningful conclusions. Future work should continue the validation of this method by testing more subjects and increasing the complexity of the model.

iii

Acknowledgements

I would like to express my sincere gratitude to the following people who made this research possible by providing me their invaluable support and wisdom at various steps along the way:

- Dr. John McPhee, my supervisor, who opened my eyes to the world of multibody dynamic modeling and computer simulation, and provided me with countless learning opportunities and words of advice throughout my Masters degree

- Dr. Tom Willett, my TA supervisor, who not only gave me the chance to mentor and teach the next generation of engineers, but provided mentorship in my career and life pursuits

- Fellow members of the Motion Research Group at the University of Waterloo, who offered weekly learning opportunities and research achievements to aspire to, as well as providing me with lifelong friendships

- Lindsay Musalem and Devon Frayne, Canadian Sports Institute Ontario biomechanists, for allowing me the opportunity to contribute to an important and inspiring research field

- And most importantly my wife, Janessa Brown, who has supported me every step of the way in my developing career, and for managing the patience and wisdom to never take me too seriously

Table of Contents

List of Tables

List of Figures

Abbreviations

BSIPs Body Segment Inertial Parameters 27–31, 92

CSIO Canadian Sports Institute Ontario vii, viii, 1, 4, 19, 23–28, 30, 32–35, 60, 68, 76, 78, 79, 92

EMG electromyography 4, 5, 9, 10, 14–16, 18

FEF Fractional Effective Force 6–8, 11, 14, 15, 18, 66

FG Flexion Group 10

iDXA dual-energy-X-ray absorptiometry 22, 23, 27

LGR Legendre-Gauss-Radau 56

MAE Mean Absolute Error 16

MRI Magnetic Resonance Imaging 22

NFG Non Flexion Group 10

NLP Nonlinear Programming Problem 56

ODE Ordinary Differential Equation 56

RF Resultant Force 19

RMSD Root Mean Squared Deviation 60, 62, 63, 66

List of Symbols

F Hand force matrix in the objective function 59

F_R Constant rolling resistance term 53

I_{m_z} Equivalent rotational inertia of the athlete and wheelchair represented at the wheel axle in the body-fixed z direction 54

Φ Kinematic constraints of the system 56

$\tau_{V_c}(t, \omega)$ Velocity scaled concentric torque 20

$\tau_{act}(t)$ Activation torque 35, 36

t_{act} Time constant of activation 20

t_{deact} time constant of deactivation 20

$\tau_A(\theta)$ Torque-angle scaling 35, 36, 50, 63

T_D Aerodynamic drag resistive torque 53

τ_I Inertial resistance torque of the athlete and wheelchair 53

$\boldsymbol{\tau}_i$ Torque input to the model about each joint viii, 26

τ_{mot} Output motor torque for the resistive torque function 53, 54

τ_m Maximum possible applied torque 20, 45, 47

τ_0 Isometric torque 45, 47, 58, 77

$\tau_P(\theta, \omega)$ Passive torque ix, 35, 52

Chapter 1

Introduction

It is common for people with a spinal cord or lower limb injury to require a manually propelled wheelchair to complete activities of daily living. In Canada, a review of the Canadian Survey on Disability (2012) determined that approximately 200,000 Canadians are manual wheelchair users [7]. Research in improving biomechanical models for manual wheelchair propulsion is of great interest to researchers and medical staff in helping paraplegic individuals complete activities of daily living with less risk to injury. Development of this research area is also sought after by coaches and athletes to improve performance and mitigate injury risk in Paralympic sport. Athletes are consistently seeking methods to provide an edge to their game or to improve longevity in their career, which may be achieved by optimal adjustments to their wheelchair equipment.

1.1 Motivation and Goals

The standard method of making a wheelchair setup change is currently a lengthy and expensive process, and is carried out on a trial-and-error basis with an athlete going through several wheelchairs over their career. This typically carries a heavy price tag and financial burden to the program and/or athlete. To address this issue, the CSIO received funding from the Innovations for Gold research grant, which is a subsidy of the Own the Podium national sports research program. The first two phases of the project focused on collecting experimental data to investigate the biomechanical response to altered wheelchair parameters such as seat angle, wheel size, and seat height, which were found to have a quantifiable impact on the performance and propulsion effort. The proposed work for phase three of the

project was to explore the feasibility of using a computer simulation tool to predict biomechanical changes to altered wheelchair settings, as little research in this area of focus has been undertaken previously. Therefore, the goal of this project was to develop a validated, fully predictive computer simulation of wheelchair propulsion, and explore the feasibility of using it to provide individualized recommendations of optimal wheelchair settings. The major benefit of using a computer simulation would be the drastic reduction in the time and effort required to fit an athlete to a new wheelchair. In addition, suggestions could be provided for improving technique.

1.2 Document Structure

This report is organized in the following manner:

- Chapter 1 provides an introduction that communicates the underlying motivation and goals for this work and summarizes the main contributions to this field of research.

- Chapter 2 provides a detailed review of wheelchair propulsion modeling studies to date, and discusses the current state of predictive simulation research in sports applications. In addition, a summary is provided of the methods used by the CSIO in phase one and two, from which data was shared for this study.

- Chapter 3 describes each aspect of the wheelchair propulsion model, including its development and validation.

- Chapter 4 outlines the experimental data collected and methods implemented to generate a predictive version of the model described in Chapter 3. The first section of this chapter highlights the subject-specific torque data that was collected and torque generating functions to which the data was fit. The remaining section outlines the resistive torque function provided to the wheel joint.

- Chapter 5 discusses the optimization method employed to determine inputs for the computer simulation. Furthermore, the key results obtained from four types of simulation experiments conducted in this study are presented and discussed.

- Chapter 6 provides a conclusion to this study by summarizing the work completed. The limitations of the study are discussed and recommendations are made for future work.

1.3   Contributions

- Fully-predictive model incorporating a previously-validated continuous resistive torque function and utilization of an objective function for simulating maximum performance

- Optimal joint torque activations obtained using direct-orthogonal collocation for application in a wheelchair propulsion predictive simulation

- Development and validation of a projected 2D model, incorporating a torso joint, that was representative of a 3D model specific to wheelchair propulsion

- Development of subject-specific torque functions for a wheelchair basketball Paralympic athlete for implementation in a forward dynamic model

- Detailed review of quasi-static, inverse dynamic, and forward dynamic models of wheelchair propulsion to date

Chapter 2

Background and Literature Review

A wide range of research areas have been explored to understand the biomechanics of manual wheelchair propulsion. Many of these studies have focused primarily on the collection of experimental data to make generalized and subject-specific conclusions about the kinematics and kinetics of the human body in wheelchair propulsion [8]. These studies typically collect data with motion capture equipment, electromyography (EMG), and handrim force sensors. Furthermore, researchers typically conduct experimental testing in controlled laboratory conditions rather than field evaluations. This involves the use of a wheelchair ergometer or treadmill, which allows wheelchair propulsion to take place in a static environment at controlled speeds and resistances. This collected data often provides complementary aspects to simulation studies, as this experimental data can be used for the refinement or input of a model. By modeling the athlete and their equipment, computer simulations can be utilized to optimize equipment design and parameter settings to maximize performance and reduce the risk of injury. In addition, recommendations for improving technique can be made. The number of studies has grown to a point where it is now difficult to understand quickly the research developments produced over the last 30 years. Therefore, to aid the pursuits of other researchers in continuing the development of original research, a detailed review (first of its kind) is presented of wheelchair propulsion modeling efforts to date. Furthermore, a summary of relevant forward dynamic studies in sport-specific applications is provided. This chapter concludes by discussing gaps to be addressed in wheelchair propulsion modeling, as well as a brief summary of the work completed to date by the CSIO.

2.1 Wheelchair Propulsion Modeling to Date

To date, much research has been devoted to understanding the role of the athlete; little has been done to further understand the dynamic effects of the wheelchair-user system [9]. Mathematical models have emerged as useful tools to eliminate this gap in knowledge, particularly when combined with a quasi-static, inverse dynamic, or forward dynamic analysis [8].

2.1.1 Quasi-Static and Inverse Dynamic Models

Four-Bar Mechanisms

The first known modeling estimate of the upper extremity joint loading and moments in wheelchair propulsion were reported in a study by Cerquiglini in 1981 [10]. Few details of the model are presented in his study; however all motions and results are reported in the 2D sagittal plane of the wheelchair user. Paraplegic subjects pushed a custom wheelchair ergometer at a steady-state push frequency with a crank handle. Strain-gauge transducers measured radial and tangential force components at the crank, and two stereoscopically coupled cinecameras were used to obtain tridimensional measurements of upper extremity kinematics. Body segment inertial parameters were obtained from [11]. An inverse dynamic analysis of the input kinematic and kinetic data found that the forward flexor moments in the shoulder were primarily involved, with the elbow and wrist moments being 1/3 and 1/5 of the shoulder, respectively. Furthermore, EMG data was collected and combined with the joint load calculations to estimate that half the elbow activity was eccentric rather than concentric. Although this study was limited by the measurement tools of its time and did not use a wheelchair for experimental testing, it set a precedent for the decades of many research studies to follow.

One of the benefits of using a 2D model that was exploited often by researchers was the ability to perform a realistic quasi-static or inverse dynamic analysis with limited experimental data. Richter [2] first demonstrated this by using a four bar mechanism to model the wheelchair-user system, which consisted of the upper arm, forearm-hand combination, and wheel. The model equations and calculations of this study were later corrected by Leary *et al* [3]. In both studies, the shoulder joint and hub of the wheel are fixed in the inertial reference frame, which can be viewed in Figure 2.1.

Segment lengths, position of the shoulder with respect to the wheelhub, and the force applied to the handrim were input to the model. Gravitational and inertial effects were ignored with the analysis treated as quasi-static. Kinematic assumptions were used to define
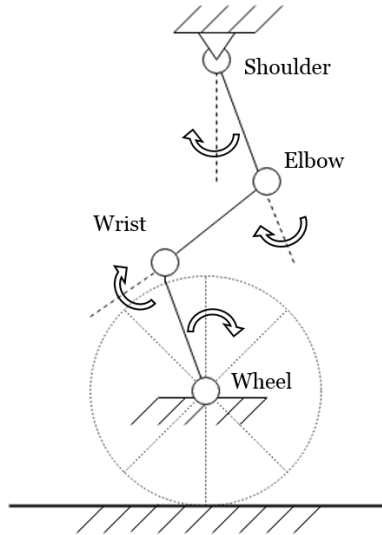
Figure 2.1: Model schematic used by Richter [2] and Leary *et al* [3] re-created by the author

initial and final state conditions, such as the forearm-hand segment being perpendicular to the handrim at initial hand contact, and the elbow being fully extended at hand release. The contact and release angles could then be calculated utilizing trigonometry. A generalized handrim force profile of propulsion was determined from 5 wheelchair users using SMARTWheel (Out-Front, Inc.), and was input to the model over the entire push angle range. A quasi-static analysis could then be performed at each wheel angle to determine both the elbow and shoulder torque necessary to balance the input handrim forces.

A quasi-static analysis using a four-bar mechanism was also conducted by Guo *et al* [12, 13] to investigate the Fractional Effective Force (FEF) in wheelchair propulsion. The FEF is described as the fraction of tangential force to the total force magnitude at the handrim. In this study, an optimization problem was formulated to solve the unknown hand forces by maximizing the moment about the wheel axle, with the lower and upper joint torque constraints determined through isokinetic dynamometer testing. If the handrim force direction were to become more tangential, the shoulder flexor would reach its maximum constraint with a smaller wheel moment. The simulation results found that the optimal handrim force direction was upward in the first half of the push (hand positioned behind Top Dead Center (TDC)), and downward in the second half (hand positioned after TDC). This differed largely from the experimental results collected, as the handrim force direction was always pointed downward; this was one of the first studies to show that an

optimal FEF is not purely tangential. The authors suggested that this was the result of the users resistance to switching from elbow flexor activation to extensor activation. Furthermore, Guo *et al's* simulations predicted that the largest FEF value should occur at the end of the propulsion phase for a maximal wheel moment. This could explain why wheelchair racing athletes rotate their torso to a maximally anterior position. Using this model and similar quasi-static analysis methods, this research group also determined in a separate study that a larger possible FEF could be achieved with an increased handrim diameter, which also increased the ability to generate a large moment about the wheel. The author of this study argued that a 2D model examining wheelchair kinetics and kinematics in the sagittal plane was sufficient, as this is the plane in which the majority of activity occurs [14].

Munaretto *et al* [15] produced one of the more recent studies that utilized a four-bar mechanism in the analysis of wheelchair propulsion, in particular to understand the impact of reaction force direction on mechanical upper extremity demand. Motion capture and handrim force data was collected on two wheelchair users pushing at a self-selected speed on an ergometer. The data collected was projected onto the sagittal plane and input to the inverse dynamic model. The radial handrim force component was varied. Results were found to be consistent with previous studies [12, 16], in that a preferred force direction is not completely tangential, as this increased the shoulder torque demand for the same applied wheel moment. A sensitivity analysis was run using the experimental motion capture and tangential force data along with varying components of the radial force. It was found that the resultant force angle that minimized shoulder torque required shifts towards the radial direction near TDC, and was tangential during the initial and terminal part of the push.

Modified Four-Bar Mechanisms

Additional studies have been conducted in the 2D plane which use modified versions of a four-bar mechanism to model the wheelchair-user system. In one of the first inverse dynamic studies conducted using a real wheelchair setup on a stationary wheelchair ergometer, a hand segment was added to the general four-bar mechanism model by [17]. The study compared kinetic results for both wheelchair and non-wheelchair users pushing a wheelchair at one speed. A significant difference was found between the two tested groups, as wheelchair users produced lower peak tangential forces and a longer time to peak tangential force. Furthermore, it was found in all subjects that higher joint moments were present in the shoulder than any other joint [17].

In a variety of studies, a 2D upper extremity model was utilized in an inverse dynamic

analysis to understand joint power and power flow through the kinematic chain during wheelchair propulsion [13, 4, 18, 19]. The power flow calculation is illustrated in Figure 2.2. Three rigid bodies made up the dynamic model, which included the upper arm, forearm, and hand. The total mechanical energy of each segment was determined as the sum of potential and kinetic energy, whereas power flow was determined as the sum of distal and proximal rotational and translational power. This analysis found that for the first two-thirds of the propulsion phase, joint power was transferred downward to the hand and handrim. For the entire propulsion phase, distal joint power at the hand was negative, which equated to power transfer to the wheel. From the onset to mid-point of the recovery phase, the total mechanical energy decreased and joint power was transferred upward to the trunk, in which the shoulder extensors act eccentrically to absorb energy from the upper arm. This was explained as the user's strategy to conserve energy in the trunk for the next propulsion phase. Furthermore, integration of the power flow curves resulted in much larger energy transfer between segments than the total mechanical energy required to perform the propulsion cycle. This provided additional support that FEF values in the push phase are lower than 100%.
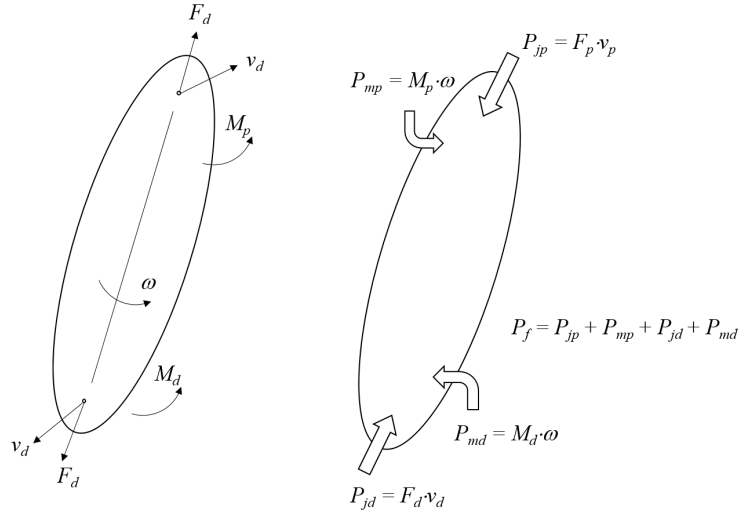
Figure 2.2: Power flow diagram of a segment used by Guo *et al* [4] re-created by the author. P_f denotes power flow which is composed of the joint and muscle power at the proximal and distal ends (denoted by subscripts p and d). M is the joint moment, v is the joint velocity, and ω is segment angular velocity

Additional insights using this analysis method found that eccentric muscle activity was

8

present close to hand release to help prepare for repositioning of the upper body in the recovery phase. In Price *et al's* study [18], both accelerative and steady-state experimental wheelchair propulsion data was input to an inverse dynamic analysis. The shoulder was found to have a higher joint power between acceleration and steady-state speed, whereas the elbow and wrist power was unchanged. Furthermore, power curves showed that the elbow had a tendency to act in an eccentric capacity during the later half of the propulsion stroke [18]. In Huang *et al's* study [19], the torso was added as an additional body segment to the 3-link model. In this analysis, variations in power flow and mechanical energy were investigated between different wheel camber angles between 0° and 15°. It was found that a larger discrepancy between power flow and mechanical energy estimates existed with a 15° camber angle, which indicated a larger energy loss. Furthermore, it was found that a greater energy cost was required in the 15° camber angle. It is clear from this study that an improvement in handling and stability with 15° camber comes at an energy cost to the user [19].

Simplified 3D Models

From the earliest days of wheelchair propulsion modeling, researchers quickly moved towards developing models capable of measuring joint torques in three dimensions. In the early 1990s, two research groups developed inverse dynamic models that allowed for an additional degree of freedom at the shoulder (abduction/adduction) and wrist (ulnar/radial deviation), which gave the ability to calculate out of plane joint torques [20, 21]. In [20], able-bodied participants pushed a wheelchair ergometer at constant speeds while 3D handrim forces and motion capture data from high speed cameras were collected. A three segment model was used, which included the upper arm and forearm modeled as axisymmetric bodies, and hand modeled as a sphere. Inertial parameters of the limb segments were selected based on anthropometric cadaver measurements obtained by [22]. It was found through this study that shoulder abduction was a passive movement related to the mechanics of the closed chain. Furthermore, by comparing EMG results of the biceps and triceps with elbow joint loading and angular velocity, eccentric activity in the elbow appeared to be minimal in the sub-maximal exertions by the subjects in the experiment. The primary muscles associated with shoulder torque generation were found to be the anterior deltoid and pectoralis major. Concentric shoulder torque production was once again found to be the highest among the three joints analyzed [20].

In similar fashion, [21] implemented a 3D inverse dynamic model to study fatigue effects in non-athletic wheelchair users. Model equations were generated symbolically in Maple. The authors used symbolic equation generation to decrease simulation time and in part to

9

reduce the chance of human error, which according to Leary *et al* [3], plagued the results obtained by Richter [2]. A custom wheelchair ergometer was used to collect handrim force data, and a 3D motion capture system was used to measure upper extremity kinematics. Each body segment coordinate system originated at its center of mass and inertial parameters for the upper body segments were derived from cadaver work by [23]. A recursive inverse dynamic approach was then used to calculate joint loading. Shoulder torque was found to be the largest contributor to the push phase, with no significant difference found between fatigue and non-fatigue pushing. Furthermore, EMG data was collected, which showed some overlap between biceps and triceps activation during the transition between elbow flexion and extension. Also, a correlation between dynamic strength and peak handrim force was strongest for the elbow extensors and shoulder flexors, suggesting that the triceps and anterior deltoid muscle groups may be most significant for wheelchair user strength development.

Many additional studies were conducted over the next decade using the model developed by Rogers [24, 25, 26, 27]. In [24], the model was validated by providing a close comparison to the results obtained by [20], in which the shoulder flexion moment was dominant over all other joint moments in all directions. The model was then used to compare the kinematic and kinetic results between two wheelchair user groups who demonstrated significant trunk flexion, known as the Flexion Group (FG), and those who did not, known as the Non Flexion Group (NFG). A kinematic analysis of fresh and fatigue pushing between groups found that FG users showed a 7–10% increase in trunk flexion when fatigued than in FG. It was suggested that the larger degree of trunk flexion in the FG group was a compensatory movement strategy that was not required by the FG group due to their increased fitness of key propulsion muscles, which was discovered in isokinetic dynamometer testing [25]. EMG data collected in the study found that the key muscle groups contributing to the wheelchair push showed an increase in activity in the FG group at fatigue, but a decrease in the FG group. It was suggested by Rodgers *et al* that this muscular fatigue demonstrated by the FG may place them at a higher risk for injury [25]. In a similar study, but this time comparing fatigue between wheelchair users and non-users, it was found that shoulder power was shifted from the shoulder to the elbow and wrist with fatigue in both groups. In addition, non-users were found to compensate fatigue with an increased trunk flexion compared to wheelchair users with limited torso mobility, who relied more on the wrist joints. The authors suggested that their risk to wrist injury is increased as a result of limited trunk flexion [26]. In a following large-scale study, wheelchair users were compared between groups with and without upper limb impairment. Significant differences were found in a wheelchair ergometer fatigue test in that users with upper-limb impairment demonstrated reduced compressive joint forces in all joints. This was the result of a higher

stroke frequency, lower power output and higher average FEF value [27]. The authors suggested that this wheelchair user group may implement these strategies as a protection mechanism against further upper-limb pathology to remain independent in activities of daily living. The studies by Rodgers *et al* suggest that subject-specific modeling to capture the limitations of different wheelchair users is necessary, and that generalization among all users may be error-prone.

Simplified 3D Models — Ball and Socket Shoulder Joint

Shortly after the development of the first out of plane inverse dynamic models came the inclusion of a ball and socket joint representation of the shoulder in 1998 by Kulig *et al* [28]. Shoulder kinetics were investigated using an upper extremity model with a torso, upper arm, forearm, and hand rigid body segments. These segments were connected by ball and socket joints. A major limiting factor of this study was that perpendicular handrim forces were not measured and assumed to be zero in the analysis, which has been found in a number of studies to be a false assumption. Another limitation was that shoulder joint torques were expressed in the global coordinate system, which Cooper *et al* [1] later showed to be significantly different from torques in a local reference frame. This made comparison between studies difficult.

The model developed in 1999 by [1] provided the foundation for 3D joint torque wheelchair propulsion modeling over the next decade. The purpose of the study was to investigate glenohumeral joint motion and shoulder net forces and moments in 3D, as well as to compare calculated joint kinematics and kinetics with three different coordinate systems: free coordinates referenced to the sternum, fixed coordinates restricting trunk movement to the sagittal plane, and global coordinates. These coordinates are represented in Figure 2.3. The rigid body model parameters were derived from a 15 segment model of the human body presented by Hanavan [23]. The model contained a sphere to represent the hand and circular cones to represent the upper arm and forearm. The shoulder, elbow, and wrist joints were represented by a ball and socket. A matrix approach was used to develop a numerically stable algorithm for efficiently computing three-dimensional net forces and moments about joints in the rigid body model, with the algorithms implemented in MATLAB (Mathworks, Inc.). To collect input kinematic and kinetic data for the inverse dynamic analysis, wheelchair users propelled their wheelchair over a dynamometer, in which Optotrak and SMARTWheel were used to obtain upper extremity kinematic and handrim kinetic data. The greatest similarity in shoulder joint kinematic and kinetic data were found between the fixed and free sternum based coordinate systems, providing evidence that analyzing trunk motion in the sagittal plane is sufficient. A number of spin-off

11

studies resulted from this work, which are summarized in Table 2.1.
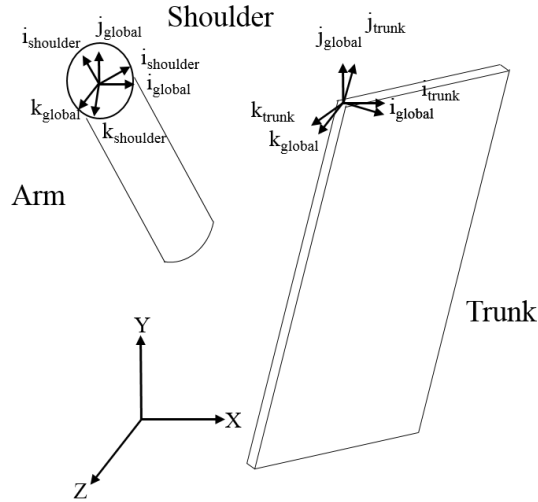
Figure 2.3: Coordinate system used by Cooper *et al* for the global and fixed analysis, re-created by the author

Table 2.1: Summary of inverse dynamic studies that use Cooper *et al's* model [1]

Study	Key Findings
Koontz *et al* [29]	• All peak shoulder moments were significantly larger for higher velocities • Peak shoulder forces occured before TDC
Mercer *et al* [30]	• Subjects who produced higher shoulder forces and moments were more likely to have shoulder pathology
Collinger *et al* [31]	• Peak shoulder joint loading occurred when the arm was extended and internally rotated • Peak shoulder forces occurred before TDC

Moon *et al* [32]	• Shoulder pain was correlated with low variability of peak shoulder forces across multiple propulsion cycles; the low variability results in a constant, isolated force which can lead to chronic pain
*Gil-Agudo *et al* [33]	• Wheelchair propulsion joint loads were lower on a treadmill than on an ergometer
*Gil-Agudo *et al* [34]	• Tetraplegic wheelchair users experience larger superior joint forces in all upper extremity joints than the paraplegic group; this could cause an increased risk of injury
*Gil-Agudo *et al* [35]	• Increases in peak medial and lateral forces were correlated with an increase in long bicep tendon thickness and decreased subacromial space; however, no change was found before or after the protocol
*Gil-Agudo *et al* [36]	• Active wheelchair users have larger shoulder joint forces in high intensity wheelchair propulsion than non-active wheelchair users • Able-bodied subjects had larger superior peak force; this could indicate adaptation of propulsion to minimize risk of injury in wheelchair users
**Desroches *et al* [37]	• Seat angle does not affect resultant shoulder moments; shoulder position with respect to wheel axle is a more important parameter to investigate

**Desroches *et al* [38]	• 90–100% FEF simulation resulted in significantly increased shoulder reactions and moments • Simulations with small increases in the tangential-radial force ratio provided improvement in propulsion efficiency without adding significant shoulder reactions and moments
**Desroches *et al* [39]	• Elderly subjects with larger FEF also had increased shoulder joint reactions and moments, which provides further support that a high FEF is not necessarily beneficial or feasible

*The model developed by Gil-Agudo *et al* used the same formulation and coordinate system as Cooper *et al* [1]. However, body segment inertial parameters were included in the model based on recommendations from Clauser [22].
** The model developed by Desroches *et al* used the same coordinate system as Cooper *et al* [1] but was developed using a wrench formulation and quaternion angles, which was used to avoid the determination of joint angle sequences for the inverse dynamic input.

3D Muscle Models

Even as 3D joint torque models were beginning to gain traction in wheelchair propulsion modeling literature, researchers from the Delft University of Technology were already beginning to develop the first high fidelity musculoskeletal shoulder model for applications to wheelchair propulsion in the mid-1990s. This model would soon become know as the Delft Shoulder model. The model would be used for the first time in a wheelchair propulsion study by Van Der Helm and Veeger [40] when the authors argued that a high level joint torque model was insufficient to make detailed insights into the causes of high strain in manual wheelchair propulsion. This pilot study was developed to gain insight into the shoulder muscles that play a dominant role in producing external torque and providing stabilization to the shoulder complex. At the time the study was conducted, methods were not available to measure dynamic scapular motion, so static measurements were done in the experimental testing of four healthy subjects. Individualized anthropometric and cadaver measurements were completed to include realistic parameters in the quasi-static model. Subjects resisted a backward turning moment of a wheelchair ergometer in different static positions. Handrim force measurements were recorded as well as EMG for 10 different

muscles of the right arm and shoulder [40]. This data was fed into the model, which used a finite element method in which all joints were spherical, and 95 muscle elements were used to represent 16 muscles. The results of the study found close similarity between EMG and predicted muscles forces, with the largest external moments produced in the sagittal plane of the glenohumeral joint and counterbalanced by major muscle groups such as the deltoideus, pectoralis major, and biceps. When dynamic measurement tools became more available to the research group, Veeger *et al* applied the Delft Shoulder model to an inverse dynamic analysis [41]. The model was expanded to included 31 muscles represented by 115 muscle elements. A minimum stress cost function was applied to obtain individual muscle forces. Key findings from the results of the model indicated that the subscapularis was the largest force producing muscle during the push phase, and that contributions of muscles to the propulsion moment almost always lead to compensatory contributions of other muscles [41]. Contact forces in the glenohumeral joint were not found to be any higher than those previously reported in other activities of daily living such as weight-relief lifting or reaching.

The inverse dynamic analysis of this model was subsequently applied in four different studies out of the Netherlands [42, 43, 44, 45], with each providing a unique analysis through the use of the finite element model, which was eventually expanded to 131 muscle elements to represent 31 muscles. Key findings included discovering that wheelchair propulsion muscle loads were significantly lower than other activities of daily living (weight-relief lifting, reaching, etc.) [42], and that no significant differences in muscle force or glenohumeral contact force were found between able-bodied, paraplegic, and tretraplegic subject groups in steady state wheelchair propulsion. This was a contradictory result when compared to previous studies that had found differences in shoulder joint loading between able-bodied and paraplegic subjects [26, 36]. Furthermore, a 100% handrim FEF input to the inverse dynamic model resulted in a 30% increase in overall physiological cost with the same performance obtained. The authors of the study [44] concluded that this was the result of the changing moment arms to produce force in different directions, which put more workload on the dominant shoulder muscles rather than the strong elbow extensors. In their most recent study, Vegter *et al* [45] tested non-wheelchair users over a 12 minute uninstructed training period and found an increased work load per push, decreased push frequency, and larger shoulder loads and moments. While this was beneficial in producing more power, interventions were deemed to be required to reduce the impact on the shoulder in novice wheelchair users in a rehabilitation setting.

Another muscle level shoulder model was developed and applied to wheelchair propulsion inverse dynamics by Dubowsky *et al* [46]. The AnyBody Modeling System was used, which is a software package that combines a solver for the multibody inverse dynamics

15

program and optimizers to solve the redundant muscle recruitment problem to calculate joint moments and muscle forces [46]. Initial segment and muscle properties were scaled to the Delft Shoulder Model, and included 21 rigid links, and 32 bilateral muscles represented by 225 muscle elements. The results of the model outputs from three different subjects (2 Spinal Cord Injury (SCI), 1 able bodied) showed strong validation to EMG recordings with a Mean Absolute Error (MAE) [1] calculation between experimental and calculated muscle activity of 0.165 across all muscles and subjects. Dubowsky *et al* states that there is no clear relationship between EMG amplitude and muscle force, so some uncertainty in model validation remains; however, this MAE value was similar to those previously reported [46]. Furthermore, total shoulder joint forces aligned well in magnitude to those found in previous literature [46]. An interesting observation made was the prolonged muscle activity measured in the triceps in a subject with limited trunk mobility, which was not captured computationally. It was hypothesized by the authors that this was a compensatory effect, and suggested that future work is necessary to further understand contraction/co-contraction effects in wheelchair propulsion.

The final model that will be discussed in this section was applied in wheelchair propulsion for the first time by Morrow *et al* [47]. A 3D rigid body upper extremity model of the right side of each subject was developed in Visual3D (C-Motion, Inc.), which used inverse dynamics to calculate shoulder loading. Using methods developed by [48], a musculoskeletal model was constructed for each subject in SIMM using kinematic marker and mass data. This software determined muscle attachment points relative to local coordinate systems of each segment, as well as muscle lengths, fiber lengths, and muscle orientations. This data was then input to a custom optimization muscle model in MATLAB. A Hill type muscle model was used to provide each muscle actuator with active and passive elements [49]. The minimization of muscle activation, maximum muscle stress, and summed muscle stress were used as optimization criteria to determine individual muscle and joint contact forces. Validation was done by comparing simulated muscle activity with EMG results. The results of the study were promising, and showed a good correlation between model results and subject-specific EMG data for all subjects. The results are similar to those determined in [46]. Furthermore, it was found that level propulsion resulted in significantly smaller mean joint contact forces than in ramp propulsion and weight relief conditions. One limitation of this study was that the optimization was done statically whereas the motions were dynamic.

---

[1] $MAE = \frac{1}{n} \sum\limits_{i=1}^{n} |MA_i - EA_i|$, where n is the number of push strokes, MA_i is the measured activity envelope at push stroke i, and EA_i is the estimated activity envelope at push stroke i

2.1.2 Forward Dynamic Models

While the large majority of wheelchair propulsion modeling to date has focused on quasi-static and inverse dynamic approaches, there has been an increase in the number of forward dynamic modeling approaches to predicting wheelchair user kinematics and kinetics in the last 8 years. A four bar mechanism was most recently used in a forward dynamic analysis of a wheelchair push by Masson *et al* [50]. The purpose of this study was to estimate the potential contribution of upper limb momentum to pushing by computing power with a passive model. Kinematic initial conditions of the wheel following hand contact were supplied to the model through data collection of wheelchair racing athletes. The experimental total wheel power was then compared to the momentum power transfer from the upper extremity to the wheel. Lagrangian equations of the four-bar linkage using a single generalized coordinate, the wheel rotation angle, were developed. Initial conditions of the shoulder and elbow angle were determined through kinematic constraint and Jacobian equations. The non-linear equations were then solved with the initial conditions using the ODE5 Dormand-Prince solver for a maximal 200ms time period. Overall, energy transfer to the wheel was dominated by muscle action over athlete momentum for the majority of the push phase in an accelerative movement. However, during fatigue movements, athlete momentum increased to its peak value where total work per push decreased. It was found that in the fatigue state, the athlete released the wheel much closer to the optimal athlete momentum angle than in the accelerative phase. Overall, the analysis showed that athletes in the experiment changed their push strategy during accelerative (speed increasing) or fatigue (speed decreasing) push phases to accommodate for an athlete momentum versus active force generation trade off. The authors suggested that the determination of an optimal pushing range should consider both pushing modes and include recovery phase dynamics as well [50]. Although this forward dynamic analysis did not require control inputs, it was the first paper in literature to implement a forward dynamic analysis on a planar model to study manual wheelchair propulsion.

Apart from [50], forward dynamic modeling of wheelchair propulsion has been dominated by Richard Neptune's research group out of the University of Texas. The first forward dynamic analysis from this group was completed by Rankin *et al* [51], and utilized the modeling techniques developed by [47]. The purpose of the study was to investigate the relationship between handrim forces and individual muscle contribution. The upper extremity musculoskeletal model was developed for the right side of the body, which included the trunk, upper arm, forearm, and hand. Body segment inertial parameters included were based on the work by [22]. To improve simulation performance, trunk motion was prescribed based on experimental data, and scapular and clavicular motions were prescribed

as functions of shoulder elevation. Passive torque functions were applied at the shoulder and elbow to limit extreme joint angles. Furthermore, 26 Hill-type musculotendon actuators were used to represent the muscles across the shoulder and elbow. Muscle actuators were put into 16 different muscle groups based on similar EMG data. To solve the muscle redundancy problem and produce optimal muscle activation inputs, a global optimization algorithm known as simulated annealing was used to minimize differences between simulated and experimental upper extremity kinematic data and tangential handrim forces. Further simulations were run that added terms to the objective function that minimized and maximized FEF. Excitation signals were defined as summed parameterized Henning patterns, which required six excitation parameters to be optimized for each muscle group [51]. Experimental data used in the simulations were collected for a single subject with paraplegia on a wheelchair treadmill. Handrim kinetic and upper body kinematic data were collected for propulsion at a self-selected speed. The forward dynamic simulations produced close comparison to experiment, with average errors of 1.12° and 2.36N between joint kinematics and handrim forces, respectively. Although percentage errors were not provided for the previous metrics stated, joint angles and handrim forces can be seen to vary from –50-80° and –5-40N in the figures provided by the authors for the experimental joint kinematics and handrim forces, respectively++. It was found that maximizing FEF shifted the work load to the rotator cuff, whereas minimizing FEF shifted work load to the elbow. It was determined that an optimal FEF becomes a balance between mechanical efficiency and minimizing upper extremity demand [51].

Since 2010, this research group has applied their research methods in five additional studies that are known to the author. These studies have investigated the mechanical energy transfer by muscles in propulsion [52], the effect of seat position on musculoskeletal demand [53] (will be discussed further in section 2.1.3), the accuracy of a static optimization versus dynamic optimization method [54], compensatory strategies in response to weakness of individual muscles [55], and most recently the influence different push and recovery patterns have on muscle power and stress in the upper extremity [56]. Results from these studies consistently found that the shoulder flexors are the most active during the push phase, while the extensors are most active in recovery. Furthermore, power contribution from the trunk was found to be minimal. In previous studies, significant power contribution from the trunk in propulsion was reported. However, the authors suggested that the use of SCI subjects in their study could explain this difference, where previous studies reporting these claims used able-bodied subjects [13, 4, 26]. Furthermore, it was concluded that a static optimization routine was insufficient for replacing the more accurate dynamic optimization, particularly for predicting movements with high amounts of co-contraction and muscle dynamic behavior [54]. In addition, weakness in individual muscles led to

18

an increase from synergistic muscle groups and decreased activity in antagonistic muscle groups. For example, large power shifts were found in the shoulder, in which deltoid and rotator cuff muscles compensated strongly for one another. The authors state that this could be a potential cause of injury, as these large compensations between muscle groups in the shoulder could lead to compromised glenohumeral stability and impingement [53].

2.1.3 Effect of Wheelchair Seat Position

One of the fundamental wheelchair parameters identified by the CSIO and previous literature [2, 3, 37, 57] was the position of the seat, and therefore the shoulders, relative to the wheel axle. In [2] and [3], the fixed shoulder position was adjusted vertically and the initial and final hand positions were calculated, which allowed for the shoulder and elbow angles to be determined at each time step. It was determined that a lower seat position minimized the required concentric shoulder torque but increased the required elbow torque. One anomaly that stands out in the results from [3] was the large amount of eccentric torque that was generated by the shoulder after 42% of push completion. This was not found in any previous studies reviewed. Munaretto *et al* [57] expanded their inverse dynamic analysis of the four bar mechanism [15] to include an analysis of varying shoulder positions. A wheelchair user with SCI propelled manually at a constant self-selected speed while handrim reaction force and 3D kinematics were recorded. The experimentally measured tangential handrim force was input to the simulation, with the Resultant Force (RF) direction adjusted by changing the magnitude of the radial force component. Performing an inverse dynamic calculation through a wide range of fixed shoulder positions and RF values allowed for a sensitivity analysis to be conducted to determine the effect on shoulder and elbow joint moments. The results agree with [3] that an increase in seat height increased shoulder torque while decreasing elbow torque. This study also found that the optimal RF direction became more tangential as the seat position decreased, which resulted in more flexed elbow angles. A unique aspect of this study was the additional focus on a limited tangential force component due to grip strength. At lower shoulder positions, the total joint moment cost was actually found to increase due to the inability to efficiently generate tangential forces.

Slowik *et al* continued the work developed by Rankin *et al* [51, 52] by using their forward dynamic model to investigate how seat position influenced musculoskeletal demand in wheelchair propulsion [53]. In the analysis, the push angle range was defined as a function of the seat height in the same way as [2, 3]. The cycle time was fixed to 1s at a constant push frequency to simulate a steady state push. Three propulsion cycles were simulated, which required the complete hand position throughout the simulation to be

prescribed over time. Furthermore, an average power output at the hand was prescribed as 10 W. A large range of seat positions were simulated, which included positions in a very large range of 90cm and 50cm for the horizontal and vertical directions, respectively. The optimization minimized the change in hand force and active joint moments. The results of the study found that muscle stress, co-contraction and metabolic cost were all minimized at anterior horizontal positions of the shoulder between -14cm and -3cm from the center wheel axle, and a superior offset of between -1cm and 3cm from the default 75cm height. This corresponded to a TDC elbow angle between 110° and 120°. This study contradicted previously reported recommendations that the seat should be moved as posteriorly as possible without affecting stability. Past a -10° hub-shoulder angle (posterior seat positions), it was found that upper extremity demand increased [53].

2.1.4 Forward Dynamic Modeling Efforts in Other Sports Applications

A number of forward dynamic models have previously been developed in various sports applications, and will be summarized briefly in this section. McNally and McPhee [58] recently developed a six degree-of-freedom biomechanical model for the application of analyzing the full golf swing. To simulate the swing in a forward dynamic analysis, parameterized joint torque generators were developed and included the eccentric-concentric dynamics of muscle to better represent actual muscle torque production. A continuous function represented by Equation 2.1 and displayed in Figure 2.4 was developed to mimic the maximum isometric activation joint torque, independent of joint angle, throughout the swing.

$$\tau_{pre}(t) = \tau_m \left(1 - e^{\frac{t_{on}}{t_{act}}} \right) - \tau_m \left(1 - e^{\frac{t_{off}}{t_{deact}}} \right) \tag{2.1}$$

where τ_m was the maximum possible applied torque, t_{act} was the time constant of activation, t_{deact} was the time constant of deactivation, and t_{on} and t_{off} were the amount of time that had passed since the torque was activated and deactivated, respectively. This equation was then scaled by a torque-velocity relationship represented by Equation 2.2 to produce $\tau_{V_c}(t, \omega)$, which is the velocity scaled concentric torque.

$$\tau_{V_c}(t, \omega) = \tau_{pre}(t) \frac{\omega_{max} - \omega}{\omega_{max} + \Gamma \omega} \tag{2.2}$$

where ω_{max} was the maximum possible angular velocity, Γ was an empirically derived scaling factor, and ω was the instantaneous angular velocity.
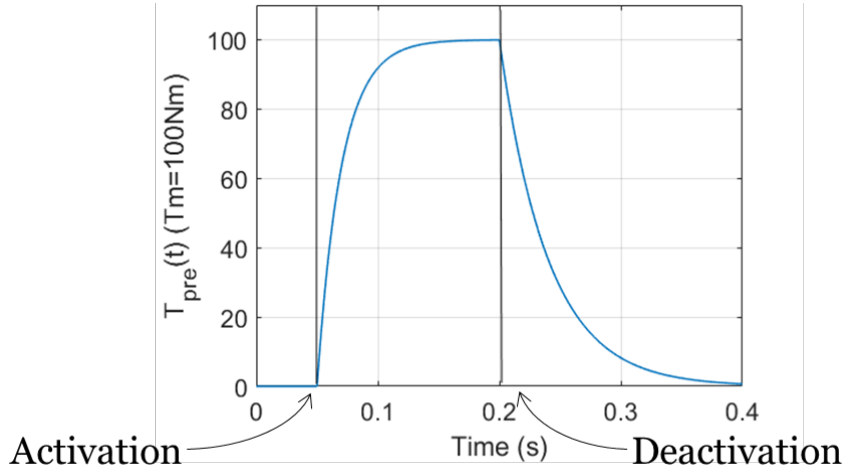
Figure 2.4: Exemplary plot of an activation curve using Equation 2.1

An objective function was minimized to determine the optimal timing parameters t_{on} and t_{off}, similar to the method employed in the forward dynamic simulations of Neptune's research group [51, 52, 53, 54, 55, 56]. Furthermore, passive torque functions were developed to represent the resistance caused by ligaments and soft tissues near joint limits. A relatively simple objective function was minimized to select the optimal timing parameters that maximized carry distance of the golf ball. Disregarding an optimized cost tracking function to experimental kinetic data allowed for a fully predictive solution of the golf swing to be determined.

Laschowski *et al* [59] developed a forward dynamic model of a Paralympic wheelchair curler. The model included a hip, shoulder, elbow and wrist joint in the sagittal plane, with the wrist modeled as a passive joint. With the inclusion of the throwing stick and curling stone, the modeled system included a closed kinematic chain. This resulted in a three degree of freedom model with one constraint equation. A direct-collocation optimization method was used to determine input joint torques to the model, which was implemented in the GPOPS-II software package. This method had the advantage of providing a neuromuscular input to the simulation without a constraint on input profile or number of activations and deactivations. A variety of objective functions were tested to determine the best overall comparison between predicted and experimental joint kinematics. Between individual objective functions that minimized the squared torque, joint angular velocity, angular acceleration, and joint power, it was found that minimizing the squared angular acceleration resulted in the lowest root mean squared error and fastest optimization time

21

[59]. Furthermore, subject-specific body segment inertial parameters were input to the model with the use of dual-energy-X-ray absorptiometry (iDXA) [60]. This provided an alternative to the standard method of using scaled anthropometric cadaver datasets.

Forward dynamic models of sports applications have also been developed by researchers at Loughborough university. These models were designed and implemented with the purpose of being subject-specific and validated by kinematic experimental data of the athletic movement or activity. One of the latest examples of this research is from Kentel *et al* [61], in which a subject-specific model of a one-handed tennis backhand stroke before and after impact was developed. The model consisted of 9 upper body segments and was constructed in ADAMS (MSC. Software Corp., California, USA). The racket was modeled as 9 point masses and the ball as a rigid sphere, which allowed for contact between the ball and any of the 9 points. The model consisted of 12 rotational degrees of freedom (three for the shoulder, two at the elbow, two at the wrist, three for the grip, and two for the racket deflection). Furthermore, 7 pairs of torque generators allowed for extensors and flexors to act in all degrees of freedom of the arm (shoulder, elbow, and wrist). One of the standout features of this research was the development of subject-specific parameters for the model. Isometric and isokinetic torque measurements with a Cybex Norm isokinetic dynamometer were used to identify 9 optimal parameters for in-house developed torque generator functions [62, 63]. These functions included eccentric and concentric dynamics of muscle, as well as the effect of differential activation and optimal muscle lengths. Parameterized and constrained quintic activation functions were used for each torque generator. Optimal timing parameters were determined by minimizing the root mean square difference between the kinematic experimental and simulation results before and after impact. Furthermore, anthropometric measurements were taken and Magnetic Resonance Imaging (MRI) was utilized to obtain body segment inertial parameters for the model. With the use of MRI, the moments of inertia could be estimated in ADAMS using bone density measurements from literature and MRI bone geometry data. The results provided good insight to the torque required in a tennis stroke by different joints, with the authors arguing that the model had sufficient complexity, without becoming overly complex, to accurately simulate a one-handed backhand stroke. However, it cannot be considered a fully predictive model due to the reliance of experimental cost tracking in the objective function, which could potentially lead to issues in producing 'what if' simulations that vary racket or swing parameters.

2.2 Opportunities for Improvement

To summarize the work dedicated to wheelchair propulsion modeling in the last 30+ years, far more research has been dedicated to quasi-static or inverse dynamic modeling than forward dynamic modeling. Forward dynamic simulations have been found to provide clear insights to the kinematic and kinetic intricacies of wheelchair propulsion, and recently have shown promise in the evaluation of 'what if' simulations that vary equipment parameters relied upon by the athlete [53]. As forward dynamic modeling is just in the early stages of wheelchair propulsion research, there are many opportunities that exist to improve this modeling work. Some of the key areas that can be explored are summarized below:

- Fully predictive forward dynamic simulations have recently been found to have the ability to draw both normative and descriptive comparisons to experimental data in different sports application settings. A forward dynamic model of wheelchair propulsion has yet to include optimized muscle input activations without the requirement of a prescribed time series hand or joint motion, and only one previous study has not required the use of an optimal tracking function [53]. The resistive torque that the wheelchair user must overcome has been previously studied and quantified by empirically developed equations in [64], which can be modified by the recent development of a continuous friction model by [65]. The addition of a simple wheelchair model could provide the necessary tools to develop a fully predictive wheelchair propulsion simulation. Furthermore, the first push has received limited attention in literature. It can also be considered as one the of the most important pushes in wheelchair basketball due to the high acceleration and maneuverability required [8], as well as the high joint strains required to overcome the inertial resistance of the system.

- A previous forward dynamic model for Paralympic curling utilized direct collocation in GPOPS-II software that provided an efficient method of optimizing a close-chain dynamic model similar to planar wheelchair propulsion models [59]. Direct-collocation can also be taken advantage of to generate activation profiles for each torque generator that are not represented by a pre-defined function (ie. Equation 2.1), which has been implemented in every active forward dynamic simulation to date in wheelchair propulsion applications.

- Recent forward dynamic studies have found the use of individualized body segment inertial parameters and torque data to aid in model validation. The CSIO generated subject-specific inertial parameters with the use of an iDXA analysis, which can be implemented in a forward dynamic model. Furthermore, limited studies have

included the torso segment in modeling wheelchair propulsion, and no studies to date have reported torso joint torques required in wheelchair propulsion. Data collected by the CSIO, as well as data reported in previous research [13, 4, 26], suggest that higher mobility wheelchair users utilize the torso significantly in wheelchair propulsion. The addition of an active torso joint and body segment could provide additional insight and accuracy to a forward dynamic model.

- Finally, the use of a Biodex System 4 Pro™(Biodex Inc, New York, USA) can be used with wheelchair Paralympic athletes for the first time to obtain personalized torque functions in a forward dynamic simulation.

2.3 CSIO Experimental Data

Data collected during phase one and phase two by CSIO were shared to aid in the research of this project. To briefly summarize the collection of the data used in this study, athletes pushed an adjustable wheelchair on top of a motor controlled dynamometer, which provided a track simulated and inertia adjusted wheel resistance [Keku Inc.]. This ergometer torque was determined from the equations developed by [64]. Athletes were instructed to push for 30 seconds at 80% effort. 3D motion capture technology was used to collect kinematic data of the upper body segments, which included data for the upper arms, forearms, hand, and wheel. 3D hand reaction forces were measured using SMARTWheel Technology.

Chapter 3

System Model and Body Segment Inertial Parameters

A 2D model was developed which was similar to the variety of planar models utilized in previous wheelchair propulsion studies and is presented in this chapter. The parameters for this model were obtained with the aid of data provided by the CSIO using a two-step parameter identification method. This 2D projected model was then validated through comparison of an inverse dynamic analysis of this model with the results obtained by the CSIO.

3.1   2D Projected Model

A five segment, joint torque driven 2D planar model was developed to represent the wheelchair-user system. This model was designed to require a relatively low number of dynamic equations of motion compared to previously developed models with tens of segments and muscle elements. The reduced number of equations of motion were intended to aid in the implementation of the fully predictive optimization forward dynamic method of this study by improving simulation time. The model was developed using MapleSim software (Maplesoft, Canada), which had the benefits of generating symbolic equations of motion that could improve simulation time further and reduce human error in equation generation [21]. Five revolute joints were included to represent flexion and extension of the torso, shoulder, elbow, and wrist, as well as the rotation of the wheel. The rigid bodies of the model represented the torso, upper arm, forearm, hand, and wheel, to which the hand

segment was rigidly attached. The model schematic can be found in Figure 3.1. It was found in CSIO experimental data that the hand grip angle relative to the radial component of the wheel was not constant throughout the push phase, which can be observed in Figure 3.2. The average contact angle was determined from a representative first push and was provided to the model as a fixed angle between the hand and wheel of 53.7°.

(a) Body segments and joint angles

(b) Joint torques and hand force directions
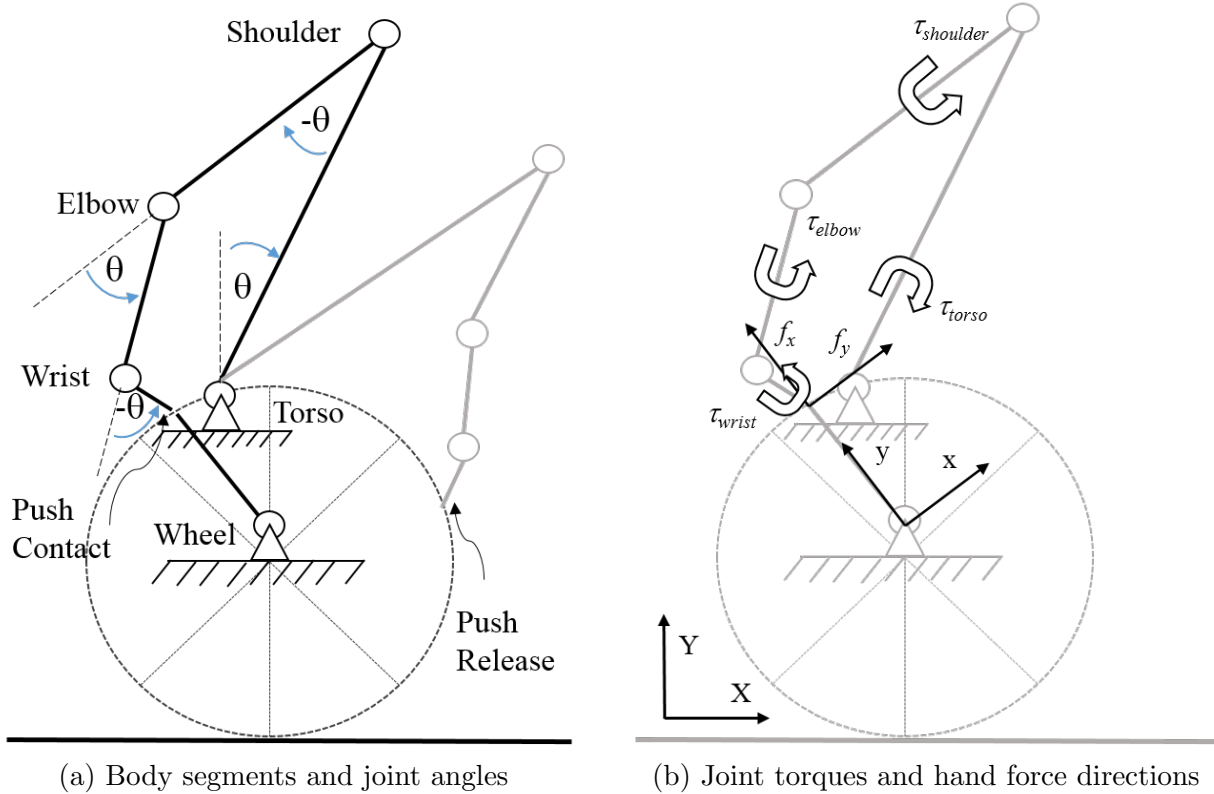
Figure 3.1: 2D Projected Model Schematic, where $\boldsymbol{\tau}_i$ represents the torque input to the model about each joint, and f_x and f_y represent the applied hand force in the normal (y) and tangential (x) direction

The resulting model contained two degrees of freedom and was represented by four generalized coordinates coupled by two algebraic constraints. Due to the planar condition of the model, the assumed camber angle of the wheel was 0°. Furthermore, the seat position was located -11.2cm posterior and $+18$cm superior to the wheel axis. This seat position was obtained from experimental marker data shared by the CSIO. Since the subject's hip joint was hidden from view by the motion capture system, the CSIO estimated the location of the hip by markers placed on the outside of the wheelchair. The center of the right wheel
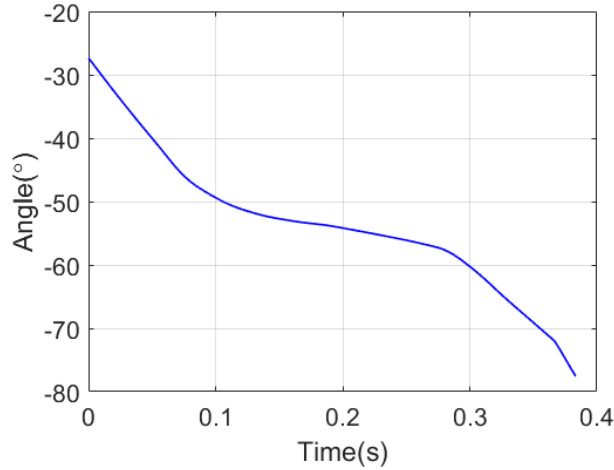
Figure 3.2: Hand angle with respect to the radial wheel component

was obtained through calculating the center of a triangle by three equally spaced markers on the wheel hub.

3.2 Body Segment Inertial Parameter Identification

3D Body Segment Inertial Parameters (BSIPs) were determined by the CSIO for each subject in their study to improve the accuracy of each inverse dynamic analysis in Visual3D. Body segment mass was measured by iDXA measurements of each subject, and center of mass and inertia terms were obtained by combining measurements with anthropometric charts obtained using a gamma-ray scanning technique of college-aged Caucasian males and females [66]. 3D motion capture technology was used to measure segment lengths. Due to the 3D movement of the arm that occurs during the push phase in wheelchair propulsion, the representative BSIPs for the 2D projected model are variable when viewed in a single plane. This was a problem that had to be overcome for the accurate representation of the 2D projected model, as BSIPs are constant values in a dynamic model. In order to obtain fixed BSIPs for the 2D projected model, optimal parameter values were selected that best matched the kinematic and kinetic properties provided by the CSIO BSIPs for the subject of this study (see section 4.1.1). The segment lengths of the arm were selected that allowed for the lowest error between the 3D and projected model hand position on the wheel. The kinetic BSIPs, which include the centers of mass, masses, and moments of inertia, were

selected that allowed for the lowest error between the 3D and projected model reaction forces at the handrim. However, in order to ensure that the measured reaction force is contributed entirely by the inertial properties of the arm segments, the model must be passive (no joint torques). The method employed is similar to the method used by [67].

Equivalent 3D Model

To facilitate the comparison between the 3D and 2D projected BSIPs in a passive environment, an equivalent 3D model to the one used by Visual3D was constructed in MapleSim. A modification was made to this model to provide a camber angle of $0°$ to the wheel. Although the experimental camber angle was $18°$, it was necessary for the hand path of the equivalent 3D model to fall in the same plane as the 2D projected model. The equivalent 3D model contained the same segments as in Figure 3.1; however the shoulder and wrist were modified with ball and socket joints. This provided flexion/extension, adduction/abduction, internal/external rotation of the shoulder, as well as flexion/extension, ulnar/radial deviation, and supination/pronation of the wrist. The model was represented by 6 generalized coordinates coupled by 3 algebraic constraints, and therefore contained 3 degrees of freedom. With the exception of the torso segment length, the 3D BSIPs obtained by CSIO for the subject of this study were used as the BSIPs for this model. As the hip joint was not modeled in Visual3D by CSIO, the distance between the experimental hip marker (fixed position on the chair seat) and shoulder markers were not constant. Therefore, the average of this distance was selected and input to the equivalent 3D Model. This model was simulated in MapleSim by a prescribed wheel and torso rotation, which allowed for a single push from rest to be generated. The prescribed motions were input by sinusoidal functions, which generated a sufficiently rich movement of the model. The frequency, phase shift, and amplitude of the sinusoidal functions were selected to provide a single push lasting 0.5s, as well as having initial and final conditions of the hand position and torso angle equal to an experimental push by the subject. These parameters can be found in Appendix B. The seat position was selected to be the same as described in section 3.1. The initial conditions were selected to be similar to that of an experimental push by the subject, and can also be found in Appendix B. Joint positions from the simulation of the equivalent 3D model were recorded and projected onto the sagittal plane, which allowed for projected joint angles to be calculated. Since the the hand segment was rigidly attached to the wheel, and the torso joint had a single degree of freedom allowing for rotation in the sagittal plane, the only variable BSIPs were found in the forearm and upper arm. This is represented by the projected segment lengths in Figure 3.3, in which the upper arm and forearm lengths are variable.

28
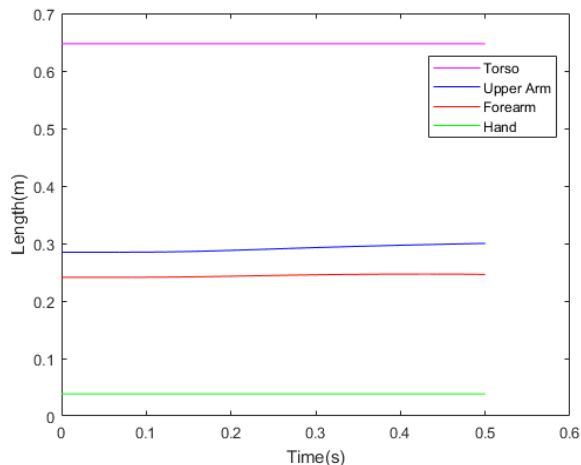
Figure 3.3: Experimental segment lengths projected onto the wheel plane (18°)

Two-step Parameter Identification

A two-step parameter identification procedure was completed that aimed to determine BSIPs for the 2D projected model that provided similar kinematic and kinetic results to those recorded and projected onto the sagittal plane in the equivalent 3D model simulation. The 2D projected model was modified by removing the wheel segment, which turned the model into an open kinematic chain by removing the constraint between the upper extremity and wheel. As represented by the segment lengths projected onto the wheel plane in Figure 3.3, the BSIPs in the 3D model simulation for the hand were constant and could be used directly in the 2D projected model, and therefore the hand segment was also removed in the open-chain 2D projected model. Although this was the same case for the torso segment, it was included in order to provide shoulder rotation to the modified 2D projected model. This left 8 unknown parameters in the open-chain 2D projected model, which are summarized in Table 3.1. The equations of the open-chain 2D projected model were exported to GPOPS-II for parameter identification using a direct collocation method (GPOPS-II and direct collocation are described further in section 5.1). The inputs to the open-chain 2D projected model were 2D forces in the sagittal plane at the distal end of the forearm (wrist joint location), as well as torque at the torso joint in order to match the prescribed torso motion of the equivalent 3D model simulation.

1. **Kinematic Identification**: The purpose of the first step in parameter identification

29

Table 3.1: Unknown parameters in the 2D projected model

Segment	Length(m)	Center of Mass(m)	Mass(kg)	Inertia(kgm^2)
Upper Arm	L_{UA}	COM_{UA}	M_{UA}	I_{UA}
Forearm	L_{FA}	COM_{FA}	M_{FA}	I_{FA}

was to determine segment lengths that resulted in the closest comparison between the wrist location of the equivalent 3D model simulation and open-chain 2D projected model. The unknown parameters in this step were L_{UA} and L_{FA}. The possible values that could be selected for L_{UA} and L_{FA} were constrained from 0–1.5 m, and the respective 3D BSIPs were selected as an initial guess. The values of the remaining parameters in this step were arbitrary, and the 3D BSIPs were input. The parameters were selected in the optimization to minimize the difference between the projected 3D model joint angles and 2D projected model joint angles, as well as the wrist position between both models. The torso torque and input wrist force were left unconstrained, however the joint angle and wrist position were constrained to their maximum value obtained in the 3D model simulation. The resulting wrist position and joint angles of the 2D projected model and 3D model are displayed in Figure 3.4a and 3.4c.

2. **Kinetic Identification**: The purpose of the second step in parameter identification was to determine the centers of mass, masses, and moments of inertia that resulted in the closest comparison between the reaction force of the equivalent 3D model simulation and open-chain 2D projected model. The unknown parameters in this step were COM_{UA}, M_{UA}, I_{UA}, COM_{FA}, M_{FA}, and I_{FA}. Centers of mass and masses were constrained from 0–1.5m and 0–10kg, respectively. I_{UA} was constrained from 0–1 kgm^2, whereas the I_{FA} was constrained from 0–0.4 kgm^2. As there were more parameters than equations, which resulted in a non-unique identification of parameters, it was found that this tighter constraint on I_{FA} was necessary to produce identified parameters that compared closely to the CSIO values. The parameters were selected in the optimization to minimize the difference between the projected 3D model joint angles and 2D projected model joint angles, as well as between the 3D model wrist reaction force and open-chain projected model input force. The torso torque was left unbounded, however the hand force was bounded to the minimum and maximum forces obtained in the 3D model simulation. The resulting hand force required is found in Figure 3.4d.

The identified parameters from both steps are presented in Table 3.2. The values identified for both segments are similar to the 3D BSIPs (see Appendix B). This can be seen further in the plots of Figure 3.4, in which the the 2D projected model was simulated with the 3D BSIPs. Although the resulting wrist position and reaction force compare closely between the identified and 3D parameters, the identified parameters produce a closer fit to the projected data of the 3D model simulation. The segment lengths and centers of mass are both lower than their 3D BSIPs counterparts with the exception of COM_{FA}, which was larger by 2cm. It was found that the identified segment lengths were equal to their average value from Figure 3.3. Both identified segment masses compared closely to their 3D BSIPs counterparts, with the forearm bass being 0.27kg larger. This may be the result of compensation for the larger difference in the moment of inertia values, as the 2D BSIPs were 0.00253 and 0.00301 kgm^2, which compared 3D BSIPs 0.000242 and 0.00688 kgm^2 for the upper arm and forearm, respectively.

Joint	Length(m)	Center of Mass(m)	Mass(kg)	Inertia(kgm^2)
Upper Arm	0.291	0.141	2.65	0.00253
Forearm	0.244	0.133	1.26	0.00301

Table 3.2: Identified parameters for the 2D projected model

(a) Joint Angle   (b) Joint Angular Velocity

(c) Wrist Position   (d) Wrist Reaction Force
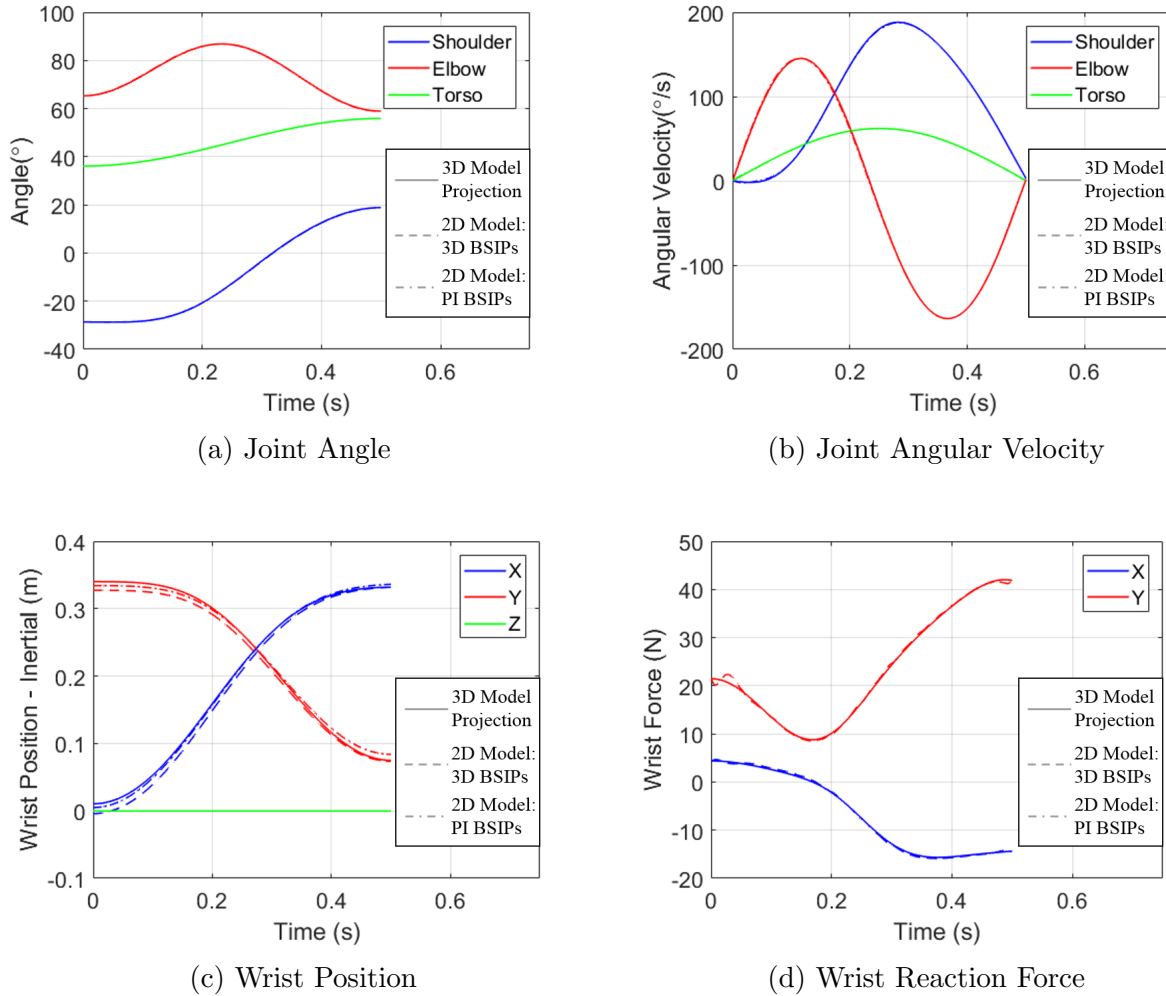
Figure 3.4: Results of the 2D model parameter identification

3.3 Inverse Dynamic Validation

To verify the parameters determined for the 2D projected model, an inverse dynamics analysis of the open-chain 2D projected model was performed and compared with the results obtained by CSIO in Visual3D. In this analysis, the hand segment was included in the open-chain 2D projected model. Experimental joint angles of a first push by the subject input to the inverse dynamic analysis were projected along the experimental camber wheel

plane. This was done by first projecting all upper body segments onto the wheel plane, and then calculating the angle between the projected segments at each time step. The push phase was identified by selecting data with a resultant hand force greater than 15N. The hand force input to the inverse dynamic model was projected to the sagittal, inertial plane. The optimal body segment parameters for the 2D model were used, and the inverse dynamic analysis was conducted in MapleSim. Resulting joint torques were filtered by a zero-lag 4th order Butterworth filter in Matlab, which was the same filter applied to the joint torque data calculated by the CSIO. For unknown reasons in the MapleSim software, the torso joint torque was unable to be determined. This bug in the software is currently being reviewed by Maplesoft. The torso torque was also not calculated by CSIO due to their lack of modeled torso joint. The input joint angle and hand force time histories can be observed in Figure 3.5.

(a) Inertial Hand Force   (b) Projected Joint Angle
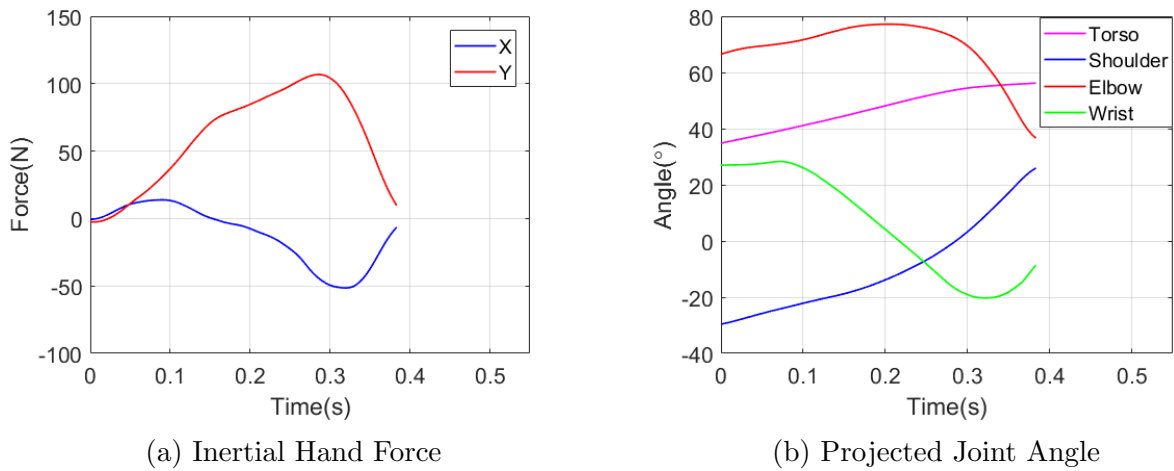
Figure 3.5: Input experimental kinetics and kinematics to the 2D projected model inverse dynamic calculation

The joint torques calculated in MapleSim are represented in the perpendicular axis to the sagittal plane. The shoulder flexion torque from CSIO was initially calculated in the local coordinate system of the torso. This torque was then transformed by determining a rotation matrix from the torso coordinate system to the inertial frame. The resulting torques between the 2D projected model and CSIO compare very closely to one another. However, this joint torque coordinate system transformation wasn't possible for the elbow and wrist joint torques as their reference coordinate systems were calculated internal to Visual3D and not available for output. From the virtual marker calibration data available, the local component of torque determined to be closest in alignment to the sagittal plane

33

for the elbow and wrist was plotted. This resulted in larger errors between joint torques in comparison to the calculated shoulder torque, however close similarities in profiles are still observed. The results of the inverse dynamic analysis are found in Figure 3.6. The 2D projected model results are indicated by the solid lines, and the CSIO Visual3D calculations are indicated by the dashed lines.
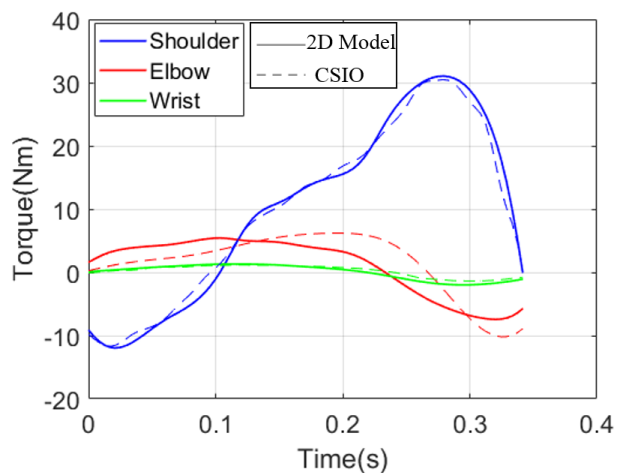
Figure 3.6: Comparing inverse dynamic results for the first push between the 2D projected model and CSIO Visual3D results

34

Chapter 4

Parameter Identification for Torque Models

The contents of this chapter explain the different methods employed to generate subject-specific torque generator functions for each joint of the model. Testing with a human dynamometer provided maximal isometric and isokinetic torque production of an elite wheelchair basketball athlete. The combination of this data with additional parameters from literature allowed for active and passive torque functions to be determined for each biomechanical joint in the model. Furthermore, a resistive torque function to mimic the torque provided by the wheelchair ergometer used by the CSIO was developed for input to the wheel joint of the model.

4.1　Biomechanical Joint Torque

To produce a forward dynamic simulation, joint torques are needed as inputs to the model so that the resulting kinematics of the simulation can be calculated. There are a variety of known constraints in human muscles that directly affect the amount of torque that can be generated about a joint. These constraints include force-velocity scaling, force-length scaling, non-linear passive force generation due to ligaments and connective tissue surrounding a joint, as well as muscle activation dynamics. The net torque produced by each joint is equal to

$$\tau = \tau_{act}(t)\tau_V\left(\omega\right)\tau_A\left(\theta\right) + \tau_P\left(\theta, \omega\right) \tag{4.1}$$

where $\tau_{act}(t)$ was the activation torque, $\tau_V(\omega)$ was the torque-velocity scaling, $\tau_A\left(\theta\right)$ was the torque-angle scaling, and $\tau_P\left(\theta, \omega\right)$ was the passive torque. The product of $\tau_{act}(t)\tau_V(\omega)\tau_A(\theta)$

was the net active torque produced by the biomechanical model. The activation of each joint torque, $\tau_{act}(t)$, could take any value between the upper and lower isometric torque at the optimal angle, and served as the control input to the model. For implementation in the forward dynamic simulation, both $\tau_V(\omega)$ and $\tau_A(\theta)$ were normalized by the maximum isometric torque of each joint. Therefore, the value of $\tau_V(\omega)$ at 0 deg/s was 1, and the value of $\tau_A(\theta)$ at the optimal angle was 1. Further constraints were necessary to obtain realistic activation mechanics to those determined from literature. Rate of Torque Development (RTD) is the studied phenomenon in which muscles are limited by how quickly they can reach maximum force [68]. To include this torque activation constraint in the model, it was necessary to bound the upper and lower limits of the rate of change of torque activation in the torso, shoulder, elbow, and wrist joint. The maximum and minimum activation and RTD bounds are further discussed in section 5.1.

4.1.1 Methods

Equipment Used

Joint torque testing was completed using the Biodex System 4 Pro™(Biodex Medical Systems, Inc, Shirley, NY). The Biodex is a multi-purpose computerized robotic dynamometer, and is one of the most widely used human dynamometers in sports and orthopedic medicine applications around the world. The Biodex measures the net torque produced by an isolated joint in the body, and can be used in both isometric and isokinetic joint conditions, which were both utilized in the testing of this study.

Subject Data

One female subject was used for the testing protocol of this study with a non-spinal lower body injury, and will hereby be referred to as wcB003 (28yrs, 170cm, 67kg, Class 4-4.5). wcB003 is an active member of the National Women's Wheelchair Basketball Team. wcB003 had no prior experience with a Biodex system, and did not report upper body pain during the testing protocol. Ethics approval for the testing protocol was obtained from the University of Waterloo Office of Research Ethics.

Data Verification

There have been many previous studies measuring isometric and isokinetic knee torque that reported a discrepancy between angles and angular velocities measured by the dy-

namometer crank and the actual biomechanical joint kinematics [69, 70, 71]. Isometric torque is the torque produced at a constant angle, whereas isokinetic torque is the torque produced at a constant angular velocity. The recommendations from these studies suggest the need for a secondary system to measure accurate joint kinematics synchronized with Biodex crank torque data. However, these studies did not report the need for this additional data collection for measurements of upper body joint torque. Preliminary testing was conducted to verify if the additional data collection was necessary to the accuracy of the current study. The joint angles used in this section are depicted in Figure 4.1.
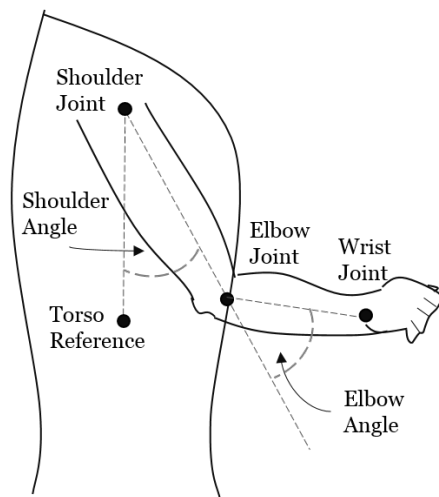
Figure 4.1: Joint angle definitions used in the Biodex, ProAnalyst, and goniometer measurements

In operation of the Biodex, the anatomical joint center is required to be positioned directly in line with the joint center of the Biodex crank. This led to difficulties in measuring accurate shoulder joint kinematics during operation of the Biodex, as the field of view of the torso, joint center, and upper arm were partially or completely blocked by the dynamometer. Without access to a multi-camera motion capture system, a small and portable video camera (iPhone SE, 30Hz, Apple Inc.) was positioned on the inside of the dynamometer slightly above the crank. This provided a limited but suitable view of the upper extremity during Biodex operation, with the center of the field of view pointed at the shoulder joint. This setup allowed for digitized upper body landmarks to be measured in post-processing using motion analysis software ProAnalyst (Xcitex, Inc) to obtain shoulder joint kinematics. Following ISB recommendations as closely as possible given the circumstance of the test [72], black markers were placed on the angulus acromialis and lat-

eral epicondyle in order to identify the approximate shoulder joint center and elbow joint center, respectively. The midpoint of the approximate position of the T8 and sternum was selected in post-processing to estimate the position of the torso segment. To improve the field of view of the elbow, shoulder movement was done in a supine position. A representation of the data processing in ProAnalyst is provided in Figure 4.2. The two blue lines connect the shoulder and elbow joints, as well as the shoulder and torso joints. In this movement, isokinetic concentric and eccentric shoulder flexor torque was measured at 180 deg/s.
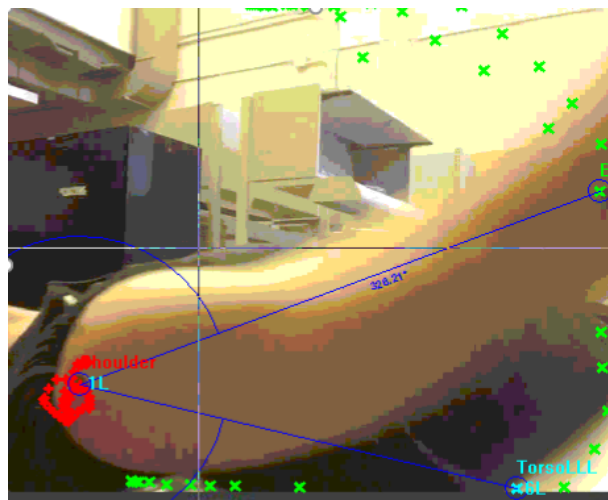
Figure 4.2: Screenshot of the ProAnalyst digitization interface

It can be seen by the time history red '+' markers representing the shoulder joint center that the joint was not stationary throughout the movement. This is a limitation of the Biodex, as it was difficult to accurately orient the shoulder joint center with the Biodex crank center throughout the movement. It can also be seen from the time history green 'X' markers representing the elbow joint that the joint was not always in the camera field of view. A reference point on the upper arm was noted and used to approximate the line to the elbow joint.

It can be seen in Figure 4.3 that the joint angle measured by the Biodex crank compares closely to the measurement obtained in ProAnalyst in the zones of interest (isokinetic region). These are represented between the first and second green line, as well as between the third and fourth green line. The angular velocities are similar between the Biodex and ProAnalyst; however discrepancies can be seen in the isokinetic regions. With the

38
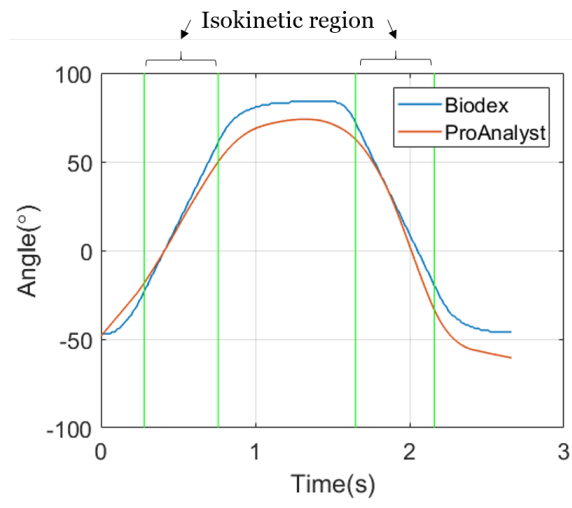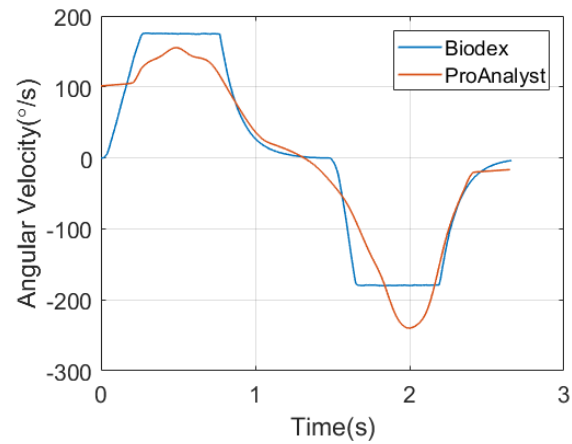
(a) Joint Angle

(b) Joint Angular Velocity

Figure 4.3: Comparing shoulder joint kinematics between ProAnalyst and Biodex

limited certainty of the ProAnalyst measurement of the shoulder joint kinematics due the lack of validation of this method, a more robust and accurate method was applied to the elbow joint by using an electrogoniometer (REF SG110, Biometris Ltd., Newport, UK) as the secondary measurement system. Three different angular velocities were tested in an isokinetic elbow flexion/extension movement. The raw output of the goniometer was voltage, which required to be converted to an angle. A calibration procedure was carried out in which the electrogoniometer was displaced while attached to a digital goniometer. The known angles were linearly regressed against voltage, which established a constant multiple to be used. Furthermore, an offset was applied to the raw output to ensure a zero-degree angle was accurately measured.

It can be seen in Figure 4.4 that the resulting angles and slopes are very similar between the Biodex and electrogoniometer for all three angular velocities, particularly in joint angles of 0–100°. Based on this preliminary test, the Biodex crank angle measurement was used without the addition of secondary data for the elbow. It is likely that the Biodex crank angle measurement was more accurate for upper body applications due to a rigid grip handle that was used to connect the human-dynamometer system. Due to the challenges of collecting confident secondary shoulder joint kinematic data, as well as the fact that the shoulder used the same grip attachment as the elbow, the Biodex angle measurement was also used for the shoulder in the athlete testing protocol. To minimize further discrepancy that was likely caused by shoulder joint translation, wcB003 was instructed to keep their back and head against the seat rest, as well as their elbow and wrist joint in a straight and locked position throughout the shoulder tests.

Testing

The testing protocol was broken into isometric and isokinetic testing of the shoulder and elbow of the dominant side of the body. In this case, the right shoulder and elbow were tested. A warm-up was completed prior to the testing of either joint. This portion of the protocol consisted of 2 sets of 5 reps of a flexor isokinetic concentric/eccentric movement at 50% maximal effort. The first set was performed at 60 deg/s, and the second was performed at 120 deg/s. This session served a dual purpose to the testing protocol, as it provided the subject a physical warm-up to improve the chance of exerting a maximal effort in the proceeding tests. It also provided a short training session to the athlete to help overcome the learning curve of exerting effort in an eccentric movement. Following the warm up period, isometric testing commenced at 8 different angles for the shoulder ($-40°$, $-20°$, $0°$, $20°$, $40°$, $60°$, $80°$, and $100°$), and 9 for the elbow ($0°$, $15°$, $30°$, $45°$, $60°$, $75°$, $90°$, $105°$, $120°$). The subject exerted a single 5 second maximal flexor activation against

40
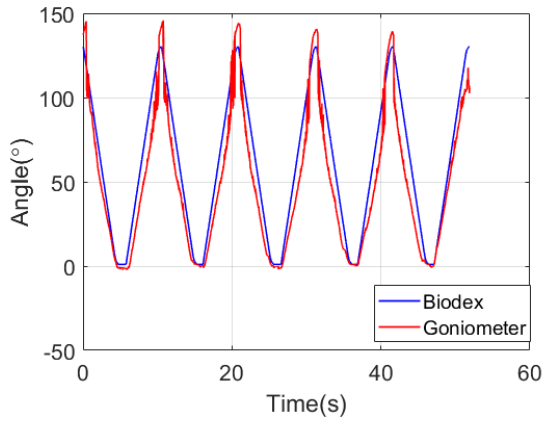
(a) 30 deg/s
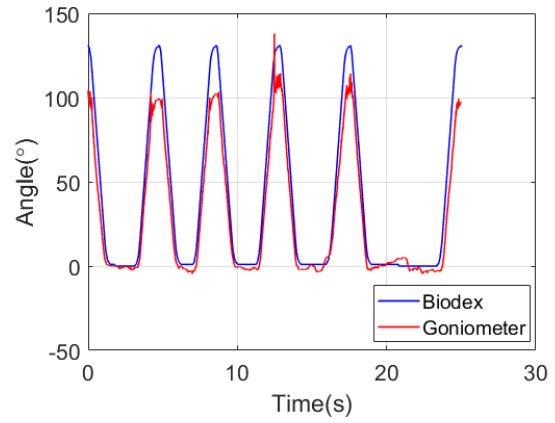
(b) 120 deg/s
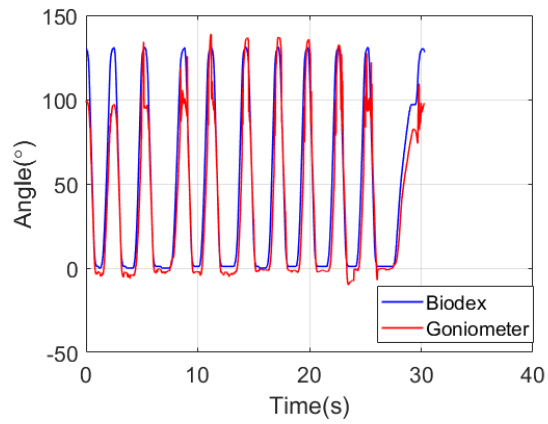
(c) 240 deg/s

Figure 4.4: Comparing elbow joint kinematics between an electrogoniometer and Biodex

41

the stationary crank, which was immediately followed by a 5 second maximal extensor activation. A minimum of 15 seconds of rest was given between joint angles, with longer breaks taken by the subject when needed to ensure maximal exertion in the following rep. Three minutes of rest was provided between isometric and isokinetic testing. The first segment of isokinetic testing involved concentric and eccentric activation of the flexor muscle group. The subject exerted a maximal effort for 2 reps of a full concentric/eccentric cycle for each velocity tested (30 deg/s, 75 deg/s, 120 deg/s, 180 deg/s, 240 deg/s, 300 deg/s, and 360 deg/s). Increased rest was provided between sets due to the larger effort required in isokinetic testing. Even though the Biodex was able to test up to 400 deg/s, it was found that angular velocities above 360 deg/s were difficult and inconsistent for wcB003 to obtain. The isokinetic testing was repeated for the extensor muscle groups. Upon the completion of the shoulder testing, the described protocol was repeated for the elbow.

Data Processing

Synchronized crank torque, angular velocity, angle, and time data was extracted from the Biodex software package following the completion of the testing protocol. Exemplary results of an isometric and isokinetic test are displayed in Figure 4.5.

(a) Isokinetic Elbow Torque at ±120 deg/s   (b) Isometric Elbow Torque at $\pm105°$

Figure 4.5: Exemplary isokinetic and isometric elbow torque

The analysis of isokinetic data consisted of a windowing function applied by Biodex software to remove any torque data that fell below 70% of the target angular velocity.

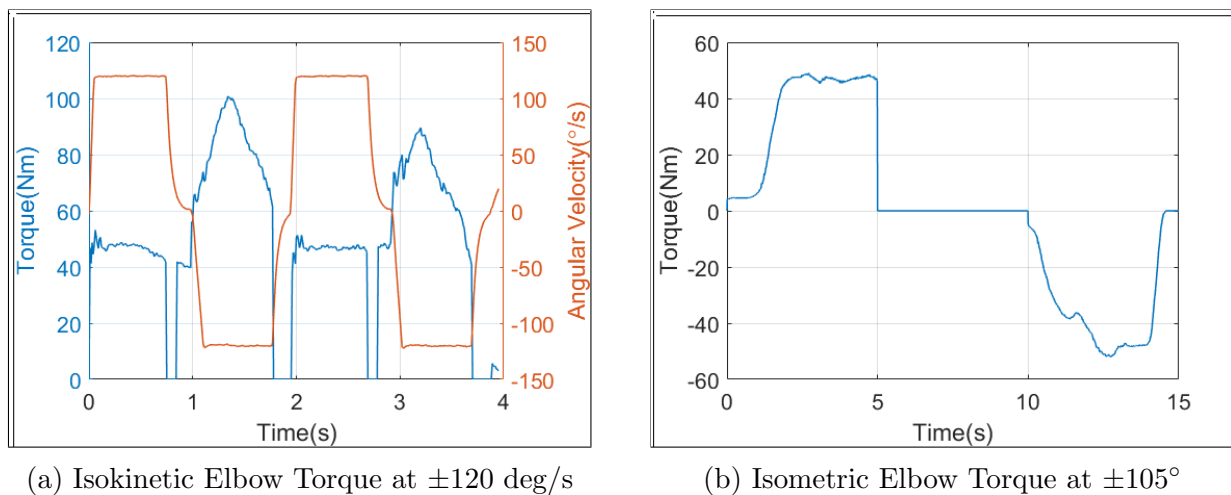Furthermore, the concentric and eccentric reps consisting of the maximum torque achievement were selected, with the other reps discarded. The maximum and average joint torque for each of the selected reps was determined for each angular velocity trial. Following the method used by [63], the maximum torque values were then regressed against the average torque values and replaced by the regression values to give a maximal data set. The purpose of this analysis was to provide a set of 14 maximal joint torques and angular velocities that had less noise than the raw data, and were independent of joint angle [63]. A similar method was used in the isometric torque data analysis. A selected range of data surrounding the peak torque achievement in both activations were selected for each trial. The subject was instructed to ramp up to maximum torque, sustain a maximum torque for approximately two seconds before ramping back down. This analyzed range was manually selected for when the subject finishing ramping up and started ramping down. The maximum and mean torque were determined, with a linear regression analysis completed to obtain a "maximal" set of torque and angle data. The primary purpose of this analysis for the isometric data was to eliminate noise in data. This data processing allowed for the construction of a single isokinetic plot and isometric plot for each of the flexor and extensor torque activations. These plots can be observed in Figure 4.6 and 4.8 .

From Figure 4.6, the isometric torque plots produced by Garner and Pandy [5], which represent an average of experimental studies summarized in their study, were included to provide a comparison to the plots generated in this study. Since maximum torque generation can vary considerably between individuals, the comparison to data presented by Garner and Pandy was only done qualitatively. To demonstrate this large variability, the data summarized by Garner and Pandy for shoulder flexion torque (this data makes up the mean calculated by Garner and Pandy and plotted in Figure 4.6a) was plotted alongside the data of this study in Figure 4.7. This data includes experiments conducted by Garner and Pandy, Otis [73], Reiser [74], and Winters [75].

For the shoulder tests, similar profiles were generated in that the maximum torque produced generally increased as flexion angle decreased. Garner and Pandy did not report negative flexion angles; however it was found in this study that these angles resulted in larger isometric torque capability by wcB003 than for positive angles. In addition, the extension tests produced a quadratic shape in that joint torque production was maximized at an optimal angle, with torque generation decreasing on either side of this optimal angle. This quadratic shape was found in the isometric elbow torque data in both the results of this study and those reported by [5]. Repeated testing of the subject over multiple days could have helped remove suspected outliers in the data, such as the torque produced at 20° in shoulder flexion or 90° in elbow extension. Furthermore, larger deviations in absolute torque values were observed in Figure 4.6a and Figure 4.6b.
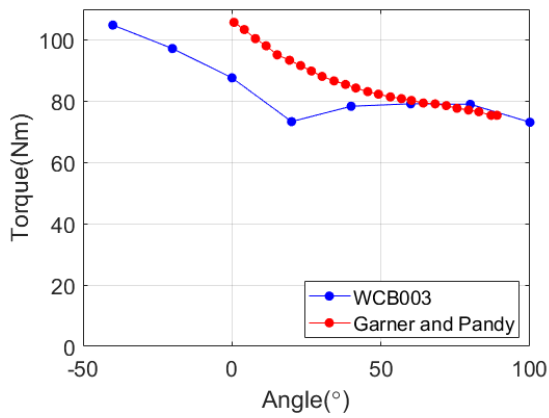
(a) Shoulder Flexion
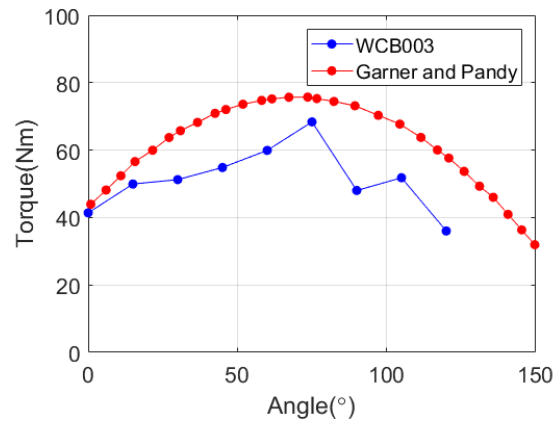
(b) Elbow Flexion
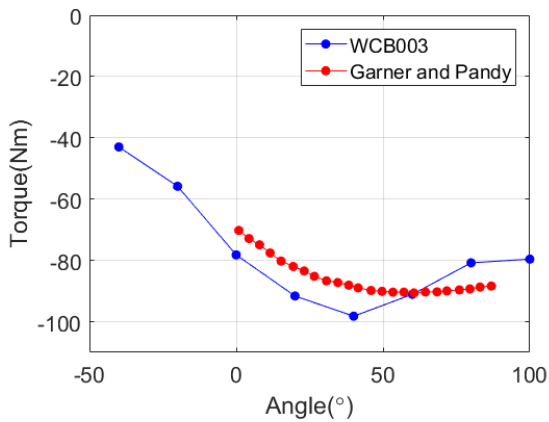
(c) Shoulder Extension
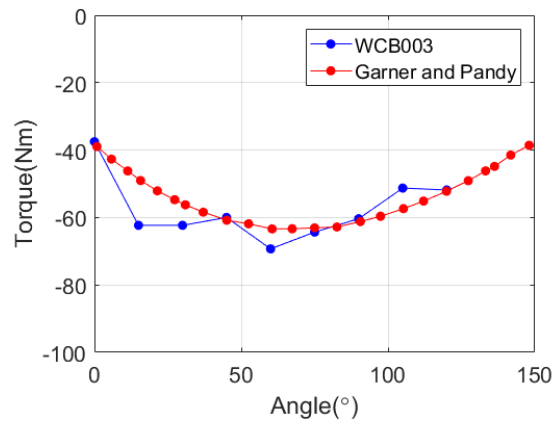
(d) Elbow Extension

Figure 4.6: Comparison between maximal isometric data sets obtained in this study and reported by Garner and Pandy [5]

44
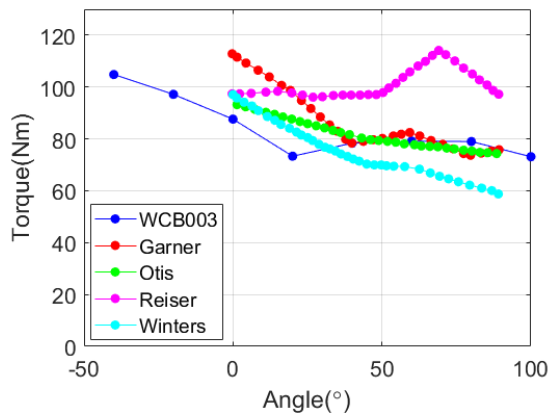
Figure 4.7: Comparison between maximal shoulder flexion isometric data sets obtained in this study and all experimental data summarized by Garner and Pandy

All isokinetic plots resulted in functions with larger torques in the eccentric region than in the concentric region. In general, as the angular velocity increased, the torque production decreased. Furthermore, eccentric torque was found to plateau at torque values larger than those produced concentrically. These observations compare closely to well-known muscle dynamic behavior. However, the eccentric torque values were not always larger than those produced in the isometric test. Eccentric torques produced by the shoulder flexors and elbow extensors were much lower than the isometric value, when the maximum eccentric torques is typically considered to be 1.3–1.5 times larger [63, 71, 58]. One hypothesis for this result was that it can be challenging to produce maximal eccentric torques using a human dynamometer, and that further Biodex training sessions would be needed to produce more representative results to known maximal muscle dynamics.

Parameter Fitting

A seven-parameter function, $\tau_V(\omega)$, was used to express maximum voluntary torque as a function of angular velocity. This function was developed by Yeadon *et al* [63] and provided a rotational equivalent to the hyperbolic shape of concentric torque produced by Hill [49], as well as a rectangular hyperbola to represent the eccentric phase. The parameters include τ_m, τ_0, ω_{max}, and ω_c, which represented the maximum torque in the eccentric phase, isometric torque, angular velocity corresponding to zero torque production, and the vertical asymptote of the Hill hyperbola, respectively. A piecewise function, $\tau_{Vs}(\omega)$, represented

45
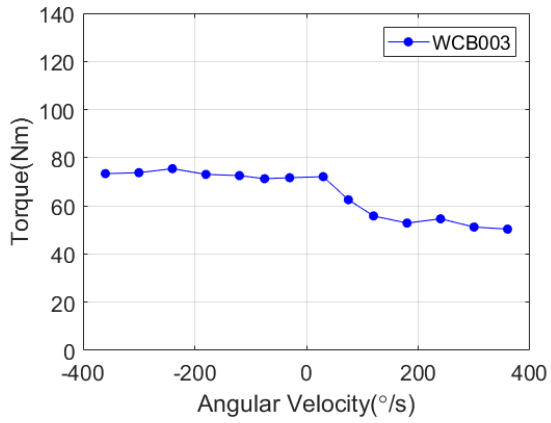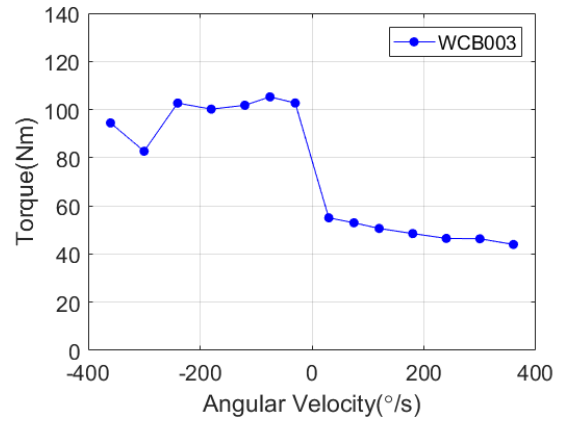
(a) Shoulder Flexors

(b) Elbow Flexors
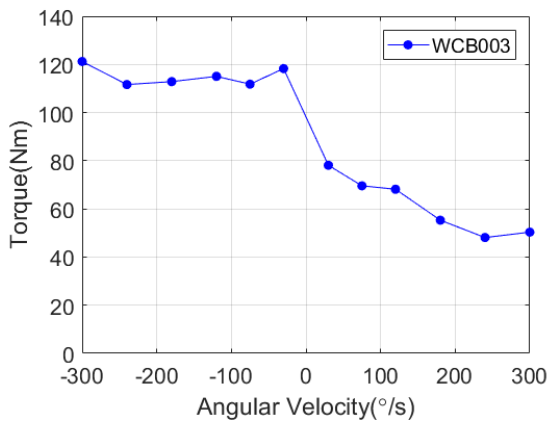
(c) Shoulder Extensors
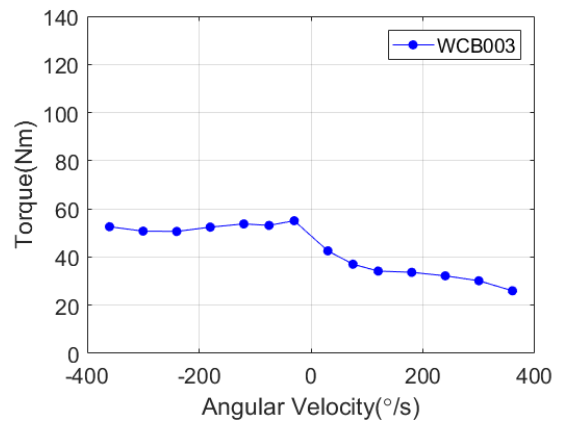
(d) Elbow Extensors

Figure 4.8: Maximal isokinetic data sets

the torque-angular-velocity relationship for the concentric and eccentric phases:

$$\tau_{Vs}(\omega) = \begin{cases} \frac{C}{\omega_c + \omega} - \tau_c & \text{if } \omega \geq 0 \\ \frac{E}{\omega_e - \omega} - \tau_m & \text{if } \omega < 0 \end{cases} \tag{4.2}$$

where $\tau_c = \frac{\tau_0 \omega_c}{\omega_{max}}$, $C = \tau_c(\omega_{max} + \omega_c)$, $\omega_e = \frac{\tau_m - \tau_0}{k\tau_0} \frac{\omega_{max}\omega_c}{\omega_{max}+\omega_c}$, $E = -(\tau_m - \tau_0)\omega_e$, and k represented the slope of the eccentric and concentric functions at zero angular velocity. This value was set to 4.3 [63]. The function $\tau_{Vs}(\omega)$ was then multiplied by a differential activation function, $a(\omega)$, consisting of three parameters, which is found in Equation 4.3, to produce $\tau_V(\omega)$ from Equation 4.2. The main idea of the differential activation function was to limit the activation torque at high eccentric velocities, which was previously found to be a protection mechanism of muscle and included in Yeadon *et al's* torque function [63]. The parameters included a_{min}, ω_1, and ω_r, which represented the lowest level of activation in the eccentric phase, the angular velocity at the point of inflection, and the range of which the ramp from a_{min} to a_{max} occurred. The assumed value of a_{max} was 1.

$$a(\omega) = a_{min} + \frac{(a_{max} - a_{min})}{\left[1 + e^{\left(-\frac{\omega - \omega_1}{\omega_r}\right)}\right]} \tag{4.3}$$

The resulting seven-parameter function is represented by Equation 4.4.

$$\tau_V(\omega) = \tau_{Vs}(\omega)a(\omega) \tag{4.4}$$

The 7 unknown parameters were determined by fitting the torque-angular-velocity function to the maximal data sets generated for the subject displayed in Figure 4.8. Parameters were bounded and provided an initial guess, which were based on the values used by Forrester *et al* [71]. The guess points for τ_0 were selected from interpolating the isokinetic plots at zero angular velocity. The value for τ_m was set to be proportionate to 1.4 times the value of τ_0 in the parameter identification scheme. To identify these parameters, a non-linear least-squares solver was used in MATLAB called lsqnonlin. In [71], it was explained that difficulties are typical in obtaining consistent maximum voluntary contractions from human participants. Therefore, a weighted simulated annealing function was applied in [71] that forced the majority of experimental data beneath the fitted torque function. The amount of experimental data below the curve varied from 73-92% for each participant. For this study, the use of lsqnonlin allowed for weightings to be placed on the value of the function at each experimental data point. Using this method, a larger percentage of experimental data was forced below the fitted torque function for each joint activation

than what was achieved using a non-weighted computation. A comparison of a weighted versus non-weighted fitted function can be found in Figure 4.9. The complete set of fitted torque-angular-velocity curves can be found in Figure 4.10. From the data in Figure 4.10a to 4.10d, the coefficient of determination (R-squared) was between the experimental data and fitted function and was found to be 0.906, 0.964, 0.855, and 0.947, respectively. Due to the lower R-squared value determined for the elbow flexors, it would be beneficial in future work to explore additional bounds on function parameters in the fitting process to more accurately represent the experimental data.
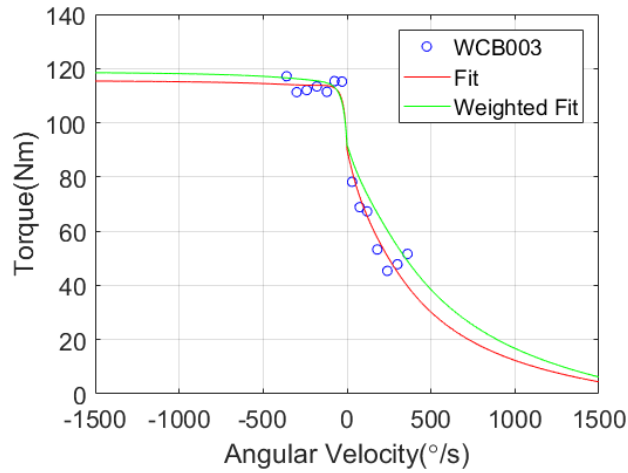
Figure 4.9: Weighted versus non-weighted curvefit for the shoulder extension isokinetic maximal data set

For the torso and wrist joints in the model, a generic torque-velocity function was utilized that has been previously used extensively in golf swing predictive simulation research [76, 77, 78, 58, 79]. This function was discussed previously and is represented by Equation 2.2. To include the torque-velocity effect in eccentric torque generation, $\tau_{V_e}(t, \omega)$, [58] developed a rotational equivalent to the eccentric force-velocity equation derived by Van Soest *et al* [80], which is displayed in Equation 4.5. The concentric torque function was described earlier in Equation 2.2

$$\tau_{Ve}(\omega) = \frac{(1 - \tau_r)\,\omega_{max} + S\tau_r\omega\,(\Gamma + 1)}{(1 - \tau_r)\,\omega_{max} + S\omega\,(\Gamma + 1)} \tag{4.5}$$

where ω was the joint's instantaneous angular velocity, ω was the shape factor affecting scaling curvature, S was the slope-factor determining smoothness between concentric and
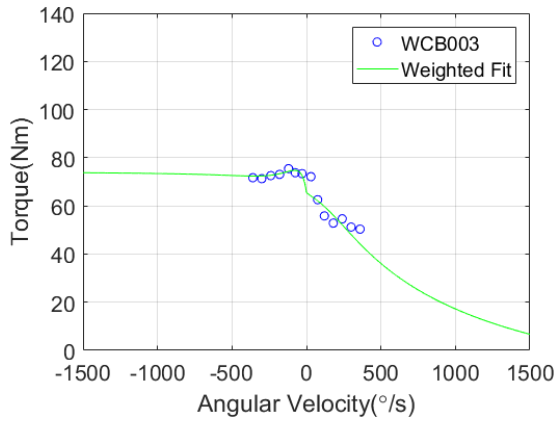
(a) Shoulder Flexors
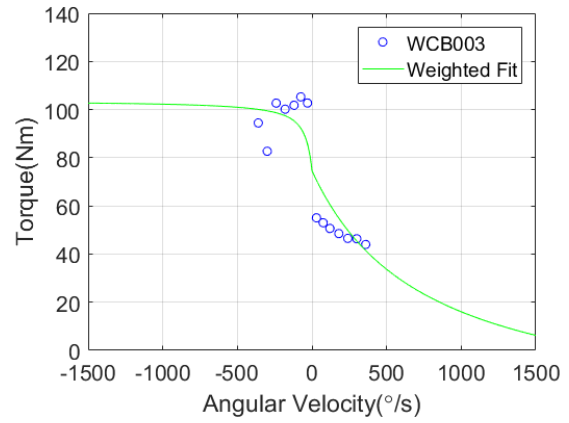
(b) Elbow Flexors
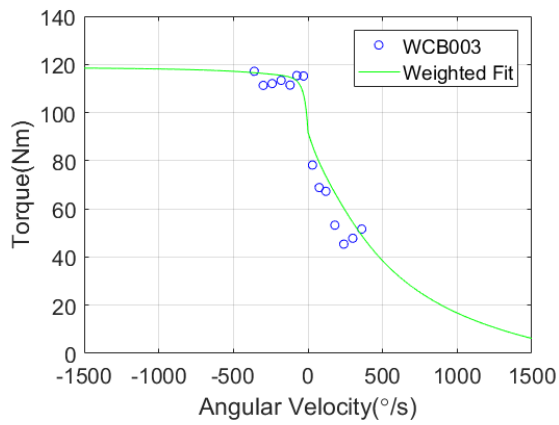
(c) Shoulder Extensors
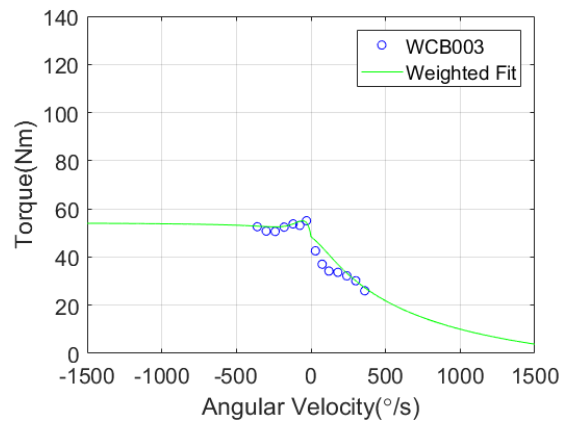
(d) Elbow Extensors

Figure 4.10: Equation 4.4 fit to the maximal isokinetic dataset

49

eccentric torques, and τ_r was the ratio between maximum eccentric and concentric torque. Values used in this study were the same as those used by [58].

A second order polynomial was used to express $\tau_A(\theta)$, which was similar to the functions used by [62, 71]. The maximal data sets for flexor and extensor isometric torque for each joint were normalized by the maximum isometric torque at the optimal angle of each joint and fitted to a second order polynomial using polyfit in MATLAB. For the unique profile produced by the flexor muscles of the shoulder, a fourth-order polynomial was used. Generic data for the wrist joint was obtained from human dynamometer data collected by [5] from three healthy subjects. Due to the generic application of this particular torque function and high similarity between flexor and extensor wrist curves, the flexor curve was used for both activations. A torso torque-angle function was not included in the model, as relevant experimental data in literature could not be found and the Biodex does not support torso tests. The plots for the fitted functions can be viewed in Figure 4.11. The fitted parameters can be found in Appendix A. The corresponding R-squared value for Figures 4.11a to 4.6d were 0.965, 0.729, 0.946, and 0.718, respectively. The quadratic polynomial proved to be a better fit for the shoulder extensor maximal data than for the elbow flexor and extensor data.
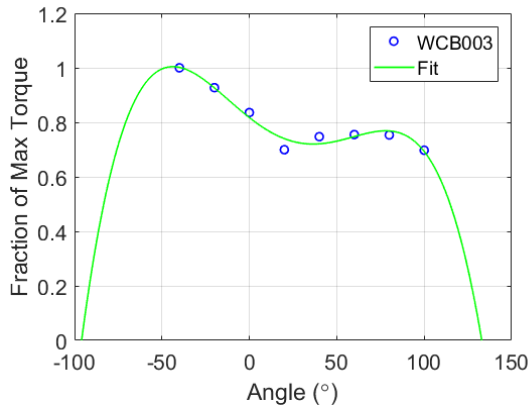
(a) Shoulder Flexors
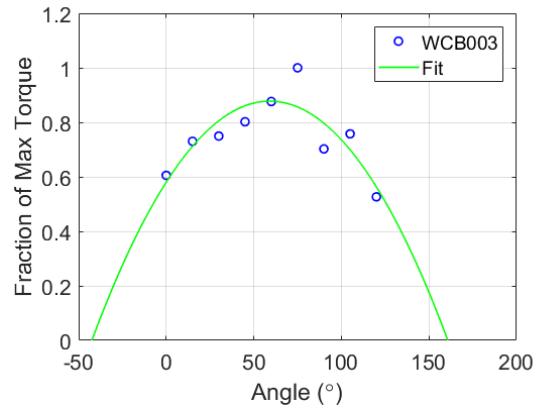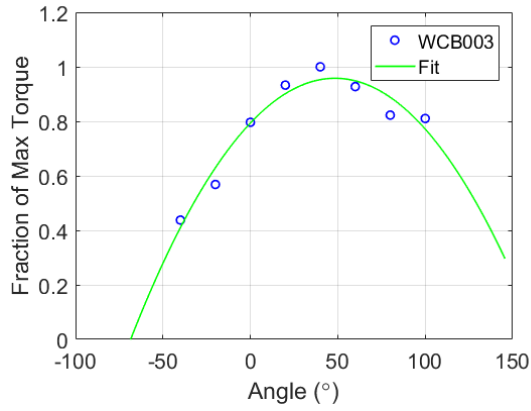
(b) Elbow Flexors

(c) Shoulder Extensors
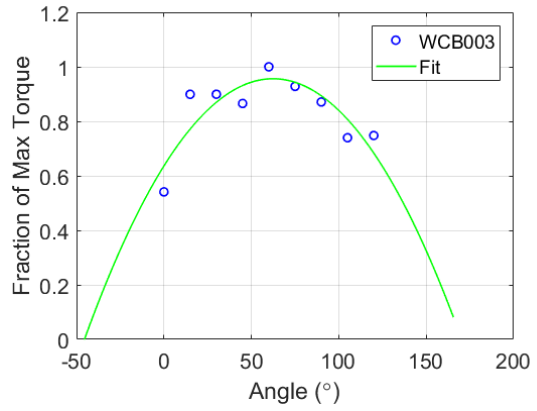
(d) Elbow Extensors
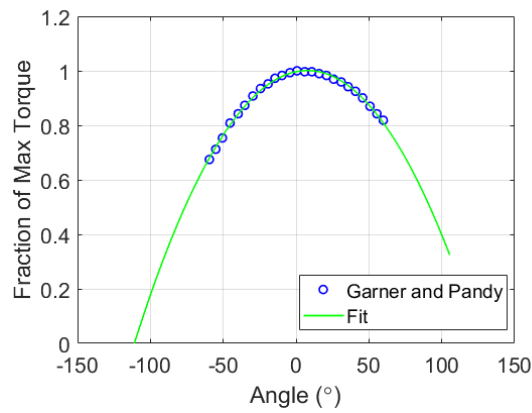
(e) Wrist Flexors/Extensors

Figure 4.11: Polynomials fit to the maximal data isokinetic dataset

4.1.2 Passive Torque

Restoring forces are produced near the anatomical joint limit by muscle tissue, tendons, and ligaments that surround the joint. Yamaguchi [81] developed an exponential equation to describe this passive torque as a function of angle and angular velocity, and is given by

$$\tau_P(\theta, \omega) = k_1 e^{-k_2(\theta - \theta_1)} - k_3 e^{k_4(\theta_2 - \theta)} - c\omega \tag{4.6}$$

where θ is the joint angle, and constant parameters are determined through fitting this equation with experimental data. The breakpoints θ_1 and θ_2 represent the physical joint angle range of motion limit in which the passive torque rises exponentially, and k_{1-4} are scalar values. A value of 0.1 Nm/s was used for the damping constant c, which was the recommended value by Yamaguchi. Parameters were obtained by [58] for the shoulder and by [78] for the wrist. To determine parameters for the elbow, output data points from experimental and model passive elbow torque data by Lemay *et al* [6] were fit to Equation 4.6. The results of this curve fitting are found in Figure 4.12. Parameter values for each joint are presented in Table 4.1. A passive torque function was not included for the torso.
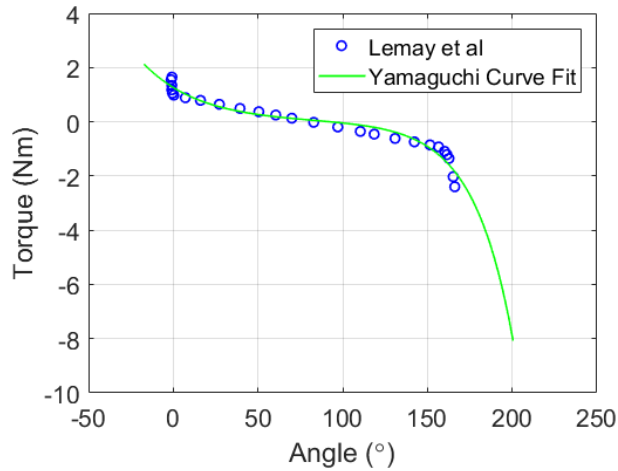
Figure 4.12: Passive torque function, $\tau_P(\theta, \omega)$, curve fitting for the elbow joint using data points from [6]

Joint	$\theta_1(\text{rad})$	$\theta_2(\text{rad})$	k_1	k_2	k_3	k_4
Shoulder	-1.14	1.27	7.03	2.31	4.30	1.65
Elbow	-0.198	2.79	1.78	1.73	1.42	2.46
Wrist	-1.17	1.19	4.30	2.73	3.90	2.89

Table 4.1: Passive joint torque parameters

4.2 Ergometer Resistive Torque

The experimental data collection was performed using a wheelchair ergometer (Keku Inc.). The ergometer consisted of a high inertia roller directly coupled with a servo motor. A calibration process also allowed for the controller to compensate for the internal resistance of the adjustable chair. The purpose of the ergometer was to apply a realistic resistance to the athlete as what would be experienced on a basketball court. The controller in the ergometer provided an equivalent rolling resistance, aerodynamic drag, as well as the inertial resistance of the athlete and wheelchair, which was based on the work by Fuss et al [64]. This was expressed by

$$\tau_{mot} = \tau_D + \tau_R + \tau_I \tag{4.7}$$

where τ_{mot} was the output motor torque, T_D was the aerodynamic drag, τ_R was the rolling resistance, and τ_I was the athlete and wheelchair inertia. Equation 4.7 can be written to include each term of the different resistive sources by

$$\tau_{mot} = \vec{r}_w \left(C_D \vec{v}_{wc}^2 + F_R + mgk_f \vec{v}_{wc}^2 \right) + m\vec{r}_w^2 \vec{\alpha}_{wc} \tag{4.8}$$

where $\vec{r}_w$ was the wheel radius, C_D was the lumped coefficient of drag, $\vec{v}_{wc}$ was the chair velocity (wheel radius multiplied by wheel angular velocity), m was the combined mass of the wheelchair and athlete, g was the gravitational constant, and k_f was the coefficient of speed influence on rolling resistance. F_R was used to describe the constant rolling resistance term. To prevent an initial backwards rotation of the wheel in the simulation, a continuous method developed by [65] was applied to eliminate the significance of this term for wheel velocities close to zero. The representation of F_R is found in Equation 4.9

$$F_R = mg\mu_R \left(\tanh \left(\frac{4\omega_{wc}}{\omega_t} \right) \right) \tag{4.9}$$

where mu_R was the coefficient of rolling friction, ω_{wc} was the wheel angular velocity, and ω_t was the approximate average angular wheel velocity. Finally, the inertial torque provided

by the athlete and wheelchair user was accounted for by manipulating the inertia term for the rigid body representing the wheel in the 2D projected model. The ergometer assumed the inertial force acting on the athlete and chair was equal to the total mass of the athlete and chair multiplied by the acceleration of the wheelchair. The servo motor then applied a torque to produce an equivalent linear resistive force to the wheels of the chair. The wheel rigid body inertia was provided a value that produced an equal linear force at the wheel:

$$\tau_I = m\vec{\alpha}_{wc}\vec{r}_w^2 = I_{m_z}\vec{\alpha}_{wc} \tag{4.10}$$

$$I_{m_z} = m\vec{r}_w^2 \tag{4.11}$$

where $\vec{\alpha}_{wc}$ was the angular acceleration of the wheelchair wheel and I_{m_z} was the equivalent rotational inertia of the athlete and wheelchair represented at the wheel axle in the body-fixed z direction (see Figure 3.1). Table 4.2 presents the parameters used to produce τ_{mot}, which used values presented by [64]. Although the combined athlete and chair weight was 80.2 kg, only half the value of this mass and I_{m_z} was used as only the right side of the athlete was modeled. A representative resultant wheel resistive torque during a propulsion simulation can be found in Figure C.1 of Appendix C.

C_D	r_w(m)	k_f(s^{2}m^{-2})	μ_R	ω_t(rad/s)	m(kg)
0.3	0.305	1×10^{-6}	0.01	2.49	40.1

Table 4.2: Simulated ergometer resistive torque generating parameters

Chapter 5

Optimal Control and Results

The optimal control method and key results of four different types of simulations are outlined in this chapter. The optimal control problem required the identification of states and controls, initial conditions, bounds, and implementation of an objective function to be minimized. These attributes to the optimal control problem varied with each simulation, which is further discussed in this chapter. The simulations generated included a sub-maximal zero and non-zero initial wheel velocity condition, as well as maximal simulations with varied vertical and horizontal seat positions. The effect of the different seat positions on joint torque requirement and push time are further discussed and analyzed in this chapter.

5.1 Optimal Control Method

In an optimal control problem, the aim is to determine the optimal function $\boldsymbol{U}^*(t)$ for the dynamic system

$$\dot{\boldsymbol{X}}(t) = f[\boldsymbol{X}^*(t), \boldsymbol{U}^*(t), t], \tag{5.1}$$

to follow an optimal state trajectory $\boldsymbol{X}^*(t)$ that minimizes the objective function

$$J = \int_{t_0}^{t_f} V[\boldsymbol{X}^*(t), \boldsymbol{U}^*(t), t] dt, \tag{5.2}$$

that is subject to the boundary conditions

$$\phi_{min} \leq \phi[\boldsymbol{X}(t_0), \boldsymbol{U}(t_0), t_0, \boldsymbol{X}(t_f), \boldsymbol{u}(t_f), t_f] \leq \phi_{max} \tag{5.3}$$

where ϕ represents the generalized constraints to the states, control, and time of the optimal control problem.

MapleSim was used to obtain the differential dynamic equations described by Equation 5.1 in the form of an Ordinary Differential Equation (ODE) for each state. Due to the presence of algebraic constraints in the dynamic equations of the 2D projected model, the differential algebraic equations were converted to ordinary differential equations. This was done by using a constraint stabilization method presented by Baumgarte [82], in which the position constraints, $\Phi = 0$, in which Φ represents the kinematic constraints, were replaced with a modified acceleration constraint equation written as

$$\ddot{\Phi} + 2\alpha\dot{\Phi} + \beta^2\Phi = 0 \tag{5.4}$$

where α and β were set to 1, and $\Phi(x, t) = 0$ was the position constraint equation. Equation 5.4 was then numerically integrated simultaneously with the ODEs from the dynamic equations.

Direct collocation was used to solve the optimization problem. In this method, the state and control are solved by approximation over a subinterval by a nth-degree polynomial. The continuous-time optimal control problem is then transcribed to a finite-dimensional Nonlinear Programming Problem (NLP), where the NLP can be solved using well-known software, such as IPOPT. This solution is obtained iteratively through mesh refinement methods until the objective function is minimized with satisfied constraints [83]. GPOPS-II is a general-purpose MATLAB software program for single or multiple-phase optimal control problems that utilizes the Legendre-Gauss-Radau (LGR) orthogonal collocation method. LGR orthogonal collocation is defined by the method with which collocation points are chosen, where collocation points are selected to be the roots of a Legendre polynomial [84]. GPOPS-II employs a unique adaptation of the LGR approach by allowing the polynomial degree, number of mesh intervals, and mesh width to be varied, known as an hp-adaptive method. Other methods are limited by being either an h method, in which polynomial degree is fixed while successively increasing the mesh interval size, or p method, in which the polynomial degree successively increases over a single mesh interval.

In GPOPS-II, the hp-LiuRao-Legendre variable polynomial order mesh method was employed [84], with a maximum of three mesh iterations and mesh tolerance of 1×10^{-7}. Furthermore, the IPOPT NLP software package was utilized to solve the resulting large-scale NLPs with a relative tolerance of 1×10^{-5} and maximum iterations of 200. In all simulations presented in Chapter 5, the optimization algorithm reached an optimum solution and did not exceed 190 iterations before automatically increasing the mesh size. For this application, increasing mesh iterations was not found to change the solution of states and controls.

State and Control

The states were described by the generalized coordinates of the 2D projected model, which were the joint angle and angular velocity of the torso, shoulder, elbow, and wheel. This is represented by 5.5. Furthermore, the activation torque of the model was included as states in the system equations, which included the torso, shoulder, elbow, and wrist, and represented by Equation 5.6. The total states for the system are represented by Equation 5.7. This allowed for the rate of torque to be handled as a control input to the system:

$$\boldsymbol{X_J}(t) = [\boldsymbol{\theta_t}(t), \dot{\boldsymbol{\theta}}_t(t), \boldsymbol{\theta_s}(t), \dot{\boldsymbol{\theta}}_s(t), \boldsymbol{\theta_e}(t), \dot{\boldsymbol{\theta}}_e(t), \boldsymbol{\theta_{wc}}(t), \dot{\boldsymbol{\theta}}_{wc}(t)] \tag{5.5}$$

$$\boldsymbol{X_T}(t) = [\boldsymbol{\tau_t}(t), \boldsymbol{\tau_s}(t), \boldsymbol{\tau_e}(t), \boldsymbol{\tau_w}(t)] \tag{5.6}$$

$$\boldsymbol{X}(t) = [\boldsymbol{X_J}(t), \boldsymbol{X_T}(t)] \tag{5.7}$$

where $\boldsymbol{X_J}(t)$ represent the joint angles of the system and $\boldsymbol{X_T}(t)$ represents the input activation torque represented as states of the system.

The coordinate associated with the wrist joint angle was obtained from the algebraic constraint of the closed chain model. The inputs to the system provided by the motor control system of the athlete are represented by Equation 5.8:

$$\boldsymbol{U}(t) = [\dot{\boldsymbol{\tau}}_t(t), \dot{\boldsymbol{\tau}}_s(t), \dot{\boldsymbol{\tau}}_e(t), \dot{\boldsymbol{\tau}}_w(t)] \tag{5.8}$$

Bounds

The initial conditions and bounds for the states and controls of the optimization are displayed in Table 5.1.

The initial hand and upper body position were selected to match the experimental hand position, which required a wheel angle and torso angle of $-1.78°$ and $36.1°$, respectively. Due to the 2D projected model assumptions, initial joint angles for the remaining upper body degrees of freedom were selected to match as close as possible to the experiment but were found to vary. The initial shoulder, elbow, and wrist were $-26.1°$, $55.7°$, and $58.4°$, respectively. This compared to -28.1, $67.6°$, and $27.1°$ experimentally. The final wheel angle of $-76.8°$ was fixed to match the final experimental wheel angle of the push phase. The beginning and end of the push phase was identified from the experimental data as

Table 5.1: Optimization initial conditions and bounds

Joint	Initial State State (°)	Angle (°)	Angular Velocity (deg/s)	Torque (Nm)	Torque Rate (Nm/s)
		Bounds (Lower, Upper)			
Torso	36.1	0, 90	±3440	–414, 197	±3200
Shoulder	–26.1	±90	±3440	–98, 105	±3200
Elbow	55.7	0, 180	±3440	–78, 68	±1800
Wrist	58.4	—	±3440	±40	±1800
Wheel	–1.78	–77.3, 1.78	±10000	—	—

when the resultant hand force exceeded 15 N. The first and last 10% of this window was removed to discount the effect of increased hand rolling along the handrim (observed in Section 3.1, Figure 3.2).

Range of motion limits were set to approximate the range of motion of each joint, which far exceeded the expected range of motion in a wheelchair push. The torso was bounded by angles of 0° and 90°, the shoulder by −90° and 90°, and the elbow by 0° and 180°. Joint angular velocity limits were ±60 rad/s (3400 deg/s), which were similar to the values used in previous predictive biomechanical simulations [78, 58, 79].

Activation torque limits for the shoulder and elbow were equal to the maximum isometric torque measured of the subject for the flexor and extensor activations. In order to adjust the torque-velocity functions to more accurate isometric torque values, the function was first divided by the τ_0 value determined in the non-linear least squares fitting process (see Appendix A), and then multiplied by the bounded activation torque value. The bounds corresponded to 105Nm and –98 Nm in the shoulder, and 68 Nm and –78 Nm for the elbow. The isometric torque estimate for the torso was determined from a flexor and extensor test conducted by Williams [85]. In this study, 61 different university varsity and amateur athletes were tested on a human dynamometer in maximum torso flexor and extensor movements. The values used in this study were the averaged peak isometric torque for all subjects of 197 Nm and −413.6 Nm for flexor and extensor activation, respectively. Values for the maximum wrist torque have varied by large margins in literature. In previous forward dynamic golf swing simulations, the wrist torque for a single arm swing was bounded by 90 Nm, and was found to result in a swing that compared closely to experiments [58]. In contrast, Garner and Pandy [5] measured isometric wrist torque at varying anatomical positions and found the maximum flexor torque to be ap-

58

proximately 23N. With such a large contrast in wrist torques, a limit of 40Nm was assumed and was modified between simulations, which is highlighted in the remaining sections of this chapter.

RTD is the studied phenomenon in which muscles are limited by how quickly they can reach maximum force [68]. In previous studies, mass normalized RTD was found to vary proportionally with joint velocity in the range of 40-130 Nm/kg/s in an upper limb torque interaction study by [68]. In comparison to the activation torque function used by [61, 77, 78, 58] it was found that the maximum torque available to each joint within 10% was obtained in the first 0.05s of activation. These approximating assumptions provided a baseline for initial guesses of the RTD value for each joint, and were varied in predictive simulation development and selected based on similarity of activation shape to literature and ease of optimization (i.e, helped the optimizer reach an optimal solution with respect to mesh and solver tolerances). Values of ± 3200 Nm/s were used for the hip and shoulder, and ± 1800 Nm/s were used for the elbow and wrist.

Objective Function

An optimization was required that solved the redundant torque problem. This redundancy is present because there are more inputs to the system (4) than degrees of freedom (2). Therefore, a suitable objective function was implemented that aimed to mimic the muscle recruitment strategy of the motor control system. Previous studies have applied different types of penalty terms in the objective function to simulate the biomechanical control input. A recent study investigating the optimized muscle activation of a Paralympic curler minimized resultant joint moments, angular joint velocities, angular joint accelerations, and mechanical power in separate objective functions [59]. The objective functions were unable to predict close agreement with experimental kinematics; however, minimizing joint accelerations produced the closest fit. The objective function used by [53] minimized the sum of change in handrim forces and change in joint moments in a high-fidelity muscle model. From these studies, it appears that an objective function that considers human efficiency is needed to best replicate the muscle recruitment strategy. Therefore, a modified version of the objective function used by [53], in which the sum of the change in activation torques and the hand forces, $\boldsymbol{F}$, was minimized.

$$J = \int_{t_0}^{t_f} \left(\dot{\boldsymbol{U}}^T \dot{\boldsymbol{U}} + w \boldsymbol{F}^T \boldsymbol{F} \right) dt, \tag{5.9}$$

where a weighting of 10 was used for w. Through trials of the predictive simulation with an objective function including a minimization of the rate of hand force, it was found

that this term provided too much difficulty for the optimizer to reach an optimal solution. Minimizing hand forces generated more efficient solutions that had lower, more realistic hand reaction forces, particularly in the normal direction. Therefore, $\dot{\boldsymbol{F}}$ was not used.

## 5.2   Predictive Simulations Versus CSIO Experiment

Simulations were generated using the optimization criteria specified in section 5.1. The simulation results are compared to experimental results that were obtained by CSIO in phase 2. The experimental data plotted in the figures of this section were the data presented in (Figure 3.5). Although the first simulated and experimental push were analyzed, it was found that the initial wheel speed was not equal to zero in the experimental data. Therefore, two different types of simulations were run which differ by the initial wheel speed. The results obtained starting from rest are presented as dashed lines and referred to as simulation A, and the results obtained with a non-zero initial wheel speed are presented as solid lines and referred to as simulation B. This non-zero initial wheel speed was set equal to the experimental initial wheel speed. The experimental results are displayed as a solid line with a circled marker. To quantify the difference in results between simulation and experiment, the Root Mean Squared Deviation (RMSD) was calculated, which was used to compare forward dynamic simulation results to experimental data in a previous study [59]. RMSDs are the square roots of the mean squared deviations between the experimental and predicted kinematics. Using this analysis, a RMSD of zero would depict a perfect agreement between data.

The initial joint angles used to generate the results for simulation A were those discussed in section 5.1. The initial joint torques and angular velocities were set to zero. Furthermore, the maximum isometric wrist torque was bounded at ± 80 Nm.

For simulation B, the initial joint angles were the same as those used in simulation A. However, the non-zero initial wheel speed required non-zero initial joint angular velocities to satisfy a continuous solution. An initial angular velocity of zero at the torso was selected. With the wheel and torso angular velocities set, MapleSim equations and experimental initial joint velocities as guesses were used to determine the remaining initial joint angular velocities that satisfied the kinematic constraints of the model. The determination of initial conditions similar to those found experimentally resulted in a more efficient optimization sequence. In this simulation, an additional constraint was used to limit wrist torque to 20 Nm. With the initial wheel angular velocity being non-zero, it was found that a larger wrist torque bound was no longer necessary.
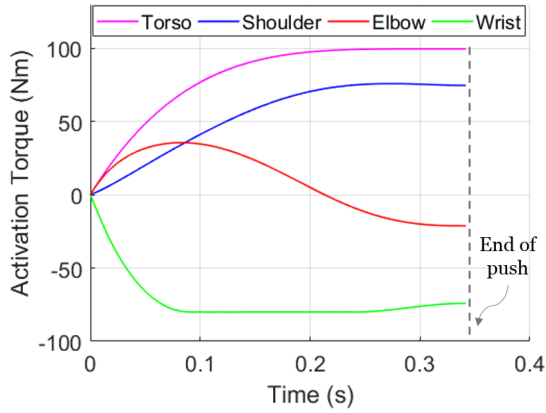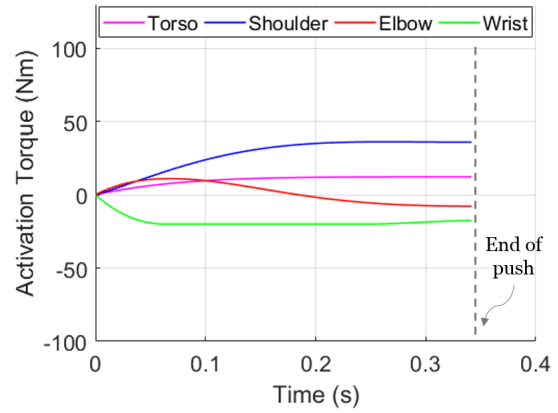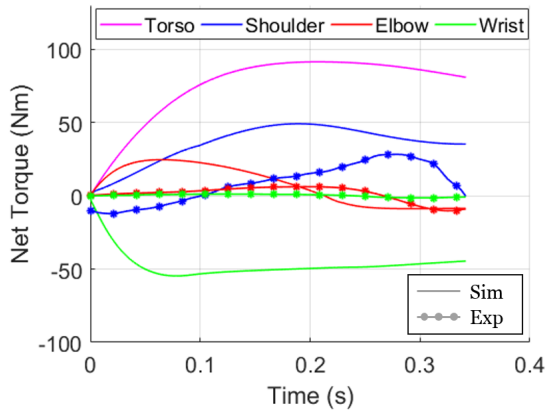
(a) Simulation A   (b) Simulation B
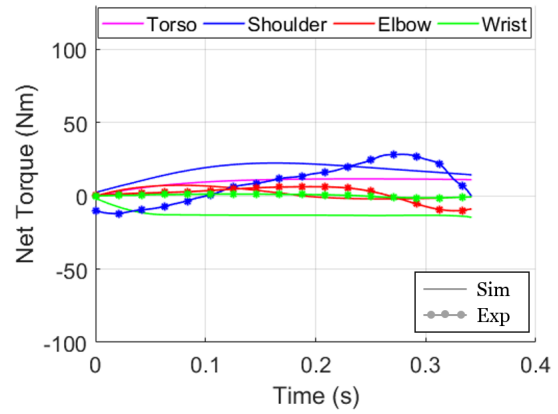
Figure 5.1: Activation torque for simulation A and B versus experiment

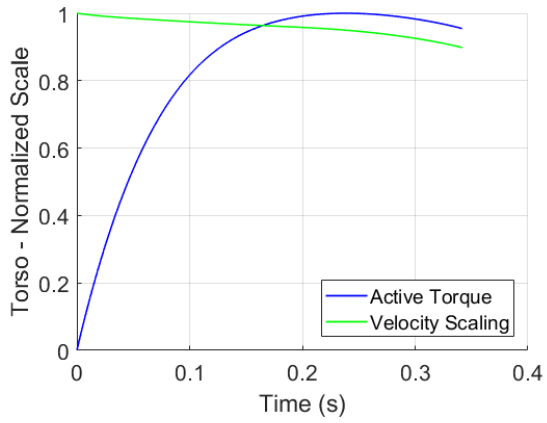(a) Simulation A   (b) Simulation B

Figure 5.2: Net torque for simulation A and B versus experiment

In Figure 5.1, the activation torque generated by the torso and shoulder resembles a steady increase in flexor activation until the end of the push phase. As a result of torque-angle-velocity scaling and passive torque, the net torque applied by the shoulder joint is lower than the activation torque in both simulations. This can be observed in Figure 5.2. For simulation A, the RMSD was 28.2Nm, 12.6Nm, and 48.0Nm for the shoulder, elbow, and wrist, respectively. In the simulation B, the RMSD was 13.6Nm, 4.99Nm, and 12.9Nm for the shoulder, elbow, and wrist, respectively. It is clear from these results that the simulated net torque was a better comparison to experiment in simulation B than A, and that the simulated elbow torque was most similar to experiment in both simulations. For the torso, the torque-velocity relationship results in a slightly lower net torque than the activation torque. The simulated shoulder torque followed a similar profile to the torque obtained from experimental data; however the simulated torque was larger throughout the entire push in simulation A. This observation was similar for both the elbow and wrist joints. Since the experimental condition had a non-zero initial wheel velocity, less work was required to reach the final wheel angle at the fixed final time than in the simulated condition. On the other hand, simulation B resulted in much lower activation and net torques than in simulation A for all joints. The net shoulder torque compares much more closely to the experimental shoulder torque than what was produced in simulation A. The largest change between simulations can be observed in the generated torso torque, as the net torque in simulation A reached 11.5 Nm, whereas the net torque in simulation B reached 91.4 Nm. The lower value in simulation B was expected, as the initial velocity of the wheelchair allowed for the final fixed wheel angle to be reached with less energy required. Further analysis of the simulated elbow torque shows that the joint provided a flexor activation followed by an extensor activation in the second half of the push. This aligns with the elbow torque profile generated from the inverse dynamic analysis. The results of the torque scaling, displayed in Figure 5.3, indicate that the elbow joint was contracting concentrically for the full duration of the push phase, as the velocity scaling curve was generally below 1. However, it can be seen at the transition between flexor and extensor activation (at 0.18 s) that there existed a short duration of eccentric contraction. Previous studies that used EMG and inverse dynamics also determined a similar effect in the elbow joint during the push phase [10, 18]. Furthermore, it was found that a relatively large wrist torque was needed to meet the constraints of the developed model and optimization procedure, and the bounds of the maximum wrist torque was doubled to 80Nm. This result was somewhat unexpected, as the wrist torque has generally been found to be the lowest of upper extremity joints [10, 28, 20, 24]. However, this demand may have been required to obtain an unrealistic average wheel velocity starting from rest, as the required wrist torque in simulation B was much lower. Finally, the largest torque observed was produced by the torso. Given the relatively large angular displacement of the torso and

full functionality in the torso of this particular experimental athlete, this was considered to be an optimal result, and falls well within the maximum torso torque generation limit. The plots in Figure 5.3 show the breakdown of how the active torque produced by the athlete was scaled. The velocity and angle scaling curves show the result of $\tau_V(\omega)$ and $\tau_A(\theta)$ at each time step, respectively, which were normalized by the maximum isometric torque for each joint. The active torque curve shows the result of $T_{act}(t)T_V(\omega)T_A(\theta)$ (see Equation 4.1) normalized by the maximum torque achieved by the joint in the simulation. Due to the similarity between simulations, only simulation B was displayed. The available torque to the model generally decreased with push progress due to the increased angular velocity of each joint and concentric contractions towards the end of the push. Interestingly, it can be seen that the simulation generally operated in an optimal region with respect to the torque-angle relationships, and as the model nears the end of the push and the joints get closer to their anatomical limits, the available torque decreased further. The maximum torque produced by each joint occurred at some point in the first half of the push. As mentioned in a previous study, it is likely that momentum generated in the upper limbs of the athlete during the first half of the push was sufficient in further increasing the velocity of the wheelchair during the last half of the push, even though the active torque decreased [50].

From Figure 5.4, the passive torque generated at each joint had a relatively small effect compared to the larger activation torque values. The initial negative shoulder angle provided a small restoring torque to resist hyperextension. Similar effects are seen from the initial flexed wrist angle. In addition, a small restoring passive torque can be observed in the elbow to resist hyperextension as the arm straightens.

The results of the terms included in the objective function are found in Figure 5.5 and 5.6. The maximum absolute RTD values for each joint occurred at the beginning of the push, and approached zero as the maximum active torque was reached. This effect has been incorporated into activation functions used in other forward dynamic models found in [47, 58]. Tangential (x) and normal (y) hand forces produced in the simulation are similar in profile to those measured experimentally, however show large differences in magnitude. The RMSD was 184N and 65.6N in the x and y direction for simulation A, whereas the RMSD was 50.4N and 18.2N in the x and y direction for simulation B. Simulation B resulted in a more accurate prediction of hand forces required to propel the wheelchair when compared to experimental data. Given that the initial conditions between simulation B and experiment were more similar, particularly the initial wheel velocity, the simulated model was required to produce a more similar amount of total work as the athlete in the experiment. This result demonstrates the importance of considering initial conditions when attempting to compare closely to a set of experimental data. The simulated hand forces

(a) Torso
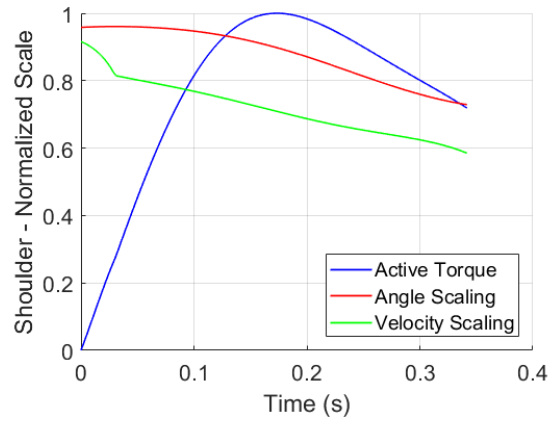
(b) Shoulder
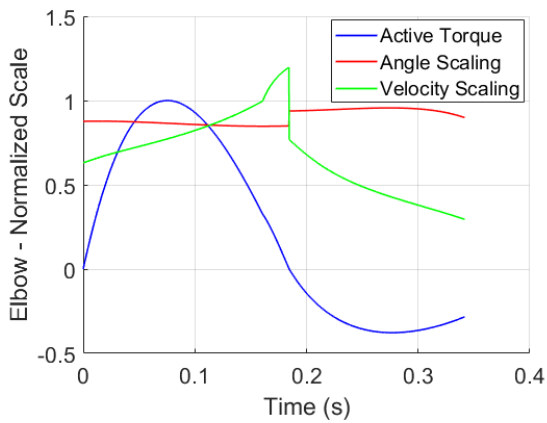
(c) Elbow
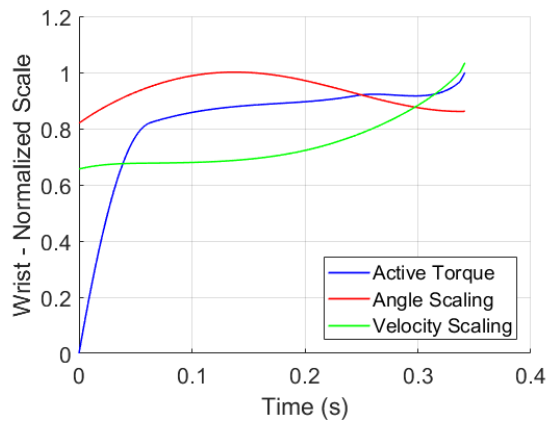
(d) Wrist

Figure 5.3: Torque-velocity-angle scaling for simulation B
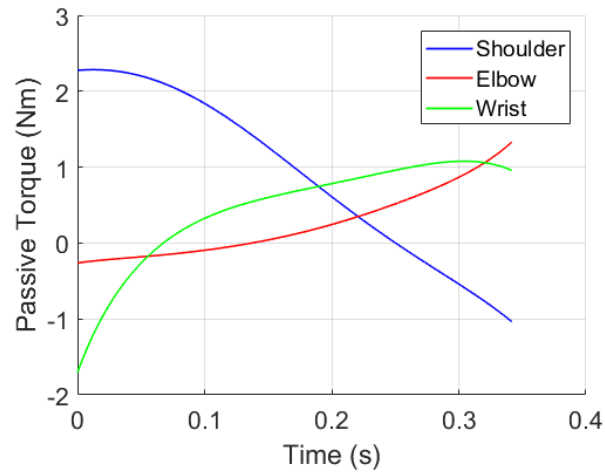
Figure 5.4: Passive torques generated in simulation B
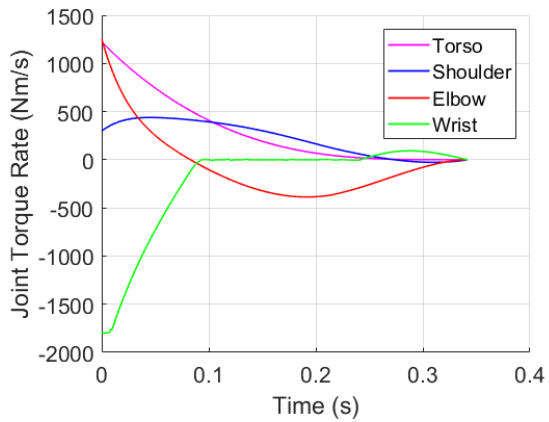
(a) Simulation A
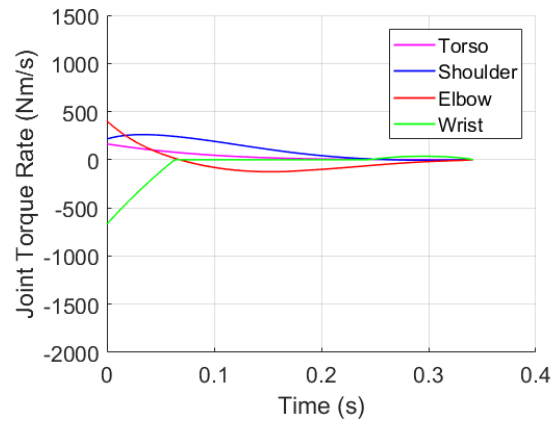
(b) Simulation B

Figure 5.5: RTD for simulation A and B

65

(a) Simulation A (b) Simulation B
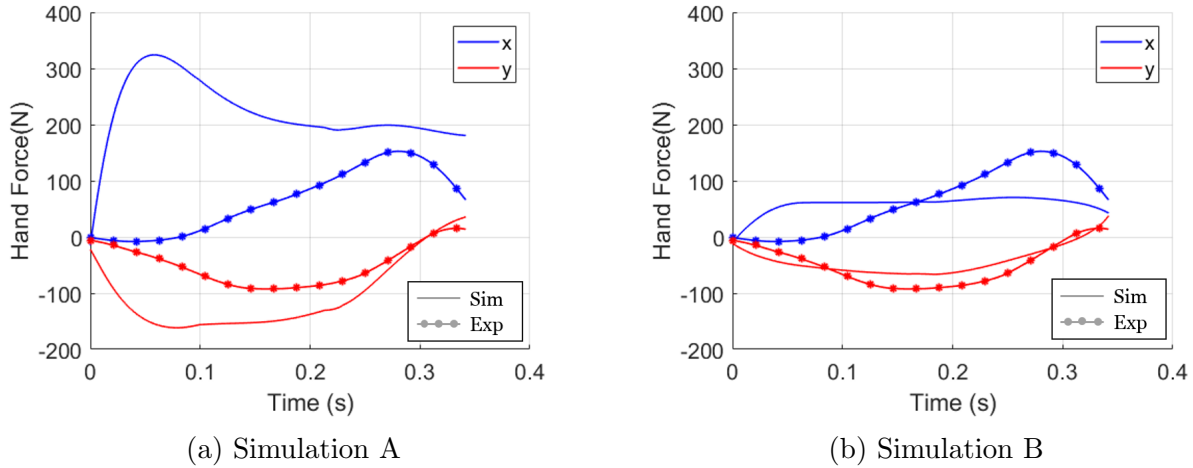
Figure 5.6: Normal (y) and tangential (x) hand force for simulation A and B versus experiment

produced larger tangential forces than normal forces, which was expected as the propulsion force is purely tangential, and resulted in a large FEF value of 88% for simulation A and 78% for simulation B. It is possible that with the lower work requirement to achieve the constrained average velocity and final wheel angle, a less efficient push could satisfy the minimization of the objective function. Maximum hand forces were observed much earlier in the push phase than were measured experimentally. The tangential force increased more quickly than the experimental condition, but plateaued to a lower maximum value. The results for simulation B (74.6 N) were more similar to the experimental measurement (81.5 N) than in simulation A (244.4 N).

The kinematic results produced in both simulations are found in Figure 5.7 and 5.8. The RMSD for the joint angles of simulation A was 7.00°, 6.96°, 9.10°, 19.7°, and 9.34° for the torso, shoulder, elbow, wrist, and wheel, respectively. For simulation B, the RMSD was 7.60°, 3.07°, 5.64°, 13.5°, and 0.458°. Other than the torso, the RMSD was lower in all joints between simulation B and the experimental data. This was largely explained by the more comparable initial conditions of simulation B to the experiment. The initial experimental wheel velocity is noticeable by the non-zero slope of the experimental wheel angle curve at the beginning of the push phase, whereas the initial slope of simulation A is zero. This resulted in a large difference between simulated virtual chair velocities, with simulation B comparing closely to the experiment. Furthermore, the torso and shoulder angles follow a similar increasing profile until the end of the push phase, at which both
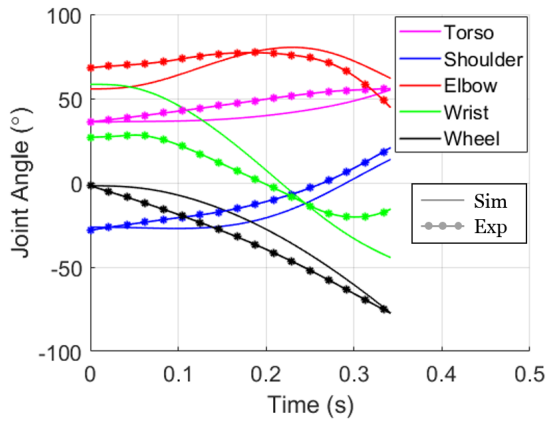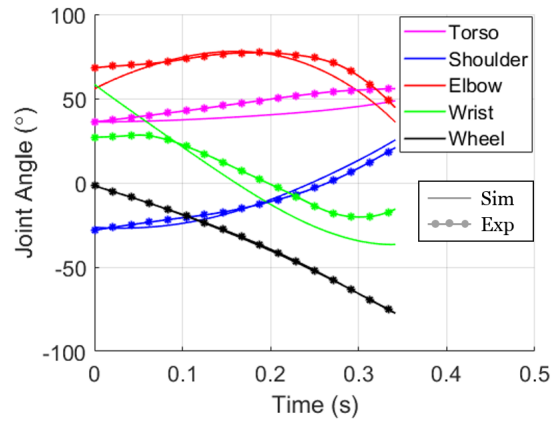
(a) Simulation A   (b) Simulation B

Figure 5.7: joint angles for simulation A and B versus experiment
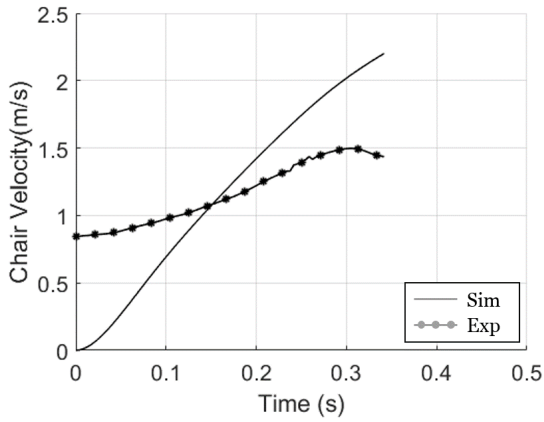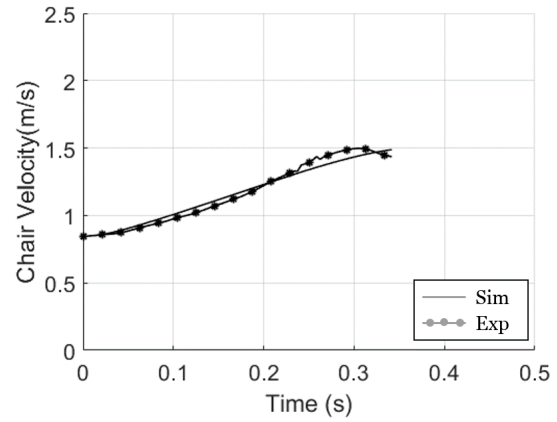
(a) Simulation A   (b) Simulation B

Figure 5.8: Virtual chair velocity for simulation A and B versus experiment

67

joints reach a very similar final state to the experiment. However, the limitations of the projected model can be observed in the elbow and wrist angles. To satisfy kinematic constraints, deviations in initial and final joint angle can be observed between simulation and experiment. Although these deviations are present, the simulated elbow joint reaches a maximum angle within close proximity to the experiment. Further complicating the ability to produce similar wrist angles to those experimentally is that the experimental grip angle to the wheel was found to be variable throughout the push phase, particularly as the athlete began the transition to the recovery phase (see Figure 3.2). However, the wrist joint angle reached an inflection point at a similar time between both simulations and experiment.

5.3 Maximum Effort and Varying Seat Position

Further simulations were generated that provided a comparison of joint torque requirement and performance between different seat positions. Due to the variation in initial conditions of the model between seat positions, it became more difficult to compare directly to the experimental condition. Simulation parameters in this section were altered to match the initial and final hand conditions of a different subject in the CSIO study. The wheel angular displacement of the first push from this subject compared more closely to those found in literature, in which the displacement of the hand occurred on both sides of top dead center. In addition, the initial torso angle was selected to be upright at 5°. This small displacement between the torso and virtual chair back was utilized to remove any neglected effect of using the chair back as leverage. Further constraints were applied to help achieve a realistic push: the final torso velocity was constrained to fall between ±1 rad/s and the final shoulder angle was constrained to achieve a minimum displacement of 25°. Furthermore, the additional constraint of the wrist at 20 Nm was removed, and the originally assumed value of 40 Nm was used. To produce a result that maximized performance, an additional term was added to the objective function that minimized the final time of the push. This effectively maximized the average velocity attained in the first push, and therefore maximized the virtual distance traveled. The weighting of this term was increased over many simulations of the same seat position until the difference in final push time was negligible. The weightings of the other objective function terms were kept the same from those used in the simulations of the previous section. The final simulation time was left open to fall between the constraints of 0.05–1 s.

5.3.1 Vertical Seat Position

Simulations were generated for seat positions of 5 cm and 10 cm lower than the neutral position. Due to issues with the optimizer, which were postulated to be related to the kinematic constraints, seat positions 5cm or further above the neutral position could not be tested. Overall, the net shoulder joint torque requirement from the optimization was lower as the seat position decreased. The largest peak shoulder torque was in the neutral position at 88.4 Nm, which was followed by 77.6Nm and 77.5 Nm for the –5 cm and –10 cm position, respectively. This pattern has been observed in previous studies that explored different seat height experimental conditions [3, 57]. Furthermore, Slowik *et al* concluded that an optimal vertical seat position that minimizes musculoskeletal demand should result in the elbow achieving a top dead center angle of 110° to 120°. The TDC values in this study were considerably lower than this, which were 47.3° (neutral), 68.8° (–5 cm) and 85.4° (–10 cm). In the most clinically important joint for wheelchair propulsion, the shoulder, the torque required decreased as the top dead center elbow angle approached the optimal range. This effect appeared to be compensated by the increased flexor torque in the torso and extensor torque in the elbow as seat height decreased. These data can be observed in Figure 5.9. For the plots of this subsection, a solid line is the neutral position, a dashed line is –5 cm, and dashed-dotted line is –10 cm.

The hand force plots are presented in Figure 5.10a, and vary in both profile and maximum value. The maximum force in the tangential direction was found to be in the neutral seat position with a peak value of 569 N. The adjusted seat height simulations produced peak forces of 464 N and 423 N for the –5cm and –10 cm condition, respectively. However, in the normal direction, a maximum downward force of 505 N was found to be largest in the -10 cm condition. The –5 cm condition had a peak downward force of 448 N, and the neutral condition was slightly lower at –447 N. These peak hand forces between simulations were all more than double those found experimentally. Furthermore, it can be seen that a large difference in profile of the force in the normal direction was present between the neutral condition and seat adjusted conditions. A significant portion of the optimal solution for both seat adjusted conditions resulted in an upward normal force over the first half of the push phase. Due to the adjusted biomechanics of these conditions, it was optimal in the control problem to pull in an upward, forward direction to minimize the push time. This effect is also observed in the neutral condition, however not to the same extreme. This effect was largely due to the starting hand position being behind top dead center, as the hand must travel in an upward direction during the first few moments of the push.

In terms of push performance, the model had a greater acceleration as chair height
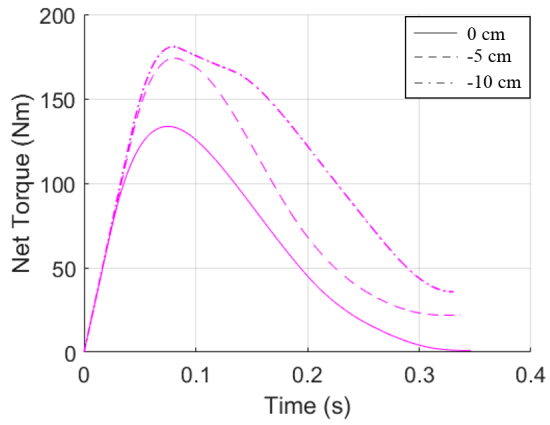
(a) Torso
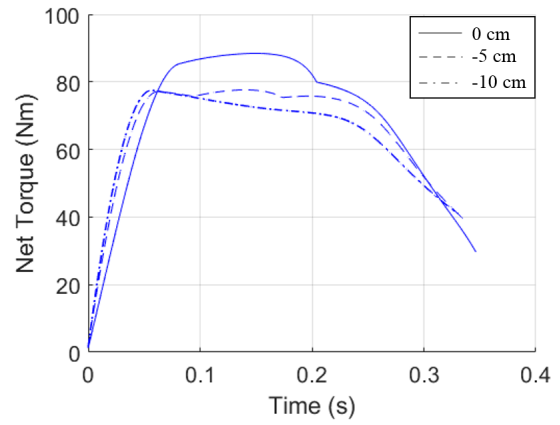
(b) Shoulder
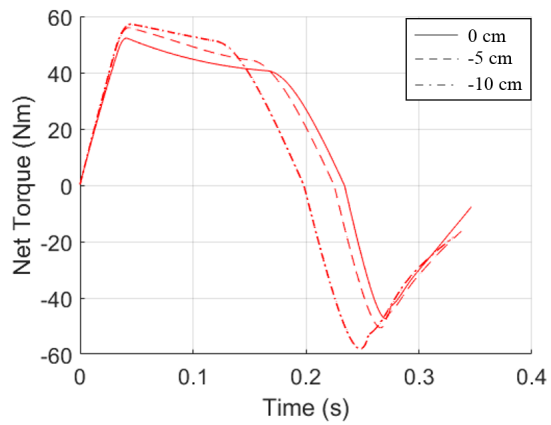
(c) Elbow
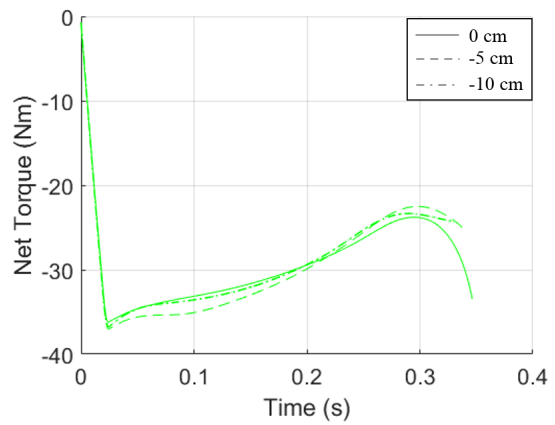
(d) Wrist

Figure 5.9: Net torque in each joint for different vertical seat heights

70
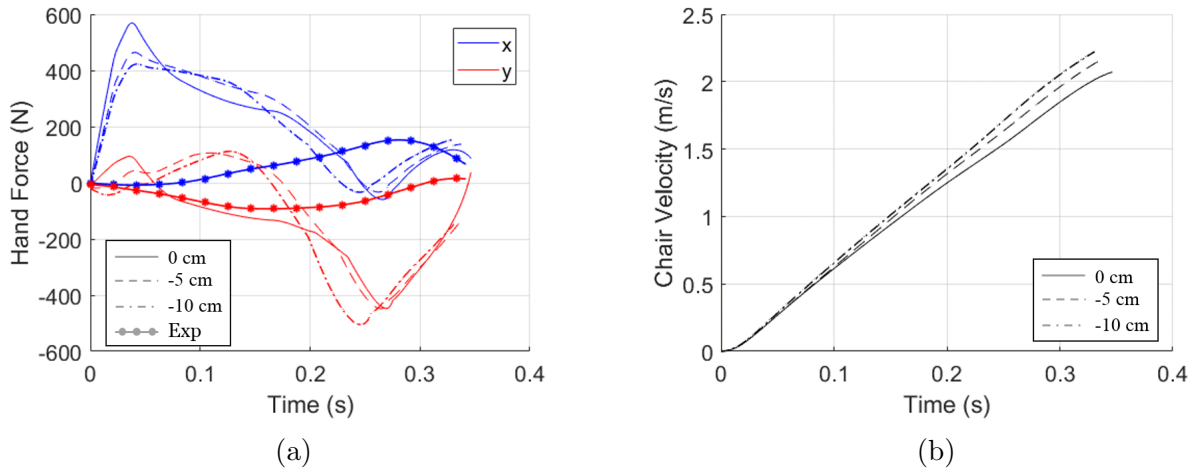
Figure 5.10: Normal (y) and tangential (x) hand force and chair velocity for different vertical seat heights

decreased. This can be observed in Figure 5.10b. It was found that the neutral optimal performance time was 0.346 s, which compares very close to the push time of 0.342 s measured by the athlete. Although the athlete pushed through a different wheel angle range, had an initial non-zero wheel velocity and was instructed to push at only 80% of maximal effort, this comparison provides a qualitative check of the realistic optimal push time determined in these simulations. The push time for –5 cm was 0.338 s, and the push time for –10 cm was 0.331 s.

5.3.2 Horizontal Seat Position

Simulations were generated at larger extreme cases for the horizontal seat direction, as the kinematic constraints of the developed model allowed for a position of –10 cm and +10 cm from the neutral condition to be simulated. The least amount of shoulder torque required to complete the push was found to be with the +10 cm seat position with a peak torque of 74.0 Nm. This was followed by peak torques of 88.4 Nm and 97.0 Nm in the neutral and –10 cm condition, respectively. The profiles of torque generation varied for each simulation as well, as it was found that the timing of peak torque transitioned to further along the push phase as seat position moved posteriorly. As with the vertical seat adjustments, a decrease in shoulder torque production was compensated by an increase in torso torque generation. However, this wasn't the case for the elbow torque. It was found that the

neutral condition required more shoulder and elbow torque than what was produced in the anterior seat position. These plots can be found in Figure 5.11
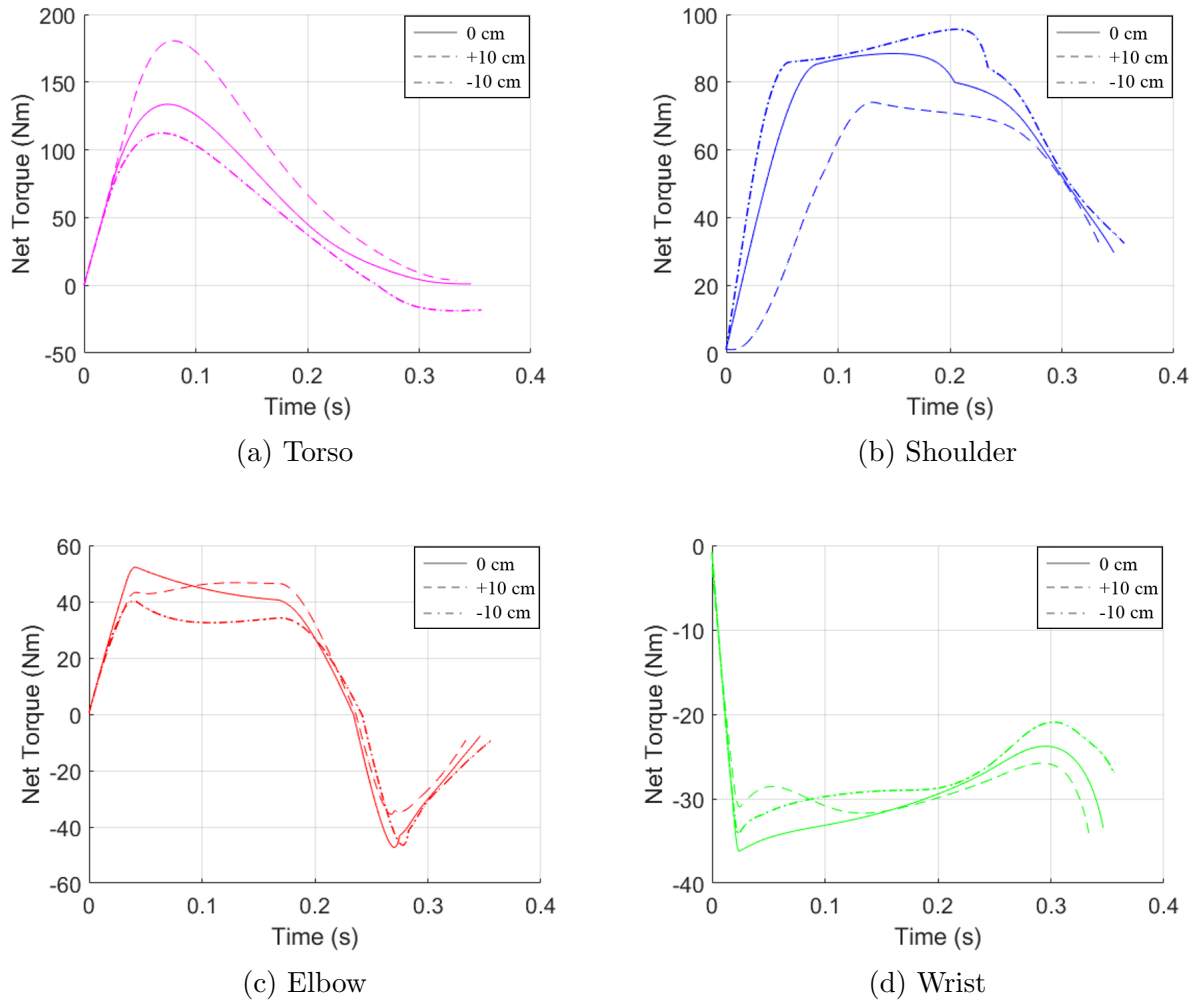
Figure 5.11: Net torque in each joint for different horizontal seat heights

In the horizontal seat adjustment simulations, the hand force plots also show variation in profile and maximum force, which can be viewed in Figure 5.12a. The maximum force in this case was the anterior seat position in the tangential direction, and was found to be 830 N, which was much larger than the 569 N neutral force determined as the largest generated in the vertical condition. The posterior simulation produced the second highest peak force of 588 N. In the normal direction, the peak neutral downward force of –447

N was found to be the lowest. Both the anterior and posterior positions resulted in peak normal forces lower than all seat vertical seat positions. The anterior peak downward force was –414 N, and for the posterior direction was –411 N. In addition, a large difference in normal force direction was found between the anterior and posterior seat positions in the first half of the push. The anterior direction has an upward force direction for more than half the push, whereas the posterior direction is downward for nearly the entire push duration. The biomechanics of the posterior direction force the model to push against the wheel rather than pull in an upward and forward direction, like in the anterior condition. In comparison to literature, Slowik *et al* discussed how various previous studies had concluded that a posterior position was optimal for reducing joint loading [53]. However, they came to the conclusion from forward dynamic simulations that a shoulder-wheel-hub angle range of –10° to –2.5° was optimal for reducing muscle stress, co-contraction, and metabolic cost, and that angles lower than –10° increased musculoskeletal demand and should be avoided. The initial shoulder-wheel-hub angles tested in this study corresponded to –13.6° (–10 cm), –4.92° (neutral), and +3.96° (+10 cm). It is difficult to compare directly to this study, as the model used different segment parameters with 3D movement and individual muscle forces, both push time and average hand force were prescribed, and the shoulder joint was held fixed during propulsion simulations in [53] In comparing qualitatively, it appeared that a shoulder-wheel-hub angle lower than –10° also increased demand in the shoulder; however decreased demand of the large torque producing torso joint, relative to the neutral condition that [53] would consider to be in an optimal range. Furthermore, the anterior position simulated was also outside of the optimal range, yet produced both lower peak torques in the shoulder and elbow than in the neutral simulation. However, this position required the largest torso torque.

For horizontal seat positions, the push time showed a decrease as seat position moved anteriorly. This can be observed in Figure 5.12b. The anterior position had a push time of 0.334 s, whereas the posterior position had a push time of 0.356 s. The summarized push time and peak shoulder torque results can be observed in Table 5.2. From these simulations, it seemed that an anterior or inferior seat position could be beneficial to alleviate the required torque production in the shoulder joint as well as to decrease push time. Overall, the fastest push time was produced by the –10 cm inferior offset from the default seat position, and the +10 cm anterior offset from the default seat position required the least amount of shoulder torque.
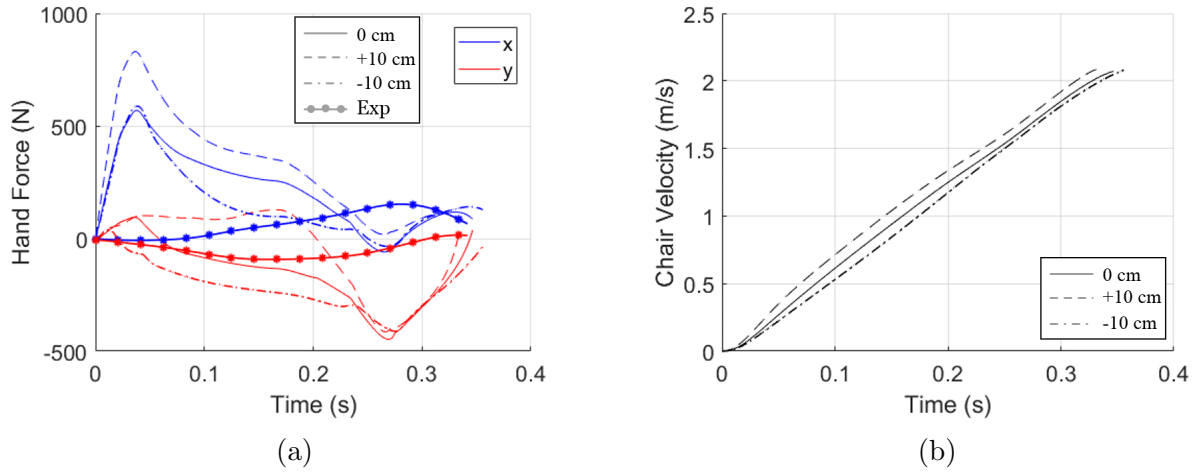
Figure 5.12: Normal (y) and tangential (x) hand force and chair velocity for different horizontal seat heights

Table 5.2: Push times for all seat positions simulated

Seat Position (cm)	Push Time (s)	Peak Shoulder Torque (Nm)
Neutral	0.346	88.4
Y: –5	0.338	77.6
Y: –10	**0.331**	77.5
X: +10	0.334	**74.0**
X: –10	0.356	97.0

Chapter 6

Conclusion

The concluding chapter of this report provides a summary of the project, and addresses some of the limitations of this study. Furthermore, recommendations are provided for the direction future work in this area of research should focus.

6.1 Project Summary

There has been a large effort over the last 30 years to develop and grow a strong research discipline of biomechanics in wheelchair propulsion. The main goal of this work was to contribute to this area of research by developing a validated, fully predictive computer simulation of wheelchair propulsion. Much of the motivation from this work stemmed from the areas of opportunity realized from the wheelchair modeling review presented in Chapter 2. These opportunities included developing a fully predictive simulation including a model of the athlete and chair, and simulating the first push with a simple model. Other opportunities were the inclusion of a torso joint and segment, the utilization of a direct-collocation optimization method, and development of subject-specific active torque functions for a wheelchair basketball athlete. This project was completed by the development of a system model and parameters as well as the forward dynamic modeling aspects, and application of the model to computer simulations.

System Model

In Chapter 3, an original 2D model was constructed that included joints for the torso, shoulder, elbow, wrist, and wheel axle. Model parameters were obtained from a 3D model

and associated parameters provided by the CSIO using an optimal parameter identification method. These identified parameters were validated by comparing an inverse dynamic calculation using the 2D projected model to the results shared by CSIO.

Forward Dynamic Modeling

Chapter 4 discussed the additional model parameters, functions, and methods that were required to run a forward dynamic simulation. Isometric and isokinetic subject-specific joint torques were measured on an elite wheelchair basketball athlete. These measurements were used to obtain parameters for input joint torque generators in the simulations of this study. Methods were employed to verify the accuracy of the Biodex joint measurements in an upper-limb application. Furthermore, the resistive torque functions and parameters were described that allowed for the simulation to predict a realistic resistance for the athlete to overcome. Finally, the direct-collocation optimization method, objective function, states and controls were presented.

Predictive Simulations

Chapter 5 presented various simulations of the first push made by a wheelchair user. First, fully predictive simulations were generated with the intent of providing close comparison to experimental kinematic and kinetic results shared by CSIO. Two different simulations were compared, which differed by the initial condition of the wheel angular velocity. Better agreement between simulated and experimental joint kinematics and kinetics were found in the simulation that used the same initial wheel velocity as was measured experimentally. Next, simulations were generated for varying vertical and horizontal seat positions to examine the change in joint torque, handrim force and push performance. A modified objective function was used to allow for a maximal effort to be simulated. Good qualitative agreement was found between the seat adjustment effects and literature; however further validation is required before firm recommendations can be made to wheelchair athletes.

6.2 Limitations

- Due to the availability of only one wheelchair basketball athlete for Biodex testing, and the fact that this was the first use of the Biodex system in this research group, it was difficult to make generalized conclusions about the quality of data collected. It

was found through preliminary tests and tests of this study that it is very difficult to obtain a high level of torque production during fast angular velocities as it requires a substantial athletic ability. This was found to be particularly true for eccentric shoulder flexor and elbow extensor tests, which becomes an issue as these testing parameters should elicit the largest torque values measured in the entire protocol. Testing more subjects under varying protocols is required to understand if this is a legitimate subject-specific biomechanical constraint and if the generalized maximum eccentric torque range of $1.3\tau_0$ to $1.5\tau_0$ should be re-investigated for upper limb torque functions.

- The simplicity of the single degree of freedom joints provided a significant benefit to the feasibility testing of the first fully predictive wheelchair propulsion simulations of its kind capable of varying initial conditions and parameters in a relatively short simulation time. However, it is important to highlight the shortcomings of such a model to providing detailed recommendations to athletes of clinical importance. The shoulder joint was modeled in its simplest form, and ignores the many degrees of freedom and complexity in movement that has been studied extensively in the modeling work of this field and others [20, 46, 47, 86]. Although generalized conclusions about joint torque remain similar between simple and complex joint models in previous literature, such as the shoulder being the largest torque generator in the arm during propulsion, the model of this study cannot predict quantities such as out-of-plane torque requirement, detailed shoulder kinematics, or individual muscle forces contributing to the net joint moment.

- The 2D planar assumption of the model was an additional benefit to reducing simulation time. However, this assumption did not provide a means of considering the effect of camber angle in the simulation. This could have contributed to some of the kinetic and kinematic differences observed between simulated and experimental results, as an increased camber angle from 0° has previously been found to result in greater energy cost and loss of energy efficiency in wheelchair propulsion [19]. Furthermore, the model could not predict the change in stability that an athlete experiences with varying seat positions, which is considered a large factor in how the athlete chooses their seat settings [53]. Furthermore, the limited degrees of freedom and kinematic constraints of the model provided some difficulty in testing a large range of vertical seat positions. Although it is unlikely that an athlete would transition to a new seat position more than a 10 cm difference from their current placement, it would be beneficial to have the flexibility in a computer simulation to test wide ranges and combinations of positions. It is possible that identifying optimal parameters for a

higher initial seat height or increasing the biomechanical degrees of freedom could help resolve this issue.

- The data shared by the CSIO was invaluable to the development of the work in this study; however natural limitations of capturing biomechanical data in the highly dynamic case of wheelchair propulsion led to some comparison difficulties to the model. Since the hip joint was hidden from view of the motion capture equipment, it was not modeled in the Visual3D environment. Therefore, experimental torso angles were estimated by considering a virtual torso segment bound between the proximal shoulder marker and fixed position on the corner of the chair back and seat. This led to some difficulties in obtaining an accurate fixed torso length that would allow close comparison between all joint planar angles, as it was variable in the sagittal plane from the marker data. It is possible that the inclusion of a markerless motion tracking algorithm or inertial measurement unit body suit could help reduce this issue of identifying the hip joint.

6.3   Recommendations and Future Work

- Using the model as is, new 2D BSIPs could be determined for an increased default seat height. This may allow for a wider range of seat adjustments that do not break kinematic constraints.

- The addition of a grip model could provide for more accurate propulsion and reduce errors in other joints that resulted in this study from the variable hand-wheel angle. This research area has been explored in previous forward dynamic simulations that could be applied to the model of this study [61, 79].

- Work towards development of a solution that minimizes the workload required by the wrist should be further studied, as inverse dynamic results typically find low torque produced by the wrist. This could be accomplished with a passive elastic wrist model [59].

- A multi-phase simulation could be pursued that incorporates the recovery phase of the wheelchair push, and allows for multiple fully predictive pushes to be simulated. This would require the integration of an open chain model to allow for free hand motion, and the determination of hand/wheel initial conditions at each new phase of push contact at the onset of the push phase.

- A predictive solution could be developed for a 3D joint torque model, such as the model developed by the CSIO in Visual 3D. Preliminary work in this area is currently in progress and was not included in this report. In this work, indications that an individually weighted rate of torque minimization objective function could provide a realistic 3D wheelchair push. This would allow for out of plane dynamics to be observed, as abduction/adduction and internal/external rotation moments have been found to be affected by changing seat conditions [53].

- A higher-fidelity muscle model should be used at each joint, such as those developed by [20, 46, 47], to optimize a fully predictive propulsion model.

References

[1] R. Cooper and M. Boninger, "Glenohumeral joint kinematics and kinetics for three coordinate system representations during wheelchair propulsion," *American Journal of Physical Medicine & Rehabilitation*, vol. 78, no. 5, pp. 435–446, 1999.

[2] W. M. Richter, "The effect of seat position on manual wheelchair propulsion biomechanics: A quasi-static model-based approach," *Medical Engineering and Physics*, vol. 23, no. 10, pp. 707–712, 2001.

[3] M. Leary, J. Gruijters, M. Mazur, A. Subic, M. Burton, and F. K. Fuss, "A fundamental model of quasi-static wheelchair biomechanics," *Medical Engineering and Physics*, vol. 34, no. 9, pp. 1278–1286, 2012.

[4] B. Guo, S. Duan, and A. Ghalambor, "Effect of handrim diameter on manual wheelchair propulsion: Mechanical energy and power flow analysis," *SPE Production and Operations*, vol. 21, no. 1, pp. 107–113, 2006.

[5] B. A. Garner and M. G. Pandy, "Musculoskeletal model of the upper limb based on the visible human male dataset," *Computer Methods in Biomechanics and Biomedical Engineering*, vol. 4, pp. 93–126, 2001.

[6] M. A. Lemay and P. E. Crago, "A dynamic model for simulating movements of the elbow, forearm, and wrist," *Journal of Biomechanics*, vol. 29, no. 10, pp. 1319–1330, 1996.

[7] E. M. Smith, E. M. Giesbrecht, W. B. Mortenson, and W. C. Miller, "Prevalence of wheelchair and scooter use among community-swelling Canadians," *Physical Therapy*, vol. 96, no. 8, pp. 1135–1142, 2016.

[8] Y. Vanlandewijck, D. Theisen, and D. Daly, "Wheelchair propulsion biomechanics: implications for wheelchair sports," *Sports Medicine*, vol. 31, no. 5, pp. 339–67, 2001.

[9] B. S. Mason, L. Porcellato, L. H. Van Der Woude, and V. L. Goosey-Tolfrey, "A qualitative examination of wheelchair configuration for optimal mobility performance in wheelchair sports: A pilot study," *Journal of Rehabilitation Medicine*, vol. 42, no. 2, pp. 141–149, 2010.

[10] S. Cerquiglini, F. Figura, M. Marchetti, and B. Ricci, "Biomechanics of wheelchair propulsion," *Proceedings of the Seventh International Congress of Biomechanics*, vol. 3A, pp. 410–419, 1981.

[11] R. Drillis and R. Contini, "Body segment parameters," tech. rep., Office of Vocational Rehabilitation, Department of Health Education and Welfare, New York, 1966.

[12] L. Y. Guo, F. C. Su, and K. N. An, "Optimum propulsion technique in different wheelchair handrim diameter," *Journal of Medical and Biological Engineering*, vol. 22, no. 1, pp. 1–10, 2002.

[13] L. Y. Guo, F. C. Su, H. W. Wu, and K. N. An, "Mechanical energy and power flow of the upper extremity in manual wheelchair propulsion," *Clinical Biomechanics*, vol. 18, no. 2, pp. 106–114, 2003.

[14] D. A. Morrow, L. Y. Guo, K. D. Zhao, F. C. Su, and K. N. An, "A 2-D model of wheelchair propulsion," *Disability and Rehabilitation*, vol. 25, no. 4-5, pp. 192–196, 2003.

[15] J. M. Munaretto, J. L. McNitt-Gray, H. Flashner, and P. S. Requejo, "Simulated effect of reaction force redirection on the upper extremity mechanical demand imposed during manual wheelchair propulsion," *Clinical Biomechanics*, vol. 27, no. 3, pp. 255–262, 2012.

[16] L. A. Rozendaal and D. Veeger, "Force direction in manual wheel chair propulsion: Balance between effect and cost," *Clinical Biomechanics*, vol. 15, no. 1, pp. 39–41, 2000.

[17] R. N. Robertson, M. L. Boninger, R. A. Cooper, and S. D. Shimada, "Pushrim forces and joint kinetics during wheelchair propulsion," *Archives of Physical Medicine and Rehabilitation*, vol. 77, no. 9, pp. 856–864, 1996.

[18] R. Price, Z. R. Ashwell, M. W. Chang, M. L. Boninger, A. M. Koontz, and S. A. Sisto, "Upper-limb joint power and its distribution in spinal cord injured wheelchair users: steady-state self-selected speed versus maximal acceleration trials," *Archives of Physical Medicine and Rehabilitation*, vol. 88, no. 4, pp. 456–463, 2007.

[19] Y. C. Huang, L. Y. Guo, C. Y. Tsai, and F. C. Su, "Mechanical energy and power flow analysis of wheelchair use with different camber settings," *Computer Methods in Biomechanics and Biomedical Engineering*, vol. 16, no. 4, pp. 403–412, 2013.

[20] H. E. J. Veeger, L. H. V. Van Der Woude, and R. H. Rozendal, "load on the upper extremity in manual wheelchair propulsion," *Journal of EIectromyography and Kinesiology*, vol. I, no. 4, pp. 270–280, 1991.

[21] M. M. Rodgers, G. W. Gayle, S. F. Figoni, M. Kobayashi, J. Lieh, and R. M. Glaser, "Biomechanics of wheelchair propulsion during fatigue," *Archives of physical medicine and rehabilitation*, vol. 75, no. 1, pp. 85–93, 1994.

[22] C. E. Clauser, J. T. McConville, and J. Young, "Weight, volume, and center of mass of segments of the human body," tech. rep., Aerospace Medical Research Laboratory, 1969.

[23] E. Hanavan, "A mathematical model of the human body," tech. rep., Aerospace Medical Research Laboratories, Wright-Patterson Air Force Base, Ohio, 1964.

[24] M. M. Rodgers and S. Tummarakota, "Three-dimensional dynamic analysis of wheelchair propulsion," *Journal of Applied Biomechanics*, vol. 14, no. 1, pp. 80–92, 1998.

[25] M. M. Rodgers, R. E. Keyser, E. R. Gardner, P. J. Russell, and P. H. Gorman, "Influence of trunk flexion on biomechanics of wheelchair propulsion," *Journal of rehabilitation research and development*, vol. 37, no. 3, pp. 283–295, 2000.

[26] M. M. Rodgers, K. J. McQuade, E. K. Rasch, R. E. Keyser, and M. A. Finley, "Upper-limb fatigue-related joint power shifts in experienced wheelchair users and nonwheelchair users," *The Journal of Rehabilitation Research and Development*, vol. 40, no. 1, p. 27, 2003.

[27] M. A. Finley, E. K. Rasch, R. E. Keyser, and M. M. Rodgers, "The biomechanics of wheelchair propulsion in individuals with and without upper-limb impairment.," *Journal of rehabilitation research and development*, vol. 41, no. 3B, pp. 385–395, 2004.

[28] K. Kulig, S. S. Rao, S. J. Mulroy, C. J. Newsam, J. K. Gronley, E. L. Bontrager, and J. Perry, "Shoulder joint kinetics during the push phase of wheelchair propulsion," *Clinical Orthopaedics and Related Research*, no. 234, pp. 132–143, 1998.

[29] A. M. Koontz, R. a. Cooper, M. L. Boninger, A. L. Souza, and B. T. Fay, "Shoulder kinematics and kinetics during two speeds of wheelchair propulsion.," *Journal of rehabilitation research and development*, vol. 39, no. 6, pp. 635–649, 2002.

[30] J. L. Mercer, M. Boninger, A. Koontz, D. Ren, T. Dyson-Hudson, and R. Cooper, "Shoulder joint kinetics and pathology in manual wheelchair users," *Clinical Biomechanics*, vol. 21, no. 8, pp. 781–789, 2006.

[31] J. L. Collinger, M. L. Boninger, A. M. Koontz, R. Price, S. A. Sisto, M. L. Tolerico, and R. A. Cooper, "Shoulder biomechanics during the push phase of wheelchair propulsion: a multisite study of persons with paraplegia," *Archives of Physical Medicine and Rehabilitation*, vol. 89, no. 4, pp. 667–676, 2008.

[32] Y. Moon, C. Jayaraman, I. M. K. Hsu, I. M. Rice, E. T. Hsiao-Wecksler, and J. J. Sosnoff, "Variability of peak shoulder force during wheelchair propulsion in manual wheelchair users with and without shoulder pain," *Clinical Biomechanics*, vol. 28, no. 9-10, pp. 967–972, 2013.

[33] Á. Gil-Agudo, A. Del Ama-Espinosa, E. Pérez-Rizo, S. Pérez-Nombela, and B. Crespo-Ruiz, "Shoulder joint kinetics during wheelchair propulsion on a treadmill at two different speeds in spinal cord injury patients," *Spinal Cord*, vol. 48, no. 4, pp. 290–296, 2010.

[34] Á. Gil-Agudo, A. Del Ama-Espinosa, E. Pérez-Rizo, S. Pérez-Nombela, and L. Pablo Rodríguez-Rodríguez, "Upper limb joint kinetics during manual wheelchair propulsion in patients with different levels of spinal cord injury," *Journal of Biomechanics*, vol. 43, no. 13, pp. 2508–2515, 2010.

[35] Á. Gil-Agudo, M. Solís-Mozos, B. Crespo-Ruiz, A. J. del Ama Eng, E. Pérez-Rizo, A. Segura-Fragoso, and F. Jiménez-Diaz, "Echographic and kinetic changes in the shoulder joint after manual wheelchair propulsion under two different workload settings," *Frontiers in Bioengineering and Biotechnology*, vol. 2, no. December, pp. 1–11, 2014.

[36] Á. Gil-Agudo, M. S. Mozos, B. C. Ruiz, A. J. Del-Ama, E. Pérez-Rizo, A. Segura-Fragoso, and F. Jiménez-Díaz, "Shoulder kinetics and ultrasonography changes after performing a high-intensity task in spinal cord injury subjects and healthy controls," *Spinal Cord*, vol. 54, no. 4, pp. 277–282, 2016.

[37] G. Desroches, R. Aissaoui, and D. Bourbonnais, "Effect of system tilt and seat-to-backrest angles on load sustained by shoulder during wheelchair propulsion," *Journal of Rehabilitation Research & Development*, vol. 43, no. 7, pp. 871–882, 2006.

[38] G. Desroches, R. Aissaoui, and D. Bourbonnais, "The effect of resultant force at the pushrim on shoulder kinetics during manual wheelchair propulsion: A simulation study," *IEEE Transactions on Biomedical Engineering*, vol. 55, no. 4, pp. 1423–1431, 2008.

[39] G. Desroches, R. Aissaoui, and D. Bourbonnais, "Relationship between resultant force at the pushrim and the net shoulder joint moments during manual wheelchair propulsion in elderly persons," *Archives of Physical Medicine and Rehabilitation*, vol. 89, no. 6, pp. 1155–1161, 2008.

[40] F. C. Van Der Helm and H. E. Veeger, "Quasi-static analysis of muscle forces in the shoulder mechanism during wheelchair propulsion," *Journal of Biomechanics*, vol. 29, no. 1, pp. 39–52, 1996.

[41] H. E. J. Veeger, L. A. Rozendaal, and F. C. T. Van der Helm, "Load on the shoulder in low intensity wheelchair propulsion," *Clinical Biomechanics*, vol. 17, no. 3, pp. 211–218, 2002.

[42] S. Van Drongelen, L. H. Van Der Woude, T. W. Janssen, E. L. Angenot, E. K. Chadwick, and D. H. Veeger, "Mechanical load on the upper extremity during wheelchair activities," *Archives of Physical Medicine and Rehabilitation*, vol. 86, no. 6, pp. 1214–1220, 2005.

[43] S. Van Drongelen, L. H. Van Der Woude, T. W. Janssen, E. L. Angenot, E. K. Chadwick, and D. H. Veeger, "Glenohumeral contact forces and muscle forces evaluated in wheelchair-related activities of daily living in able-bodied subjects versus subjects with paraplegia and tetraplegia," *Archives of Physical Medicine and Rehabilitation*, vol. 86, no. 7, pp. 1434–1440, 2005.

[44] D. J. J. Bregman, S. van Drongelen, and H. E. J. Veeger, "Is effective force application in handrim wheelchair propulsion also efficient?," *Clinical Biomechanics*, vol. 24, no. 1, pp. 13–19, 2009.

[45] R. J. Vegter, J. Hartog, S. De Groot, C. J. Lamoth, M. J. Bekker, J. W. Van Der Scheer, L. H. Van Der Woude, and D. H. Veeger, "Early motor learning changes in upper-limb dynamics and shoulder complex loading during handrim wheelchair

propulsion," *Journal of NeuroEngineering and Rehabilitation*, vol. 12, no. 1, pp. 1–14, 2015.

[46] S. R. Dubowsky, J. Rasmussen, S. A. Sisto, and N. A. Langrana, "Validation of a musculoskeletal model of wheelchair propulsion and its application to minimizing shoulder joint forces," *Journal of Biomechanics*, vol. 41, no. 14, pp. 2981–2988, 2008.

[47] M. M. B. Morrow, K. R. Kaufman, and K. N. An, "Shoulder model validation and joint contact forces during wheelchair activities," *Journal of Biomechanics*, vol. 43, no. 13, pp. 2487–2492, 2010.

[48] K. Holzbaur, W. Murray, and S. Delp, "A model of the upper extremity for simulation musculoskeletal surgery and analyzing neuromuscular control," *Annals of Biomedical Engineering*, vol. 33, pp. 829–840, 2005.

[49] A. V. Hill, "The heat of shortening and the dynamic constants of muscle," *Proceedings of the Royal Society B: Biological Sciences*, vol. 126, no. 843, pp. 136–195, 1938.

[50] G. Masson, M. A. Bégin, M. Lopez Poncelas, S. K. Pelletier, J. L. Lessard, J. Laroche, F. Berrigan, E. Langelier, C. Smeesters, and D. Rancourt, "Contribution of limb momentum to power transfer in athletic wheelchair pushing," *Journal of Biomechanics*, vol. 49, no. 13, pp. 2577–2583, 2016.

[51] J. W. Rankin, A. M. Kwarciak, W. Mark Richter, and R. R. Neptune, "The influence of altering push force effectiveness on upper extremity demand during wheelchair propulsion," *Journal of Biomechanics*, vol. 43, no. 14, pp. 2771–2779, 2010.

[52] J. W. Rankin, W. M. Richter, and R. R. Neptune, "Individual muscle contributions to push and recovery subtasks during wheelchair propulsion," *Journal of Biomechanics*, vol. 44, no. 7, pp. 1246–1252, 2011.

[53] J. S. Slowik and R. R. Neptune, "A theoretical analysis of the influence of wheelchair seat position on upper extremity demand," *Clinical Biomechanics*, vol. 28, no. 4, pp. 378–385, 2013.

[54] M. M. Morrow, J. W. Rankin, R. R. Neptune, and K. R. Kaufman, "A comparison of static and dynamic optimization muscle force predictions during wheelchair propulsion," *Journal of Biomechanics*, vol. 47, no. 14, pp. 3459–3465, 2014.

[55] J. S. Slowik, J. L. McNitt-Gray, P. S. Requejo, S. J. Mulroy, and R. R. Neptune, "Compensatory strategies during manual wheelchair propulsion in response to weakness in individual muscle groups: A simulation study," *Clinical Biomechanics*, vol. 33, pp. 34–41, 2016.

[56] J. S. Slowik, P. S. Requejo, S. J. Mulroy, and R. R. Neptune, "The influence of wheelchair propulsion hand pattern on upper extremity muscle power and stress," *Journal of Biomechanics*, vol. 49, no. 9, pp. 1554–1561, 2016.

[57] J. M. Munaretto, J. L. McNitt-Gray, H. Flashner, and P. S. Requejo, "Reconfiguration of the upper extremity relative to the pushrim affects load distribution during wheelchair propulsion," *Medical Engineering and Physics*, vol. 35, no. 8, pp. 1141–1149, 2013.

[58] W. McNally and J. McPhee, "Dynamic optimization of the golf swing using a six degree-of-freedom biomechanical model," *MDPI Proceedings of the 12th Conference of the International Sports Engineering Association*, vol. 2, no. 6, p. 243, 2018.

[59] B. Laschowski, N. Mehrabi, and J. McPhee, "Optimization-based motor control of a Paralympic wheelchair athlete," *Sports Engineering*, vol. 2, pp. 1–9, 2018.

[60] B. Laschowski and J. McPhee, "Body segment parameters of Paralympic athletes from dual-energy X-ray absorptiometry," *Sports Engineering*, vol. 19, no. 3, pp. 1–8, 2016.

[61] B. B. Kentel, M. A. King, and S. R. Mitchell, "Evaluation of a subject-specific, torque-driven computer simulation model of one-handed tennis backhand ground strokes," *Journal of Applied Biomechanics*, vol. 27, no. 4, pp. 345–354, 2011.

[62] M. A. King, C. Wilson, and M. R. Yeadon, "Evaluation of a torque driven-model of jumping for height," *Journal of Applied Biomechanics*, vol. 22, pp. 264–274, 2006.

[63] M. R. Yeadon, M. A. King, and C. Wilson, "Modelling the maximum voluntary joint torque-angular velocity relationship in human movement," *Journal of Biomechanics*, vol. 39, no. 3, pp. 476–482, 2006.

[64] F. K. Fuss, "Influence of mass on the speed of wheelchair racing," *Sports Engineering*, vol. 12, no. 1, pp. 41–53, 2009.

[65] P. Brown and J. McPhee, "A continuous velocity-based friction model for dynamics and control with physically meaningful parameters," *Journal of Computational and Nonlinear Dynamics*, vol. 11, no. 5, p. 054502, 2016.

[66] P. De Leva, "Adjustments to Zatsiorsky-Seluyanov's segment inertia parameters," *Journal of Biomechanics*, vol. 29, no. 9, pp. 1223–1230, 1996.

[67] B. Ghannadi, *Model-based control of upper extremity human-robot rehabilitation systems.* PhD thesis, University of Waterloo, 2017.

[68] A. J. Bastian, K. M. Zackowski, and W. T. Thach, "Cerebellar ataxia: torque deficiency or torque mismatch between joints?," *Journal of neurophysiology*, vol. 83, pp. 3019–3030, 2000.

[69] W. Herzog, "The relation between the resultant moments at a joint and the moments measured by an isokinetic dynamometer," *Journal of Biomechanics*, vol. 21, no. 1, pp. 5–12, 1988.

[70] P. W. Kong, "Challenges in the determination of strength parameters for simulation models of human movements," *International Journal of Modelling, Identification and Control*, vol. 2, no. 3, pp. 180–187, 2007.

[71] S. E. Forrester, M. R. Yeadon, M. A. King, and M. T. G. Pain, "Comparing different approaches for determining joint torque parameters from isovelocity dynamometer measurements," *Journal of Biomechanics*, vol. 44, no. 5, pp. 955–961, 2011.

[72] G. Wu, F. C. Van Der Helm, H. E. Veeger, M. Makhsous, P. Van Roy, C. Anglin, J. Nagels, A. R. Karduna, K. McQuade, X. Wang, F. W. Werner, and B. Buchholz, "ISB recommendation on definitions of joint coordinate systems of various joints for the reporting of human joint motion - Part II: Shoulder, elbow, wrist and hand," *Journal of Biomechanics*, vol. 38, no. 5, pp. 981–992, 2005.

[73] J. C. Otis, R. F. Warren, S. I. Backus, T. J. Santner, and J. D. Mabrey, "Torque production in the shoulder of the normal young adult male: The interaction of function, dominance, joint angle, and angular velocity," *The American Journal of Sports Medicine*, vol. 18, no. 2, pp. 119–123, 1990.

[74] R. Reiser, *Development of geometric and muscle specific parameter values for musculoskeletal modeling of the shoulder joint.* PhD thesis, University of Texas at Austin, 1993.

[75] J. M. Winters and D. G. Kleweno, "Effect of initial upper-limb alignment on muscle contributions to isometric strength curves," *Journal of Biomechanics*, vol. 26, no. 2, pp. 143–153, 1993.

[76] E. J. Sprigings and R. J. Neal, "An insight into the importance of wrist torque in driving the golfball: a simulation study," *Journal of Applied Biomechanics*, vol. 16, no. 4, pp. 356–366, 2000.

[77] S. J. MacKenzie and E. J. Sprigings, "A three-dimensional forward dynamics model of the golf swing," *Sports Engineering*, vol. 11, no. 4, pp. 165–175, 2009.

[78] D. Balzerson, J. Banerjee, and J. McPhee, "A three-dimensional forward dynamic model of the golf swing optimized for ball carry distance," *Sports Engineering*, vol. 19, no. 4, pp. 237–250, 2016.

[79] C. Brown and J. McPhee, "Dynamics of the golf club-grip interaction," *MDPI Proceedings of the 12th Conference of the International Sports Engineering Association*, vol. 2, no. 6, p. 239, 2018.

[80] J. Soest and M. F.Bobert, "The contribution of muscle properties in the control of exprosive movements," *Biological Cybernetics*, vol. 69, pp. 195–204, 1993.

[81] G. T. Yamaguchi, *Dynamic modeling of musculoskeletal motion: A vectorized approach for biomechanical anlaysis in three dimensions*. Norwell, Massachusetts: Kluwer Academic Publishers, 2001.

[82] J. Baumgarte, "Stabilization of constraints and integrals of motion in dynamical systems," *Computer Methods in Applied Mechanics and Engineering*, vol. 1, no. 1, pp. 1–16, 1972.

[83] M. Patterson and A. Rao, "GPOPS II: A MATLAB software for solving multiple-phase optimal control problems using hp-adaptive gaussian quadrature collocation methods and sparse nonlinear programming," *ACM Transactions on Mathematical Software*, vol. 41, pp. 1–37, 2012.

[84] A. V. Rao, "A survey of numerical methods for optimal control," *Advances in the Astronautical Sciences*, vol. 135, no. 1, pp. 497–528, 2009.

[85] C. Williams, *Maximum concentric, eccentric, and isometric strength of trunk flexor and extensor muscles in athletes*. PhD thesis, University of Alberta, 1992.

[86] B. Sagl, C. R. Dickerson, and I. Stavness, "Fast forward-dynamics tracking simulation: application to upper limb and shoulder modeling," *IEEE Transactions on Biomedical Engineering*, vol. Forthcomin, 2018.

APPENDICES

Appendix A

Torque Function Parameters

Table A.1: Identified parameters for polynomial isokinetic torque functions

Parameter	Shoulder Flexor	Shoulder Extensor	Elbow Flexor	Elbow Extensor
$T_0(\mathrm{Nm})$	80.3	110	74.8	52.8
$\omega_{max}(°/s)$	2000	2000	2000	1999.99
$\omega_c(°/s)$	750	438.53	750	614.17
a_{min}	0.66	0.77	0.99	0.74
$\omega_r(°/s)$	90	90	90	54.31
$\omega_1(°/s)$	17.25	90	-90	-41.94

Torque-angle functions that were used to fit subject-specific torque parameters found in Table A.2 are displayed below:

$$\tau_A(\theta) = a\theta^2 + b\theta + c \tag{A.1}$$

The shoulder flexor torque function was represented by a 4th-order polynomial:

$$\tau_A(\theta) = a\theta^4 + b\theta^3 + c\theta^2 + d\theta + e \tag{A.2}$$

Table A.2: Identified parameters for polynomial isometric torque functions

Parameter	Shoulder Flexor	Shoulder Extensor	Elbow Flexor	Elbow Extensor	Wrist Flexor/Extensor
a	-0.109	-0.230	-0.279	-0.270	-0.233
b	0.180	0.389	0.576	0.588	0.0633
c	0.144	0.794	0.580	0.636	0.997
d	-0.287	0	0	0	0
e	-0.817	0	0	0	0

Appendix B

Equivalent 3D Model

Table B.1: 3D parameters obtained by the CSIO for WCB003

Segment	Length(m)	Center of Mass(m)	Mass (kg)	Moment of Inertia $xz(\text{kgm}^2)$	Moment of Inertia $y(\text{kgm}^2)$
Torso	0.647*	0.324	25.8	2.33	1.67
Upper Arm	0.301	0.145	2.68	0.000243	0.0000388
Forearm	0.247	0.113	1.53	0.00688	0.00106
Hand	0.0384**	0	0.578	0.000255	0.000255
Wheel	0.302	0	–	–	–

*Since the hip wasn't modeled, this value represents the average distance between the hip and shoulder markers during the push. The value provided by CSIO was 0.635m
** This value represents the average distance from the wrist to the center of pressure of the hand during the push phase. The remaining length of the hand would rest on the top of the wheel. The value provided by the CSIO was 0.0775m.
It can also be noted that kinetic properties of the wheel were not included for the BSIPs identification portion of this project, as it was not necessary in comparing 3D and 2D BSIPs. Finally, the body fixed coordinates for the moments of inertia of each segment are represented in Figure B.1

The initial conditions used for the equivalent 3D model simulation are displayed in Table B.2. The ball and socket joints (shoulder and wrist) followed a [1,2,3] body-fixed Euler rotation. The coordinate system used for this model is displayed in Figure B.1, in which the Z axis is perpendicular to the sagittal (XY) plane. Furthermore, the input equations for the prescribed wheel and torso angles are shown in Equation B.1, with the

input parameters found in Table B.3 .

Table B.2: Initial conditions for the equivalent 3D model simulation

Joint	Angle(deg)
Torso	36.1
Shoulder X	–6.42
Shoulder y'	27.2
Shoulder z"	–30.6
Elbow	71.6
Wrist X	–13.6
Wrist y'	–24.6
Wrist z"	–8.08

$$\theta(t) = A\sin(2\pi f + \phi) + y_0 \tag{B.1}$$

Table B.3: Prescribed motion parameters for the equivalent 3D model simulation

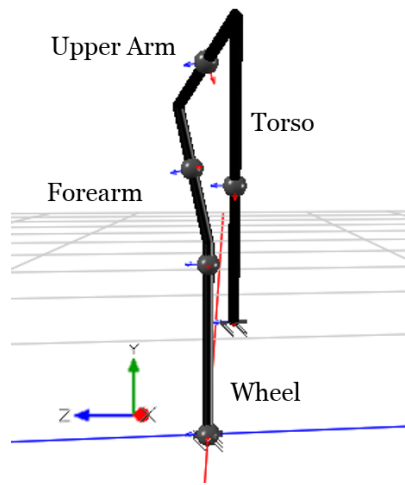| Joint	A(rad)	f(Hz)	ϕ(rad)	y_0
Torso	0.345/2	1	$-\pi/2$	$0.63 + 0.345/2$
Wheel	1.32/2	1	$-\pi/2$	$-0.0311 - 1.32/2$

Figure B.1: Coordinate system for the equivalent 3D model
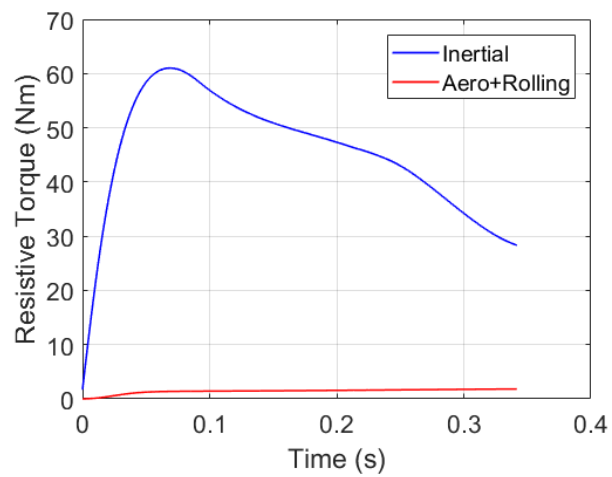
Appendix C

Resistive Wheel Torque

Figure C.1: Representative resistive wheel torque (simulation A, section 5.2)